Eur. Phys. J. A (2016) **52**: 123
DOI 10.1140/epja/i2016-16123-1

THE EUROPEAN PHYSICAL JOURNAL A

Review

Elastic scattering, fusion, and breakup of light exotic nuclei

J.J. Kolata[1,a], V. Guimarães[2], and E.F. Aguilera[3]

[1] Physics Department, University of Notre Dame, Notre Dame, IN, 46556-5670, USA
[2] Instituto de Fìsica, Universidade de São Paulo, Rua do Matão, 1371, 05508-090, São Paulo, SP, Brazil
[3] Departamento de Aceleradores, Instituto Nacional de Investigaciones Nucleares, Apartado Postal 18-1027, Código Postal 11801, México, Distrito Federal, Mexico

Received: 18 February 2016
Published online: 10 May 2016

Communicated by N. Alamanos

Abstract. The present status of fusion reactions involving light ($A < 20$) radioactive projectiles at energies around the Coulomb barrier ($E < 10$ MeV per nucleon) is reviewed, emphasizing measurements made within the last decade. Data on elastic scattering (providing total reaction cross section information) and breakup channels for the involved systems, demonstrating the relationship between these and the fusion channel, are also reviewed. Similarities and differences in the behavior of fusion and total reaction cross section data concerning halo nuclei, weakly-bound but less exotic projectiles, and strongly-bound systems are discussed. One difference in the behavior of fusion excitation functions near the Coulomb barrier seems to emerge between neutron-halo and proton-halo systems. The role of charge has been investigated by comparing the fusion excitation functions, properly scaled, for different neutron- and proton-rich systems. Possible physical explanations for the observed differences are also reviewed.

Contents

1 Introduction

This article is a review of progress made over the past decade in reactions induced by light ($A < 20$) radioactive

[a] e-mail: jkolata@nd.edu

beams at energies near to and below the Coulomb barrier ($E/A \leq 10$ MeV). Studies of elastic scattering, breakup, transfer, and fusion reactions on targets with $A > 4$ that were published between 2006 and 2015 are reported. Experimental work is emphasized, together with a selection of some of the many relevant theoretical papers on these subjects. Early publications within this time frame have already been reviewed by Keeley *et al.* [1,2]. In addition, a review of reactions with weakly bound nuclei by Canto *et al.* [3], which discusses reactions induced by both stable and radioactive projectiles and includes extensive theoretical analyses of the data, has recently appeared. All three of these publications are valuable resources for assessing the progress and future directions in this area in light of the fact that more exotic beams at higher intensity are becoming available.

2 Reactions with ^{6}He

Reactions induced by ^{6}He have continued to be a fruitful area of research in the last decade, both because of the neutron-halo nature of this nuclide and the relative ease of producing intense beams of it at energies near to and below the Coulomb barrier. Over 150 articles reporting on fusion, elastic scattering, and breakup reactions, approximately 1/3 of them experimental, have appeared during this period. The experimental papers, and some of the more important theoretical work, are reviewed below.

2.1 Elastic scattering of ^{6}He

Elastic scattering of ^{6}He and other light radioactive nuclei on various targets was last reviewed by Keeley *et al.* in 2009 [1]. Work that appeared after this publication is emphasized below.

2.1.1 ^{6}He + ^{6,7}Li

All available elastic-scattering data on these systems are reviewed in ref. [1].

2.1.2 ^{6}He + ^{9}Be

Elastic scattering of ^{6}He on ^{9}Be has been measured at an incident energy of 16.8 MeV by Majer *et al.* [4], as part of a project to study ^{7}He produced via the ^{9}Be(^{6}He, ^{8}Be)^{7}He reaction. The measured angular distribution, shown in fig. 1, is compared with data for ^{6}Li + ^{9}Be scattering at 16.6 MeV [5]. Optical-model (OM) and continuum-discretized coupled-channels (CDCC) calculations are also shown. The optical-model calculations were performed by varying the real and imaginary well depths of the ^{6}Li+^{9}Be potential of Cook and Kemper [6]. They begin to differ from the data at angles $\theta_{c.m.} > 100°$ for ^{6}Li+^{9}Be and 70° for ^{6}He + ^{9}Be. A CDCC calculation coupling to the ^{6}He continuum above the $\alpha + 2$n breakup threshold provides

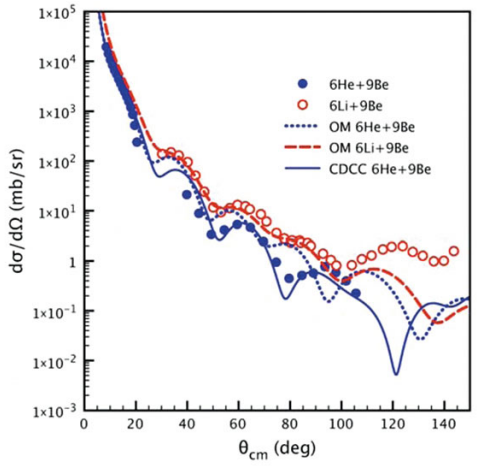

Fig. 1. Elastic scattering of ^{6}He on ^{9}Be at 16.8 MeV. Figure reprinted from ref. [4] with kind permission of The European Physical Journal (EPJ).

superior agreement with the data, illustrating the effect of the projectile breakup channel on the elastic scattering. A total reaction cross section of 1436 mb was deduced. In addition, quasifree scattering of ^{6}He on an α-particle cluster in ^{9}Be was studied, together with two-neutron stripping to states in ^{11}Be.

Additional data for elastic scattering of ^{6}He on ^{9}Be were obtained at $E_{lab} = 16.2$ and 21.3 MeV by Pires *et al.* [7]. The effect of target and projectile excitation was studied via coupled-channels calculations including coupling to the first three members of the ground-state rotational band in ^{9}Be and the 2^{+} state in ^{6}He. The rotational couplings were found to have only a minor effect, while the coupling to the 2^{+} resonance improved the agreement with experiment. Three-body and four-body CDCC calculations were also performed, and it was found that a dominant role is played by nuclear couplings to the 2^{+} resonance. Surprisingly, the trivial local potentials extracted from these calculations displayed the long-range absorption effects found for heavier targets, even though the interaction is mainly nuclear rather than Coulomb in this system. An additional analysis of this same data set was presented in ref. [8]. Average total reaction cross sections of 1525(104) mb and 1527(106) mb at 16.2 MeV and 21.3 MeV, respectively, were deduced. This implies an enhancement of $\approx 25\%$ in comparison with stable systems.

2.1.3 ^{6}He + ^{12}C and ^{6}He + ^{27}Al

All available elastic-scattering data on these systems are reviewed in ref. [1].

2.1.4 ^{6}He + ^{51}V

Angular distributions for ^{6}He quasielastic scattering on ^{51}V at laboratory energies of 15.4 and 23.0 MeV are reported in ref. [9]. The data at 23.0 MeV were compared

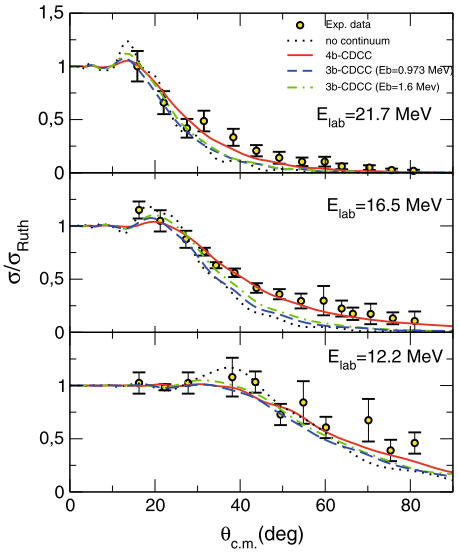

Fig. 2. Elastic scattering of ^{6}He on ^{58}Ni from ref. [10].

with ^{4}He scattering data at 23.2 MeV taken at the same time. Optical-model calculations showed that ^{6}He is far more absorbed than ^{4}He. The ^{6}He + ^{51}V total reaction cross sections were found to be 1836 mb and 2219 mb at 15.4 and 23.0 MeV, respectively.

2.1.5 ^{6}He + ^{58}Ni

Elastic-scattering angular distributions for ^{6}He on ^{58}Ni at $E_{lab} = 12.2, 16.5$, and 21.7 MeV were presented in ref. [10]. The data were analyzed via three-body and four-body CDCC calculations. The results are shown in fig. 2. It can be seen that the effect of coupling to the continuum is to remove cross section from the region of the Fresnel peak. Both the three-body and four-body CDCC calculations captured this effect. However, the three-body calculations failed to reproduce the experimental data in detail while the four-body calculations provided an excellent fit at all energies. These results were found to be quite stable with respect to changes in the optical-model potentials used in the calculations. The trivially-equivalent local potentials derived from the four-body calculation displayed a long-range imaginary part, indicating absorption from the combined effect of the nuclear and Coulomb potentials. The real part of the potential is repulsive in the surface region, which acts to reduce the fusion cross section. Finally, the total reaction cross sections were found to be 1185, 1833, and 2185 mb at $E_{lab} = 12.2, 16.5$, and 21.7 MeV, respectively. These values correspond to an $\approx 50\%$ enhancement over total reaction cross sections for ^{6,7}Li or ^{9}Be on ^{58}Ni.

2.1.6 ^{6}He + ^{64}Zn and ^{6}He + ^{65}Cu

All available elastic-scattering data on these systems are reviewed in ref. [1].

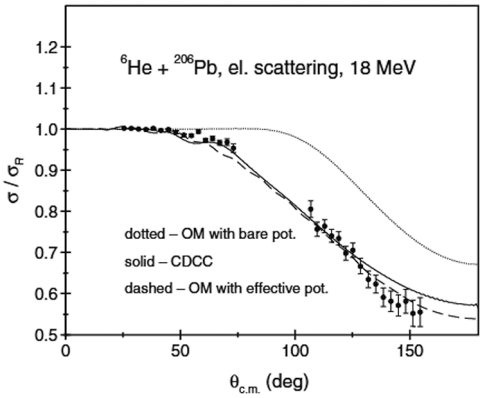

Fig. 3. Elastic scattering of ^{6}He on ^{206}Pb. Figure reprinted with permission from ref. [13]. © 2013, The American Physical Society.

2.1.7 ^{6}He + ^{120}Sn

The elastic scattering of ^{6}He on ^{120}Sn has been studied at $E_{lab} = 17.40, 18.05, 19.80$, and 20.5 MeV [11]. The angular distributions were analyzed using the optical model, and also a four-body CDCC calculation. The latter followed the methodology laid out in ref. [12] and included coupling to the breakup channel. The total reaction cross sections extracted from these analyses were compared with those from elastic scattering of stable projectiles, both strongly- and weakly-bound, on several targets. It was observed that the reduced total reaction cross sections for ^{6}He were greater than those of weakly-bound stable nuclei, which in turn were greater than those for strongly-bound projectiles. A preliminary discussion of these data was given in ref. [9].

2.1.8 ^{6}He + ^{197}Au

All available elastic-scattering data on this system at energies such that the angular distributions are not pure Rutherford are reviewed in ref. [1].

2.1.9 ^{6}He + ^{206}Pb

An elastic-scattering angular distribution for this system at $E_{lab} = 18$ MeV has been reported in ref. [13]. The data were well-reproduced by a three-body CDCC calculation [14] that included only the effect of the breakup of ^{6}He (fig. 3). This calculation very slightly over-predicted the differential cross section at c.m. angles $\geq 125°$, while a more sophisticated four-body CDCC calculation [15] tends to under-predict the data in the same angular region. The corresponding dynamic polarization potential is similar to that derived for ^{6}He + ^{208}Pb, with a long-range, attractive real part as well as long-range absorption.

2.1.10 ^{6}He + ^{208}Pb

Elastic-scattering data on this system are reviewed in ref. [1], including all information available up to 2009. Since then, two papers of interest have appeared. The first (ref. [16]) presents an analysis of the 18 MeV data from ref. [17] in terms of the dipole polarizability of ^{6}He, which was found to be much greater than those of ^{2}H, ^{3}He, or ^{7}Li. For example, the ^{6}He dipole polarizability was found to be 1.2 fm^3, the highest value yet observed, compared with only 0.70 fm^3 for ^{2}H. The second paper (ref. [18]) was a measurement of ^{6}He + ^{208}Pb elastic scattering at 22 MeV. This system had previously been studied [17] but over a more limited angular range. Agreement between the two data sets was observed. The new data were analyzed in the context of a three-body CDCC calculation, which reproduced them fairly well.

2.1.11 ^{6}He + ^{209}Bi

This system, which is the most-extensively studied of all those presented here, is reviewed in ref. [1]. No new information has become available since the publication of that article.

2.2 Breakup of ^{6}He

The first indication of the anomalous breakup cross section of ^{6}He at energies near the Coulomb barrier was published in 2000 [19]. In this paper, an astonishingly strong α-particle group from ^{6}He + ^{209}Bi, possibly resulting from breakup of ^{6}He, was noted. However, the energy spectrum of the α-particles was consistent with that expected from Q-window calculations for 2n-transfer to ^{211}Bi. Subsequently, a series of α-n coincidence experiments [20–22] established that 2n-transfer was indeed the most important process, and that 1n-transfer and direct breakup were less important, each having only about 1/2 the cross section for 2n-transfer. In this section, further work in the last decade on ^{6}He breakup near the Coulomb barrier is reviewed. Additional data on a number of systems can be found in ref. [1].

2.2.1 α-particle production in ^{6}He reactions near the Coulomb barrier

Alpha-particles from the breakup of ^{6}He on a ^{120}Sn target were observed by deFaria *et al.* [23]. The α-particle energies and angular distributions led to conclusions about the reaction mechanism that agreed with those discussed in ref. [19]. A preliminary report of this work appeared in ref. [9].

Escrig *et al.* [24] observed α-particle production in the ^{6}He + ^{208}Pb reaction at energies near the barrier and developed a method to calculate 2n-transfer to continuum states in ^{210}Pb. Their analysis indicated that the α-particles emitted at backward angles in this reaction are mainly due to two-neutron transfer to weakly-bound states of the final nucleus. More recently, Fernández-García *et al.* [25] and Acosta *et al.* [18] have used this method to analyze data for the same system at a number of nearby energies and reached the identical conclusion. In all three experiments, however, the α-particle yield was somewhat underpredicted.

In addition to elastic scattering, α-particle production in the ^{6}He+^{206}Pb reaction at 18 MeV was also reported in ref. [13]. The observed yield was analyzed in the context of the DWBA. For 1n-transfer, (d,p) spectroscopic factors for transitions to known low-lying states were used. The emission angle of the resulting α-particles was assumed to be identical with that of the outgoing ^{5}He. Since the 2n-transfer Q-window is at high excitation energy, a fictitious $6S_0$ dineutron state was placed at an excitation energy of 14 MeV in ^{208}Pb. Both calculated transfer processes peak at angles $\geq 100^\circ$ and their sum slightly overpredicts the observed cross section at backward angles. The 1n- and 2n-transfer cross sections were calculated to be of similar magnitude, though it was emphasized that these calculations are very much model dependent. The effect of transfer on the elastic channel was investigated in a Coupled Reaction Channel (CRC) calculation using the neutron-transfer parameters from the DWBA. Introduction of the transfer channels significantly reduced the predicted elastic scattering at backward angles. However, a reasonably good fit to the experimental data could be achieved by replacing the ^{6}He + ^{206}Pb optical-model potential by one having a short-range imaginary potential in order to avoid double-counting in the absorptive potential.

2.2.2 Effect of breakup on elastic scattering and fusion near the Coulomb barrier

As mentioned in sect. 2.1.5 above, the trivially-equivalent local potential (TELP) for ^{6}He + ^{58}Ni scattering at an energy of $E_{lab} = 16.5$ MeV has been evaluated by Morcelle *et al.* [10] using both 3-body and 4-body CDCC. The results, shown in fig. 4, demonstrate the effect of breakup coupling on the scattering potential. In particular, the main features are the generation of long-range absorption (due to both Coulomb and nuclear effects) and an additional repulsion in the real part of the potential in the surface region ($R \approx 6$–7 fm) which serves to enhance the Coulomb barrier. Similar features have been observed in lighter systems where the Coulomb potential is less dominant [7], and seem to be a general characteristic of polarization potentials derived from CDCC calculations for neutron-halo projectiles.

Sargsyan *et al.* [26] analyzed the effect of breakup on the fusion cross section of a number of systems, including ^{6}He incident on targets of ^{64}Zn, ^{197}Au, and ^{209}Bi. They used the quantum diffusion approach (see for example ref. [27]) in an attempt to gain an understanding of breakup systematics on fusion suppression near the barrier. Neutron transfer channels and deformation effects were taken into account within this approach. Calculated capture cross sections were compared with experimental

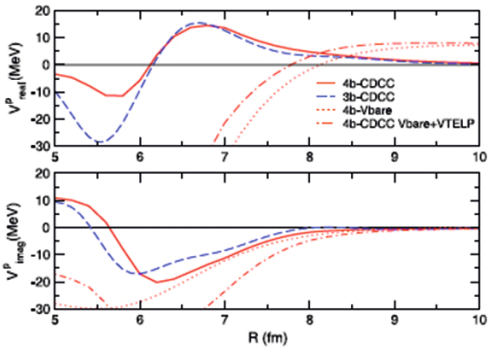

Fig. 4. Trivially-equivalent local potential for ^{6}He on ^{58}Ni from ref. [10].

fusion data. Unfortunately, no systematic trends were observed. The computed fusion excitation functions reproduced the energy dependence for ^{6}He fusion, but it was necessary to normalize the calculated cross sections by factors of 0.4, 0.8, and 0.68 for ^{64}Zn, ^{197}Au, and ^{209}Bi, respectively. A similar conclusion was reached by Gomes *et al.* [28] in a search for systematics in the fusion of ^{9}Be with a number of targets, using a very different method.

Kucuk [29] has analyzed the elastic scattering of ^{6}He on targets of ^{12}C, ^{27}Al, ^{58}Ni, ^{64}Zn, ^{65}Cu, ^{197}Au, ^{208}Pb, and ^{209}Bi at energies near the Coulomb barrier, as well as on ^{12}C at 38 and 42 MeV/A. A double-folding-model approach based on a No Core Shell-Model (NCSM) wave function for ^{6}He, together with a phenomenological imaginary potential, was used. All data were taken from the literature. The predictions for all targets were quite good. In addition, the ^{6}He + ^{208}Pb data were chosen for an investigation into the breakup threshold anomaly [30]. It was found that the real part of the scattering potential decreases at lower energies, while the imaginary potential increases just as in the case of ^{6}Li + ^{208}Pb [30]. This may be the result of strong coupling to breakup channels at near-barrier energies.

In order to more directly evaluate the effect of coupling to breakup channels on fusion cross sections near the barrier, Canto *et al.* [31,32] have derived a "Universal Fusion Function" (UFF) which they used to compare the systematic behavior of fusion cross sections for strongly-bound and weakly-bound stable projectiles, as well as halo nuclei such as ^{6}He. As a first step, the data are compared with predictions based on an optical-model potential that takes into account the target and projectile densities. Canto *et al.* adopt the São Paulo folding-model potential [33]. Next, barrier parameters are deduced following the Wong model [34] and a dimensionless fusion function F is defined:

$$F(x) = \frac{2E\sigma_F}{\hbar\omega R_B^2}\,; \qquad x = \frac{E - V_B}{\hbar\omega}\,. \tag{1}$$

Here, σ_F is either the experimental cross section or the one extracted from the optical-model potential using incoming-wave boundary conditions. In the case of systems that follow the Wong formula, $F(x)$ reduces to:

$$F_0(x) = \ln[1 + \exp(2\pi x)]. \tag{2}$$

Canto *et al.* call this the Universal Fusion Function (UFF) since it doesn't depend on the system and can therefore be used to directly compare different systems. Deviations of the reduced experimental data from the UFF are taken as a sign of channel-coupling effects. However, in order to isolate the effect of breakup couplings it's necessary to account for other effects, such as coupling to inelastic channels, by carrying out a coupled-channels calculation and renormalizing the data according to:

$$\bar{F}_{exp}(x) = F_{exp}(x)\frac{F_0(x)}{F_{CC}(x)}\,. \tag{3}$$

Here, $F_{CC}(x)$ is the fusion function from the coupled-channels calculation. Then, under the assumption that all relevant channels have been included, deviations of the renormalized experimental fusion function from the UFF, $F_0(x)$, arise only from coupling to the breakup channels. Qualitatively, the results of applying this procedure to fusion of ^{6}He with high-Z targets such as ^{209}Bi or ^{238}U gave evidence for suppression of $\approx 30\%$ above the barrier and a small enhancement below it [31,32]. In a later article [35], the same group analyzed ^{6}He + ^{64}Zn data [36] and unexpectedly found even greater fusion suppression.

Moro *et al.* [37] have calculated three-body breakup assuming either transfer to the continuum (TC) or direct breakup (bu). They analyzed data from the ^{6}He + ^{208}Pb reaction at 22 MeV [18] and the ^{8}B + ^{58}Ni reaction at 26 MeV [38]. The ^{8}B data were equally-well represented in both schemes, but the ^{6}He data were in much-better agreement with the TC calculation, indicating that the α-particles emitted at backward angles arise from 2n-transfer to slightly-unbound states of the target. In this case, the transferred neutrons are highly-correlated in the final state of the target. This calculation assumed a di-neutron model for ^{6}He. Ogata *et al.* [39] have analyzed ^{6}He + ^{209}Bi elastic scattering at 19 and 22.5 MeV [19] in a four-body CDCC calculation that removes this constraint. They found that the elastic-scattering cross section was much better represented in the four-body approach, but didn't carry out a TC analysis of the α-particle data. An earlier version of this work was reported in ref. [40].

2.3 Fusion of ^{6}He

In this section, results from fusion measurements with a ^{6}He projectile that appeared since the review of Keeley *et al.* [1] are presented. In addition, a selection of some of the many theoretical papers on this subject are discussed.

2.3.1 Recent experimental work on ^{6}He fusion

Scuderi *et al.* [41] have studied fusion, breakup, and transfer in the ^{6}He + ^{64}Zn reaction at energies near the barrier. The breakup and transfer results, obtained by looking at α-particle production, were consistent with their previous measurements [36]. The fusion cross sections were measured using an activation technique, by detecting delayed x-ray activity following the electron-capture decay

of the evaporation residues. Statistical-model calculations showed that electron-capture decay predominates for this beam-target combination and that stable decay products constitute at most 10% of the fusion yield. A stack of four ^{64}Zn targets separated by ^{93}Nb catcher foils was exposed to a ^{6}He beam at two different energies, and the x-ray activity was detected off-line using a Si(Li) detector having an efficiency of 100% for the energies of interest. Five different fusion-evaporation channels were observed and separated by their corresponding x-ray energies and half-lives. Cross sections were determined from the measured number of incident beam and target particles and the known Kα fluorescence probabilities. The beam current was measured as a function of time in order to correct for decay of short-lived activities during the bombardment and transfer to the counting station. The fusion excitation function was initially obtained by summing the contributions from all the reaction channels. However, it was observed that the αn channel leading to ^{65}Zn was very strong compared with a statistical-model calculation. Since this channel could also be reached via the known strong transfer processes, a corrected fusion probability was obtained by replacing its measured cross section by the calculated one. The data were compared with results from the ^{4}He+^{64}Zn system reported in the same experiment. It was concluded that no effect on the fusion cross section at energies above the barrier was evident in the ^{6}He-induced reaction with respect to that induced by ^{4}He. Enhancement of the fusion cross section observed below the barrier was attributed to static effects of the halo structure rather than dynamic coupling effects.

Complete (CF) and incomplete (ICF) fusion reactions of ^{6}He on ^{166}Er were investigated by Fomichev *et al.* [42] at an energy of 64 MeV, well above the Coulomb barrier. The data were compared with results from the ^{6}Li+^{165}Ho and ^{6}Li + ^{166}Er reactions at 58 MeV. Charged particles, γ rays, and neutrons were detected. Exit channel identification was obtained via a (γ_1-γ_2-light charged particle) triple coincidence. Relative intensities of γ rays in ^{166}Yb from ^{165}Ho (^{6}Li, 5n) and ^{166}Er (^{6}He, 6n) were compared as a function of the spin of the γ-emitting state, up to 22$\hbar$ in the ground-state band and one excited band. The results were compared with the predictions of the EMPIRE code (ref. [43]). From this comparison, the effects of ICF reactions associated with the capture of the α clusters in either ^{6}Li or ^{6}He by the ^{166}Er nuclei were estimated to be less than 10% as compared with the intensities of the ^{166}Yb γ rays and corrections were made for this process. The spin distribution of the compound systems were deduced from the corrected intensities and CF suppression factors of 3.4 for the ^{6}He reaction and 2.4 for the ^{6}Li reactions were calculated, again by comparison with EMPIRE, suggesting a large effect of projectile breakup. A similar analysis was made for γ rays in the ground-state band of ^{164}Er coming from ^{165}Ho (^{6}Li, α3n) and ^{166}Er (^{6}He, α4n), and values for lower and higher orbital angular momentum cutoffs were deduced.

Fusion and nucleon transfer processes in the ^{6}He + ^{197}Au system were studied in the energy range from 40–120 MeV by Skobelev *et al.* [44]. The stacked-foil activation method was used, with Au foils separated by Al absorbers to degrade the beam energy. A range of Tl, Au, and Hg isotopes were identified off-line using γ detectors. Excitation functions for fusion reactions involving the evaporation of up to ten neutrons from the compound nucleus, as well as reactions with the emission of charged particles and nucleon transfer products, were obtained. It was concluded that, unlike the situation at near-barrier energies, no evidence for fusion inhibition was found. The production cross sections for ^{194,196}Au and $^{192-197}$Hg, however, were shown to be dominated by direct processes over the entire energy range. Isomeric ratios for several isotopes of Tl, Au, and Hg were also determined. Isomeric ratios for ^{196,198}Tl and ^{196,198}Au produced via ^{6}He + ^{197}Au fusion and transfer reactions had already been measured by Kulko *et al.* [45]. Population probabilities for high- and low-spin states were determined in the range from 7–60 MeV and compared with statistical-model calculations. They were found to be similar to those from ^{4}He-induced reactions. The isomeric ratios for fusion reactions followed by the evaporation of five and seven neutrons were 1 to 3 orders of magnitude greater than those observed for neutron-transfer products. Finally, the isomeric ratios for ^{196}Au and ^{198}Au produced via transfer processes displayed a different energy dependence and differ in absolute value: in the case of neutron removal from ^{197}Au, the isomeric ratios are higher than for the transfer of a neutron to ^{197}Au.

Sub-barrier fusion of ^{6}He with ^{206}Pb was measured by Wolski *et al.* [46] in the energy range from 14–28 MeV using a stacked-foil activation technique and radiochemical analysis via α-particle detection. The elastic scattering at 18 MeV was simultaneously measured during the beam exposure period in order to obtain an accurate value for ^{210}Po production in this reaction. This 2n-evaporation channel dominates the fusion cross section at all energies except for the highest one measured. Corrections were made for the naturally-occurring background from this isotope. The deduced fusion cross sections were in disagreement with an earlier measurement [47,48], as illustrated in fig. 5. It was suggested that the disagreement

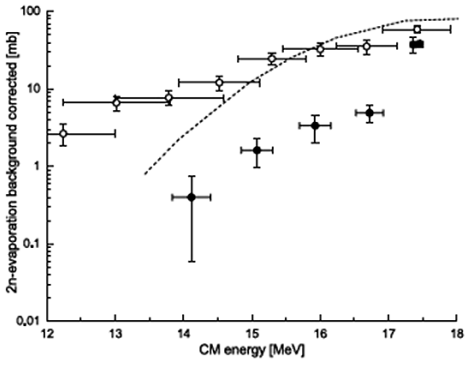

Fig. 5. Data for sub-barrier fusion of ^{6}He+^{206}Pb from refs. [46] (solid circles) and [47] (open circles). The dashed curve is the prediction of the sequential fusion model [48,49] for the 2n evaporation channel. Figure reprinted from ref. [46] with kind permission of The European Physical Journal (EPJ).

might be due to the effects of the beam energy spread, which was particularly significant for the earlier data as noted by the large horizontal error bars for this experiment shown in the figure. However, it is not clear that this effect could completely account for the very large differences below 17 MeV, and the much smaller discrepancy at 17.5 MeV is unexplained. The authors of ref. [47] also used the stacked-foil method with off-line α-particle detection and compared with ^{4}He + ^{208}Pb fusion leading to the same ^{212}Po compound system and the same ^{210}Po 2n-evaporation channel. Good agreement was obtained with data from a previous experiment [50].

3 Reactions with ^{8}He

Reaction data for ^{8}He beams at energies near the Coulomb barrier are still very scarce due to the limited availability of this beam. Two early papers, from 2003 and 2004, are reviewed in ref. [1]. More recently, Marquínez-Durán *et al.* [51,52] have studied ^{8}He elastic scattering and reactions on a ^{208}Pb target at energies of 16 and 22 MeV. (The Coulomb barrier for this system is at 19 MeV). They compared their elastic-scattering results with ^{6}He + ^{208}Pb data at the same energies and found that the absorption was greater for ^{8}He (see, *e.g.* fig. 6). The observed absorption was consistent with the fact that large yields of ^{4}He and ^{6}He fragments were also seen. The data were also compared with a coupled-reaction-channel (CRC) calculation including only 1n-stripping to ^{7}He. The data near the Fresnel peak and at back angles were somewhat overpredicted, probably due to the neglect of other reaction channels.

Transfer/breakup channels in the ^{8}He + ^{197}Au system at $E_{lab} = 18.7, 20.1$ and 29.4 MeV, and the ^{8}He+^{65}Cu system at $E_{lab} = 19.9$ and 30.6 MeV, were studied by Lemasson *et al.* [53]. Two different experimental methods were used. For the ^{65}Cu target, in-beam measurements of light charged particles, neutrons, and γ-rays were carried out. The Q-value spectrum for ^{6}He in coincidence with the 186-keV γ-ray transition in ^{66}Cu peaked around $Q = 0$, consistent with expectations for 2n-transfer to states in ^{67}Cu above the neutron-emission threshold. The inclusive Q-value distribution was nearly identical in shape, suggesting that 2n-transfer processes to low-lying bound states were weak or non-existent. Very large total neutron transfer cross sections ($\sigma_{1n} + \sigma_{2n}$) of 782 ± 78 (759 ± 114) mb at 19.9 (30.6) MeV were deduced from the measurement of characteristic γ-ray transitions, corrected for γ-rays arising from fusion-evaporations reactions.

A stacked-foil radiochemical technique was used with the ^{197}Au target. Gamma rays from ^{198,199}Au were counted off-line, and cross sections for ^{198m}Au were also obtained from γ-γ coincidence data. Surprisingly, a relatively large cross section was obtained for ^{199}Au despite the fact that the optimum Q-value for 2n-transfer would lead to population of states that are well above the neutron-emission threshold (see fig. 7). In the case of the ^{65}Cu target discussed above, survival of ^{67}Cu was not

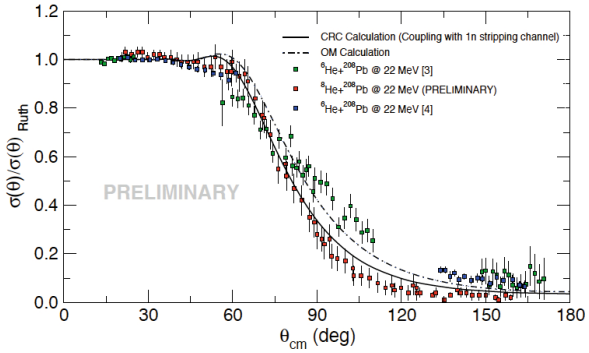

Fig. 6. Ratio-to-Rutherford of the elastic cross section for ^{8}He + ^{208}Pb and ^{6}He + ^{208}Pb at $E_{lab} = 22$ MeV. The dot-dash line is the result of an optical-model calculation using parameters from ^{6}Li + ^{208}Pb scattering, while the solid line is the result of a CRC calculation including 1n-stripping. See refs. [51,52] for details.

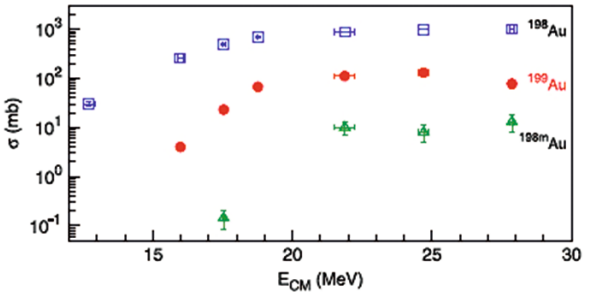

Fig. 7. Excitation functions for ^{198,198m,199}Au production from ref. [53].

observed. An explanation for this difference was given in terms of mixing of bound and unbound levels in ^{199}Au.

Fusion of ^{8}He with ^{206}Pb was studied by Parkar *et al.* [54] at energies near the Coulomb barrier, using a radiochemical technique with stacked targets of ^{206}Pb separated by mylar and Al spacers. The yield of the ^{210}Po evaporation residue (half-life of 138 days) was counted off-line after the Pb targets were dissolved and a ^{209}Po tracer was added. The absolute normalization was determined during the beam exposure period by measuring Rutherford scattering at forward angles ($\theta_{lab} < 30°$). However, the results have not yet been published as of the end of 2015.

In addition to the elastic scattering and transfer/breakup data discussed above, Lemasson *et al.* have also reported on fusion of ^{8}He with ^{197}Au [55] and ^{65}Cu [56] using on-line measurements of characteristic γ radiation. Surprisingly, the ^{197}Au fusion excitation function turned out to be very similar to that measured for ^{6}He incident on the same target [57]. Both display larger cross sections than those for ^{4}He + ^{197}Au [58]. However, when scaled according to the procedure described in refs. [31, 32], the sub-barrier fusion was only mildly enhanced and above-barrier fusion was suppressed as might be expected from the large transfer yields reported in ref. [53]. The ^{65}Cu fusion data [56], taken at energies well above the Coulomb barrier, displayed a somewhat different behav-

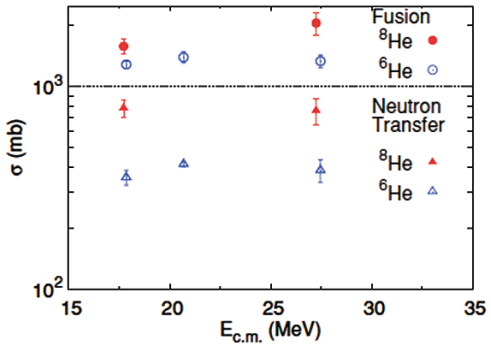

Fig. 8. Excitation functions for fusion and transfer in the ^{8}He+^{65}Cu system. Note the very large yield for neutron transfer. The comparison ^{6}He + ^{65}Cu cross sections were taken from refs. [59,60]. Figure reprinted with permission from ref. [56]. © 2010, The American Physical Society.

ior. When compared with ^{6}He data on the same target, the ^{8}He cross sections were considerably greater than those for ^{6}He, as were the neutron transfer cross sections (fig. 8).

4 Reactions with ^{8}Li

Although the short-lived radioactive nucleus ^{8}Li is not considered to be exotic, its low 1n separation energy threshold of 2.03 MeV means that it is a weakly-bound nucleus, as are the stable isotopes ^{6}Li and ^{7}Li. The main motivation of the many experiments performed with ^{8}Li beams is its role in primordial nucleosynthesis (see, *e.g.*, ref. [61]). Another important motivation, more related to the scope of this review, is the investigation of the effect of the different cluster configurations between the Li isotopes: $^8\text{Li} = {}^7\text{Li} + \text{n}$ (BE = 2.033 MeV), $^7\text{Li} = \alpha + \text{t}$ (BE = 2.467 MeV), $^6\text{Li} = \alpha + \text{d}$ (BE = 1.474 MeV). The role of neutron stripping in the elastic scattering and fusion reaction has also been studied. For instance, the difference in the neutron separation threshold, S_n, for the ^{8}Li, ^{7}Li and ^{6}Li isotopes (2.03 MeV, 7.25 MeV and 5.66 MeV, respectively) can provide a different interplay between transfer and breakup in coupled-channels treatment of elastic scattering and fusion data.

In-flight beams of ^{8}Li at low energy have been obtained with relatively good intensity at small facilities such as *Twinsol* at the University of Notre Dame and *RIBRAS* at Universidade de São Paulo, and also in bigger facilities such as *EXOTIC* in the Laboratori Nationali di Legnaro. Some of the works (theoretical and experimental) involving reactions induced by ^{8}Li beams produced in these laboratories are reviewed below.

4.1 Elastic scattering of ^{8}Li

4.1.1 ^{8}Li + ^{7}Li

An angular distribution for the elastic scattering of ^{8}Li on ^{7}Li has been measured at an incident energy of 11 MeV by Howell *et al.* [62] at both forward and backward angles. The angular distribution was very well described by an optical-model analysis using a Woods-Saxon potential. At forward angles elastic scattering is the most important mechanism, while at backward angles the neutron transfer reaction, ^{7}Li(^{8}Li, ^{7}Li)^{8}Li, dominates. The interference between elastic scattering and transfer at backward angles was used to obtain the asymptotic normalization coefficient (ANC) [63] for the valence neutron in ^{8}Li, and thereby to infer the astrophysical S-factor [64] $S_{17}(0)$ for the isospin symmetric ^{7}Be(p, γ)^{8}B capture reaction.

4.1.2 ^{8}Li + ^{9}Be

Angular distributions for ^{8}Li + ^{9}Be elastic scattering have been measured at 19.6 MeV [65] and at 27 MeV [66]. In both measurements the data were well described by ^{7}Li + ^{9}Be optical-model potential parameters at similar ^{7}Li energies. An optical-model analysis with the São Paulo double-folding potential [33] was also performed for these data, giving good results. Total reaction cross sections were derived from these analyses and compared with the values for other systems with weakly-bound and stable projectiles, applying the two most-used reduction methods [31,32,67,68]. The conclusion is that reactions with non-halo light nuclear projectiles lead to similar total reaction cross sections [65].

4.1.3 ^{8}Li + ^{12}C

Two elastic-scattering experiments with ^{8}Li incident on a ^{12}C target, performed in the 1990s, were reviewed in ref. [1]. More recently, an elastic-scattering experiment was performed at an incident energy of 23.9 MeV by Barioni *et al.* [69]. Optical-model analyses with Woods-Saxon and São Paulo potentials gave a good description of the elastic data. A coupled-channels calculation, including inelastic and breakup channels, was performed and coupling effects were found to be unimportant.

4.1.4 ^{8}Li + ^{51}V

Elastic scattering of ^{8}Li + ^{51}V was measured at 18.5 MeV [65] and 26.0 MeV [9]. Optical-model analyses with Woods-Saxon and São Paulo potentials were performed and total reaction cross sections were derived from the angular distributions measured at both energies. A comparison of the total reaction cross sections with values from other light weakly- and strongly-bound projectiles on similar mass targets was carried out. Once adequate reductions were applied, a similar behavior as a function of energy was observed (fig. 9).

4.1.5 ^{8}Li + ^{90}Zr

Very recently, measurement and analysis of two angular distributions for ^{8}Li + ^{90}Zr at 18.5 and 21.5 MeV have

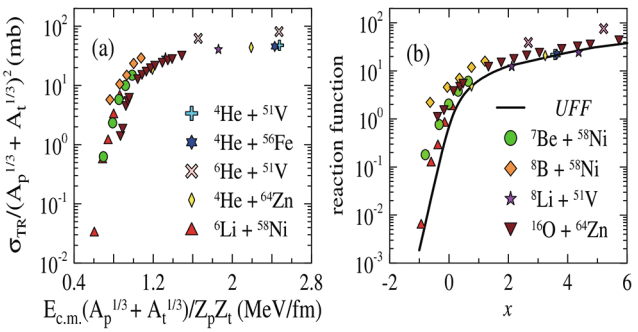

Fig. 9. Total reaction cross sections for systems with different projectiles on targets from $A = 51$ to 64, reduced using two different reduction methods. Figure from ref. [65].

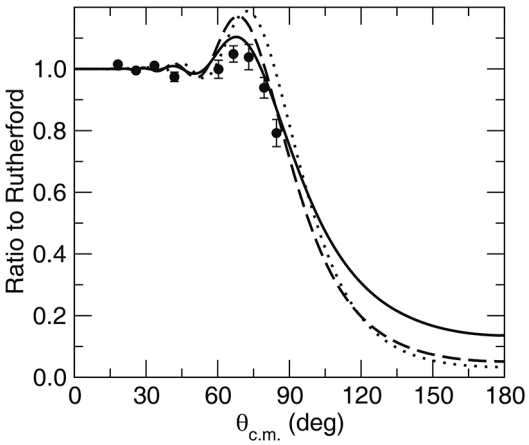

Fig. 10. Quasielastic scattering angular distribution for the ^{8}Li+^{90}Zr system at 18.5 MeV compared with no-coupling (dotted curve), CC (dashed curve), and CRC (solid curve) calculations, respectively. Figure reprinted from ref. [71] with kind permission of The European Physical Journal (EPJ).

been reported, in refs. [70] and [71]. The main goal of these measurements was to investigate the influence of the single neutron stripping reaction in the coupling scheme for quasielastic scattering. They found that the dominant contribution to the CRC (Coupled Reaction Channel) calculation was neutron stripping: ^{90}Zr(^{8}Li, ^{7}Li)^{91}Zr.

Figure 10 shows the comparison of this calculation with the experimental angular distribution measured at 18.5 MeV. Total reaction cross sections for the two energies were also determined from the analysis and compared with several other similar systems with similar projectile and target mass, applying the reduction suggested in refs. [31,32] but replacing σ_F by σ_R. The results indicate that the total reaction cross sections exhibit rather similar behavior as a function of the reduced energy at higher energy. For lower energy, however, some differences among the systems appear. They attributed the difference between the UFF function and the best fit to the data to a possible role of direct reactions, and determined the ratio of the direct to total reaction cross section for ^{8}Li on several targets. The conclusion was that direct reactions are very important at energies below the Coulomb barrier.

4.1.6 ^{8}Li + ^{208}Pb

The only existing data on ^{8}Li + ^{208}Pb elastic scattering were already reviewed in ref. [1]. However, the role of the neutron stripping channel in the ^{8}Li + ^{208}Pb elastic scattering has been investigated by Keeley in ref. [72]. The author of this work performed a full CRC calculation for the quasielastic barrier distribution of this system and compared with that for ^{6}He + ^{208}Pb. For ^{8}Li, the effect of the single-neutron transfer coupling was to move the peak of the barrier distribution to lower energies, while the effect in ^{6}He was to split the barrier distribution into two distinct peaks, one at lower energy and one at higher energy. These are actually schematic calculations and the observed structures in the barrier distributions can be washed out in the measurements due to other possible couplings, such as to breakup channels.

4.2 Transfer reactions induced by ^{8}Li

Proton and neutron transfer reactions with a ^{8}Li projectile have been measured on ^{9}Be and ^{12}C targets. The ^{9}Be(^{8}Li, ^{9}Be)^{8}Li proton transfer reaction was measured at 27 MeV and reported in ref. [66]. In this work, the spectroscopic factor for the $\langle ^9\mathrm{Be}_{gs}|^8\mathrm{Li}_{gs} + \mathrm{p}\rangle$ bound system was obtained from a comparison between the experimental differential cross sections for the transfer reaction and finite-range distorted-wave Born approximation (FRDWBA) calculations, assuming a direct transfer and using the code FRESCO [73,74]. The spectroscopic factor was then used to infer information concerning the ^{8}Li(p, γ)^{9}Be proton capture reaction. The transfer reactions ^{9}Be(^{8}Li, ^{7}Li)^{10}Be and ^{9}Be(^{8}Li, ^{9}Li)^{8}Be, measured in the same experiment, were published in ref. [75]. The $\langle ^9\mathrm{Li}_{gs}|^8\mathrm{Li}_{gs} + \mathrm{n}\rangle$ and $\langle ^8\mathrm{Li}_{gs}|^7\mathrm{Li}_{gs} + \mathrm{n}\rangle$ spectroscopic factors were obtained from a comparison between the experimental differential cross sections and FRDWBA calculations. Cross sections for the direct neutron-capture reactions ^{7}Li(n, γ)^{8}Li and ^{8}Li(n, γ)^{9}Li were then deduced in the framework of a potential model [76] using these spectroscopic factors.

Transfer reactions have also been measured on ^{12}C. The ^{12}C(^{8}Li, ^{7}Li) and ^{12}C(^{8}Li, α) reactions were measured in the early 1990s. The latter was confirmed to be due to two-body transfer rather than a fusion-evaporation mechanism [77]. More recently Barioni *et al.* [69] took advantage of the higher cross section for the ^{12}C(^{8}Li, ^{9}Be)$^{11}\mathrm{B}_{gs}$ proton transfer reaction to obtain the spectroscopic factor for $\langle ^9\mathrm{Be}_{gs}|^8\mathrm{Li}_{gs} + \mathrm{p}\rangle$. The results were compared with shell-model calculations and previous data and good agreement was observed.

4.3 Fusion of ^{8}Li

Fusion of ^{8}Li on ^{208}Pb was measured at the University of Notre Dame for energies between 32 and 37.5 MeV (center-of-momentum), corresponding to between 3 and 8.5 MeV above the Coulomb barrier [78]. The excitation function

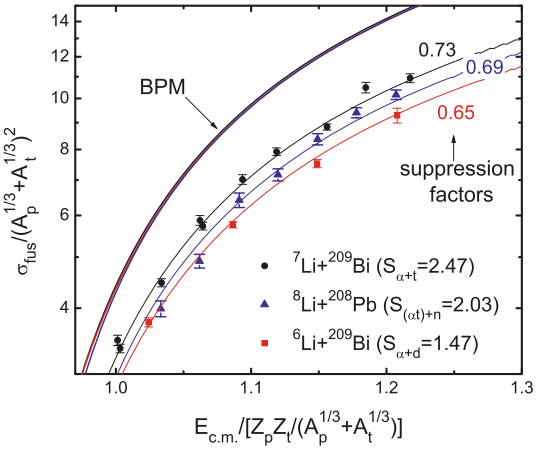

Fig. 11. Reduced complete fusion (CF) cross sections for ^{8}Li+^{208}Pb. The breakup threshold energies for ^{6}Li, ^{7}Li and ^{8}Li are indicated, in MeV. Figure reprinted with permission from ref. [78]. © 2009, The American Physical Society.

for complete fusion (CF) of this system (fig. 11) was obtained by detecting delayed α-particle emission from the ^{211,212}At residual nuclei (after 5n and 4n evaporation from the compound nucleus, respectively).

The experimental results were compared with one-dimensional barrier-penetration model (BPM) calculations and PACE2 [79] predictions. A suppression of about 30% was observed for energies above the barrier. Using the above comparison, the roles of CF and ICF (incomplete fusion) reactions were disentangled. ICF due to the fusion of the heavier ^{7}Li fragment from the breakup of ^{8}Li was estimated and found to be important for the higher energies. A comparison with fusion data for other Li isotopes was also performed by applying the appropriate scaling factors of $(A_p^{1/3}+A_t^{1/3})^2$ and $Z_pZ_t/(A_p^{1/3}+A_t^{1/3})$ for the cross sections and energies, respectively. Some correlation between the suppression factor used to adjust the BPM calculation to the experimental data for each isotope, ^{6}Li, ^{7}Li and ^{8}Li, and the threshold breakup energies of the projectiles was observed, as shown in fig. 11.

5 Reactions with ^{9}Li

Since ^{9}Li is a short-lived radioactive nucleus with one-neutron separation energy $S_n = 4.064$ MeV, it may be considered to be weakly bound. Very few experiments have been carried out with this nucleus as projectile, and most of those were performed in association with the famous halo isotope ^{11}Li. There is, however, some intrinsic interest in elastic-scattering measurements with ^{8,9}Li, related to the relative importance of the one-neutron-transfer and breakup mechanisms. Previous elastic-scattering experiments, reviewed in ref. [1], were performed at relatively high energy beyond the scope of the present review. However, a recent elastic experiment was performed with both ^{9}Li and ^{11}Li beams produced by fragmentation and post-accelerated at the ISAC-II line at the TRIUMF facility (Vancouver, Canada) [80]. Fusion experiments induced by ^{9}Li on ^{70}Zn and on ^{208}Pb have also been performed at the same facility and are reviewed below.

5.1 Elastic scattering of ^{9}Li

Angular distributions were measured for ^{9}Li + ^{208}Pb at center-of-mass (c.m.) energies of 23.1 and 28.3 MeV [81], corresponding to a little below and a little above the barrier for this system. The lower energy angular distribution showed a typical Rutherford scattering characteristic, as expected. The higher energy angular distribution, however, displayed Coulomb-nuclear interference, with a maximum at $\theta = 75°$ and a smooth decrease beyond that angle. This was interpreted as a typical Fresnel-type pattern, characteristic of the scattering of ordinary stable nuclei near the Coulomb barrier. This result was used to compare with data for the more exotic ^{11}Li projectile as discussed in sect. 6.1 below.

5.2 Fusion of ^{9}Li

Fusion measurements induced by ^{9}Li beams have been performed at ISAC-TRIUMF on ^{70}Zn [82] and ^{208}Pb [83] targets. In both experiments, enhancement of the fusion cross section for energies below the barrier and suppression above the barrier was observed. The below-barrier enhancement for ^{9}Li + ^{70}Zn remains a challenge for theoretical calculations. The role of neutron transfer, which is usually the main motivation to investigate reactions with Li isotopes, was explicitly considered by Zagrebaev *et al.* [84] in a standard coupled-channels calculation. This particular calculation did not describe the data, and the possible role of dineutron transfer was postulated. Later, Balantekin and Kocak [85] reported a coupled-channels calculation with the inclusion of coupling to additional inelastic channels. Unfortunately, this calculation also failed to reproduce the low-energy enhancement in ^{9}Li + ^{70}Zn fusion. The authors then proposed a very sophisticated mechanism in which a molecule with two cores, ^{9}Li and ^{68}Zn, might be formed and share and exchange two neutrons thereby forming ^{11}Li and ^{70}Zn.

The role of the 2n-transfer process was also explicitly taken into account in a quantum diffusion approach by Sargsyan *et al.* [26]. In contrast to the calculation of Balantekin [85], they considered a 2n-stripping reaction to the target, ^{70}Zn(^{9}Li, ^{7}Li)^{72}Zn, which is expected to be much more favorable ($Q_{2n} = 8.6$ MeV) than the 2n-pickup reaction ^{70}Zn(^{9}Li, ^{11}Li)^{68}Zn ($Q_{2n} = -15.4$ MeV). The agreement with the ^{9}Li + ^{70}Zn fusion data was improved, but the lowest point in the excitation function could still not be reproduced (fig. 12). This data set still deserves further experimental and theoretical investigation.

Data on fusion of ^{9}Li + ^{208}Pb were reported as a function of energy by Vinodkumar *et al.* [83]. They detected the decay α particles emitted by the evaporation residues ($^{214-211}$At) using a beam on/beam off method. The fusion cross sections were estimated from statistical model

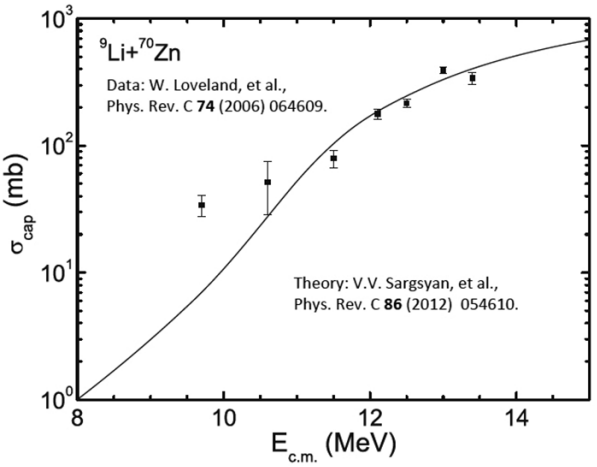

Fig. 12. Fusion (capture) cross section for the $^9\mathrm{Li} + {}^{70}\mathrm{Zn}$ system. The data are from ref. [82]. The solid line is the result of a quantum diffusion calculation [26].

calculations. This data set was compared with the predictions of coupled-channels calculations using the code CCFULL [86]. Only the important inelastic channels were included. The results of this calculation, as well as a one-dimensional barrier-penetration calculation, underestimated the sub-barrier fusion cross sections and overestimated the above-barrier cross sections, indicating that the description of the fusion of ^{9}Li is yet to be understood. On the other hand, the authors also compared the fusion data for $^9\mathrm{Li} + {}^{208}\mathrm{Pb}$ with that for ^{6}Li, ^{7}Li, and ^{8}Li available in the literature. Considering the reduced cross sections ($\sigma_{fus}/\pi R_B^2$) as a function of reduced energy ($E_{c.m.}/V_B$), they found no obvious difference in behavior for the ^{9}Li projectile. The role of the breakup and transfer was not explicitly considered in any of these calculations, and these could provide further insights.

6 Reactions with ^{11}Li

The ^{11}Li nucleus is the most fascinating case, and the archetype, of a Borromean halo nucleus. Its low binding energy for the di-neutron ($S_{2n} = 0.369\,\mathrm{MeV}$) generates an extended mass distribution going well beyond its core. Also, due to the loosely bound structure, the di-neutron halo can be easily polarized by the strong electric field of a heavy target such as ^{208}Pb. This polarization would correspond to a distortion of the halo nucleus in which the positively charged core would move away from the target and the halo neutrons would move in the opposite direction. The large $E1$ transition strength observed in the Coulomb dissociation measurement of ^{11}Li [87] corroborates this possibility. Recently, a reliable beam of ^{11}Li became available at the post-accelerated ISAC-II line of the TRIUMF facility (Vancouver, Canada). The intensity achieved for this beam was about 5×10^3 particles/s, enough for elastic-scattering [81], breakup [88], and fusion [89] measurements on a ^{208}Pb target. These measurements are reviewed below.

6.1 Elastic scattering

The strong dynamic polarizability for ^{11}Li in the presence of the electric field of a heavy target can give rise to a long-range Coulomb interaction whose effect would be to reduce the elastic-scattering cross sections even at energies well below the barrier. This possibility was addressed by Cubero *et al.* in ref. [81], which reported the first measurement of the scattering of ^{11}Li on a ^{208}Pb target at incident energies of 24.3 and 29.8 MeV. These are, respectively, below and above the Coulomb barrier ($V_{barrier} = 28\,\mathrm{MeV}$). In this work, they also reported on the elastic scattering of $^9\mathrm{Li} + {}^{208}\mathrm{Pb}$ with the same setup and at the same c.m. energies of 23.1 and 28.3 MeV. This comparison is important to highlight the different characteristics of the elastic scattering of the ^{9}Li and ^{11}Li nuclei, and to disentangle the contribution of the loosely-bound structure of ^{11}Li. Actually, the large polarizability of ^{11}Li was already predicted years earlier by Andrès and Gómez-Camacho [90]. They also predicted a strong reduction of the elastic cross section for ^{11}Li.

This strong reduction in the elastic cross section was then experimentally corroborated in the paper of Cubero *et al.* [81]. To investigate this effect in a more quantitative way, they considered the comparison of four-body CDCC calculations with and without coupling to the continuum. The three-body description of the borromean ^{11}Li projectile was based on the idea used to describe the other borromean nucleus, ^{6}He [91]. It is well known that coupling to the continuum allows the evaluation of projectile breakup effects on the elastic scattering. The results of such calculations for the ^{11}Li data can be seen in fig. 13 as the dotted and solid curves. In this figure, a strong cross section reduction can be observed for the 4-body CDCC calculation in the "no-coupling" case, where the extended size of ^{11}Li was taken into account. However, although the cross section decreased faster than the ^{9}Li data beyond 90°, it still was not sufficient to describe the data. A good description was achieved when coupling to continuum was incorporated into the calculation. The final reduction was then attributed to the strong dipole coupling between the ground and continuum states. They also concluded that inclusion of the low-lying dipole resonance, which is close to the breakup threshold for ^{11}Li, into the calculation improved the description of the data. Keeley *et al.* [92] simplified these CDCC calculations by employing a two-body di-neutron model for the ^{11}Li nucleus. They claimed that, in principle, this approach would have all the essential physics to investigate the influence of the continuum states on ^{11}Li elastic scattering. In addition to this model applied for ^{11}Li, they also considered dynamic polarization potentials (DPPs) using the trivially equivalent local potential (TELP) derived from the CDCC calculations associated with optical-model analysis. The agreement between the calculations and the data indicated that this methodology could well represent the effects of the large dipole polarizability in describing the ^{11}Li elastic data.

A different approach to analyze the ^{11}Li data on elastic scattering has been reported in refs. [93,94]. In these pa-

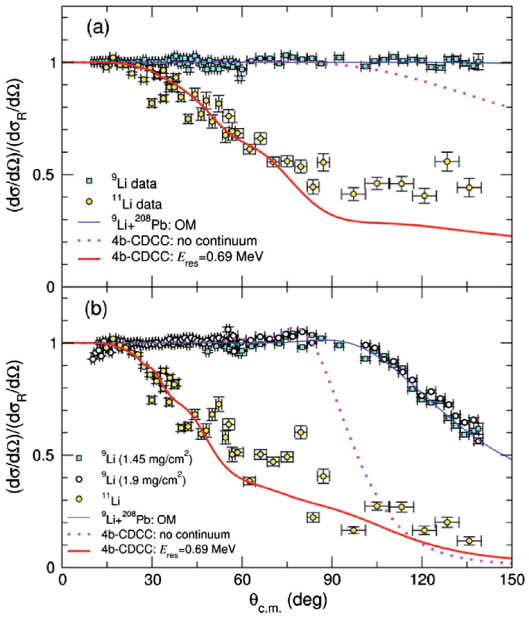

Fig. 13. Elastic-scattering cross section (ratio-to-Rutherford) for ^{9}Li and ^{11}Li on a ^{208}Pb target at the same c.m. energies of 23.1 MeV (upper panel) and 28.3 MeV (lower panel). The curves are the results of calculations with a standard optical-model potential (thin blue line), 4-body CDCC with no continuum (dotted line), and 4-body CDCC including the continuum (solid red line). Figure reprinted with permission from ref. [81]. © 2012, The American Physical Society.

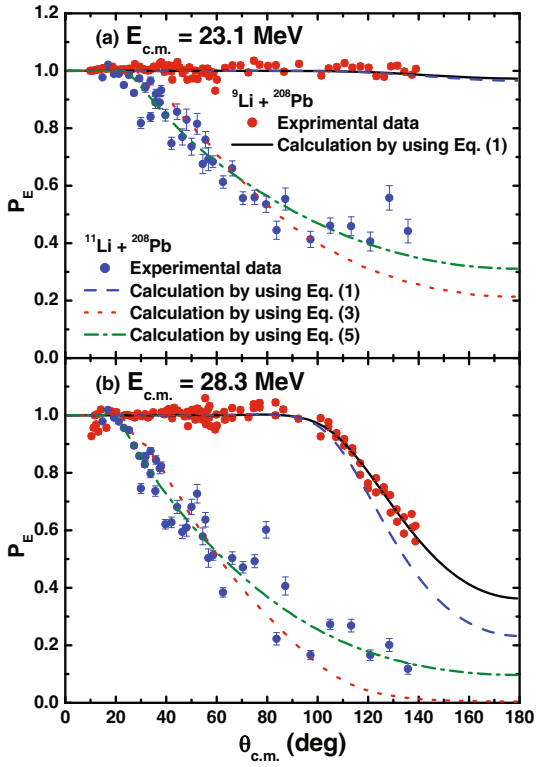

Fig. 14. Elastic-scattering cross section ratio to Rutherford for ^{9}Li and ^{11}Li on a ^{208}Pb target. The curves are the results of calculations with a standard Optical-Model (OM) potential for ^{9}Li (black line) or ^{11}Li (dashed blue line), with DPP (dotted red line) and with an extra long-range nuclear potential (dot-dashed green line). Figure reprinted with permission from ref. [93]. © 2014, The American Physical Society.

pers, the effect of ^{11}Li polarizability was investigated using long-range potentials. A dynamic polarization potential (DPP) was used to simulate the Coulomb dipole excitation (CDE) or electric dipole polarization for ^{11}Li, where the charged ^{9}Li core is decelerated by the effect of the Coulomb field of the heavy target while the valence neutrons move in a straight-line direction. The DPP was obtained using a Coulomb dipole strength $B(E1) = 1.42$ and 1.41 e^2 fm^2, at $E_{c.m.} = 23.1$ and 28.3 MeV, respectively, and a dipole resonance with energy $\epsilon = 0.69$ MeV. In the analysis, they incorporated an extra-long-range complex nuclear potential in an attempt to improve the agreement between calculation and the data.

The results of such calculations can be seen in fig. 14, where eq. (1) stands for optical model with a short-range complex potential given by the usual Woods-Saxon function, eq. (3) included the Coulomb dipole excitation (CDE) for ^{11}Li and eq. (5) has an additional complex nuclear potential of Woods-Saxon type with large diffuseness parameters to simulate a long-range interaction. In the analysis of ref. [94] the authors used a DPP taking into account the $B(E1)$ strength value from experimental data on ^{11}Li breakup [87]. Due to the spreading of the data it is not possible to disentangle the relative importance of the inclusion of the extra nuclear potential. More recently, another analysis in terms of an OM has been performed by Fernández-García *et al.* [95]. In this work, the authors combined a double-folding potential, the São Paulo Potential (SPP), and a long-range polarization potential. They used more realistic densities for ^{9}Li and ^{11}Li from proton scattering measurements [96], and the experimental $B(E1)$ distribution from the Coulomb dissociation measurement [87], to obtain both the short- and long-range potentials. Considering only the double-folding SPP in the form of $U_{opt} \approx V_{SPP} + i(0.78V_{SPP})$, without any long-range potential, the calculation for the ^{9}Li + ^{208}Pb system agrees very well with the experimental angular distribution. For the ^{11}Li + ^{208}Pb system it was necessary to include a long-range Coulomb Dipole Potential (CDP). The good agreement between the calculation and data indicates the dominance of the Coulomb dipole polarizability for ^{11}Li. The long-range absorptive tail of the ^{11}Li imaginary CDP extends to a very large radius, suggesting that the Coulomb breakup of ^{11}Li takes place much further from the target. Although there was a good description of the data with these calculations, the role of the halo structure of ^{11}Li is not completely understood. The presence of the strong soft electric dipole ($E1$) response at low excitation energies for ^{11}Li due to Coulomb excitation is clear. However, the existence of a low-energy dipole resonance in ^{11}Li [97], and what would be its contribution in the $B(E1)$ strength and thus in the elastic scattering, deserves further investigation.

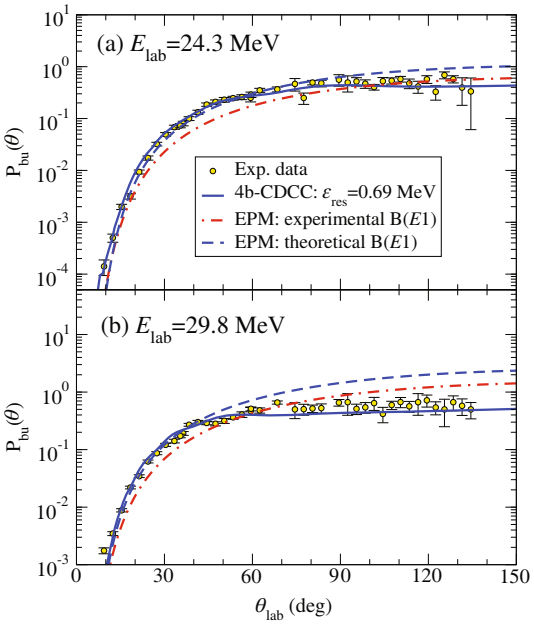

Fig. 15. Angular distribution of the ^{11}Li breakup on a ^{208}Pb target at (a) 24.3 MeV and (b) 29.8 MeV. The solid line represents the 4b-CDCC calculation and the dashed and dot-dashed lines are the semi-classical calculation with theoretical and experimental $B(E1)$ distribution, respectively. Figure reprinted with permission from ref. [88]. © 2013, The American Physical Society.

6.2 Breakup of ^{11}Li

Breakup reactions play a significant role in the investigation of halo structure in nuclei. From the direct measurement of breakup cross sections, we can infer and better understand the exotic structure caused by the weakly-bound nature of valence neutrons in halo nuclei. Both Coulomb and nuclear breakup are important in the spectroscopy of halo nuclei since the observables are strongly correlated with their ground and continuum structure. Two decades after the first confirmation of halo structure in ^{11}Li, several breakup-reaction measurements of halo nuclei have been performed, and some of them are reviewed here. However, only two experiments involving ^{11}Li as a projectile have been performed, one at high energy in RIKEN, reported in ref. [87], and the other at TRIUMF measured at an energy around the Coulomb barrier and reported in ref. [88]. Both measurements were performed with a ^{208}Pb target, which in principle would probe Coulomb breakup. Although important for the investigation of the low-lying resonances in ^{11}Li, the experiment performed at RIKEN is outside the scope of our review.

The experiment performed at TRIUMF corresponds to an inclusive angular distribution measurement for the breakup of $^{11}\text{Li} + {}^{208}\text{Pb}$ at 24.3 and 29.8 MeV. The setup was composed of 4 telescopes placed around the ^{208}Pb target, covering a large angular range from 10 to 140 degrees. The telescopes consisted of ΔE-E double-sided Si strip detectors (DSSSD). The ^{9}Li fragments from the breakup of ^{11}Li were clearly separated and could be easily identified in a two-dimensional ΔE *vs.* $\Delta E + E$ plot.

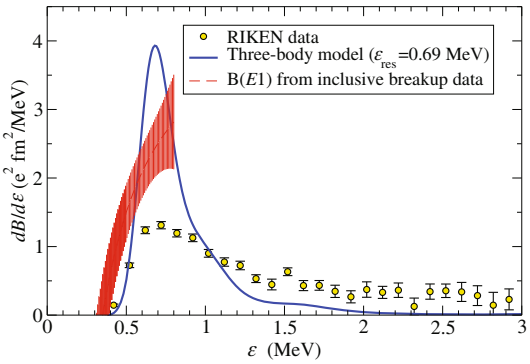

Fig. 16. $B(E1)$ distributions of ^{11}Li. The circles represent the experimental data from ref. [87], the solid line is the result of the extraction from the full CDCC calculation including the dipole resonance at $\epsilon = 0.69$ MeV above the ground state and the shaded area is the result of a calculation where the $B(E1)$ distribution was assumed to be a linear function of the excitation energy given by eq. (5) in ref. [88]. Figure reprinted with permission from ref. [88]. © 2013, The American Physical Society.

The experimental angular distributions are shown in fig. 15 together with the results of a 4b-CDCC calculation, using a ^{11}Li model similar to the one proposed for ^{6}He in ref. [91]. As can be seen in the figure, this 4b-CDCC calculation reproduced the data quite well. This good agreement, in particular at forward angles ($\theta < 60°$), indicates the validity of the semiclassical approximation and the dominance of $E1$ couplings. The figure shows the results of semiclassical Coulomb excitation theory as described in ref. [98], where three-body theoretical (dashed line) and experimental (dot-dashed line) $B(E1)$ distribution were used. As can be seen in the figure, the latter calculation did not reproduce the data. The authors also used the results of the full 4b-CDCC calculation, which better described the data, to extract the $B(E1)$ distribution. It is important to mention that the three-body model used to describe ^{11}Li predicted the existence of a low-lying dipole resonance, but its energy was adjusted to $\epsilon_x \sim 0.69$ MeV above the ground state, or 0.32 MeV above the 2n breakup threshold. The comparison of the $B(E1)$ distributions obtained from the breakup data from RIKEN [87], from the 4b-CDCC calculation, and from a linear approximation using the inclusive breakup data from TRIUMF, can be seen in fig. 16. The authors claimed that their methodology can be used to obtain the binding energy of other weakly bound nuclei from inclusive breakup angular distributions.

6.3 Fusion of ^{11}Li

When it comes to fusion reactions, the relevant question is whether fusion at energies near the Coulomb barrier is enhanced, owing to the large extent of the nuclear matter distribution, or hindered due to the very low threshold of the breakup channel. Since ^{11}Li is a nucleus with more-diffuse density and a high probability of breakup,

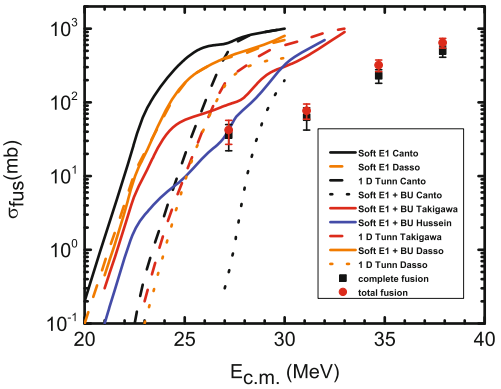

Fig. 17. Fusion excitation function for the ^{11}Li+^{208}Pb system. The several lines correspond to predictions from refs. [100–104] and the symbols are the data from ref. [89]. Figure reprinted with permission from ref. [89]. © 2013, The American Physical Society.

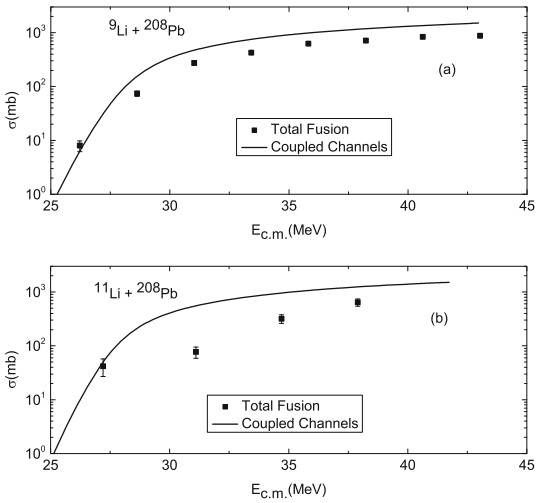

Fig. 18. Fusion excitation functions for the ^{9,11}Li+^{208}Pb systems. The solid lines are predictions of the total interaction cross section from coupled-channel calculations. The data are for the total fusion of ^{9,11}Li+^{208}Pb. Figure reprinted with permission from ref. [89]. © 2013, The American Physical Society.

interest in its fusion reaction was quite high. It was not so long after the measurement of the large interaction cross section for ^{11}Li by Tanihata *et al.* [99] that theoreticians started making predictions for the fusion excitation function of ^{11}Li + ^{208}Pb. Considering different approaches such as the influence of the soft Coulomb dipole, the breakup channel, and one-dimensional tunneling, Canto [100], Takigawa [101], and Hussein [102,103] used an optical-model approach with a polarization potential to take into account the breakup channel. Dasso [104] used a coupled-channel approach with breakup as one channel. Their predictions are summarized in fig. 17.

These predictions varied by up to one order of magnitude so the need for data was clear. The only fusion measurement induced by a ^{11}Li beam was very recently performed at the ISAC2 facility at TRIUMF on a ^{208}Pb target [89]. In this experiment, the 40 MeV post-accelerated ^{11}Li beam, with an intensity of about 10^3 pps, impinged on a stack of ^{208}Pb targets. The α-particle emission yields from fusion-evaporation residues ($^{212-216}$At) were used to obtain the fusion cross section. The beam was pulsed on for 5 ns and then data were collected during a 172 ns beam-off period. The incident c.m. energy spanned from 27.1 to 37.9 MeV, covering a region from below to above the nominal Coulomb barrier. The data are plotted in fig. 17, together with the theoretical predictions.

The main motivation for these studies was related to the role of breakup and other reaction channels in terms of enhancing or reducing the fusion yield. Breakup of the incident ^{11}Li results in incomplete fusion (ICF), where the ^{9}Li fragment fuses with the target. It is very difficult to experimentally separate ICF from complete fusion (CF). However, based on a previous fusion measurement for the ^{9}Li + ^{208}Pb system [83], the authors claimed to have disentangled the contribution of CF from the total fusion (CF+ICF), shown separately in fig. 17. Although it was claimed that the contribution of ICF was quite large, the data were still overestimated by all the previous predictions. The authors also reported a new coupled-channels calculation where they considered the optical-model parameters from the elastic-scattering measurement for ^{9,11}Li with ^{208}Pb [81]. The results of these new calculations are shown in fig. 18, and as one can see, they still overestimate the data for both ^{9,11}Li+^{208}Pb systems at energies above the Coulomb barrier. In ref. [89], a comparison plot of the reduced fusion cross sections, $\sigma_{fus}/\pi R_R^2$, for all the lithium isotopes ^{6,7,8,9,11}Li as a function of $E_{c.m.}/V_B$ was also given. The differences could be attributed to geometry for the $^{6-9}$Li isotopes, but not for ^{11}Li. It is clearly important to have an improved ^{11}Li beam intensity, and fusion measurement on other targets, to achieve a better understanding of fusion induced by ^{11}Li.

7 Reactions with ^{7}Be

^{7}Be lies on the proton-rich side of the line of nuclear stability and it is weakly bound, with a separation energy of 1.59 MeV for breakup into ^{3}He and ^{4}He. It is a radioactive nucleus with a half-life of 53.2 d and the fact that it is the core for the proton-halo nucleus ^{8}B enhances its own interest. In ref. [1], elastic scattering and reaction data for ^{7}Be on targets of ^{7}Li, ^{10}B, ^{12}C, ^{14}Ni, ^{27}Al, ^{58}Ni, and ^{238}U were reviewed. Data appearing later will be emphasized here.

7.1 Elastic scattering of ^{7}Be

The elastic-scattering studies performed so far with a ^{7}Be projectile seem to indicate only small effects of bu couplings, although sizable effects appear for energies above 12 MeV per nucleon (sect. 7.1.2). In spite of being a weakly bound nucleus, a behaviour characteristic of the breakup threshold anomaly does not seem to apply to reactions with ^{7}Be (sect. 7.1.6). Recent experiments leading to these conclusions are reviewed below.

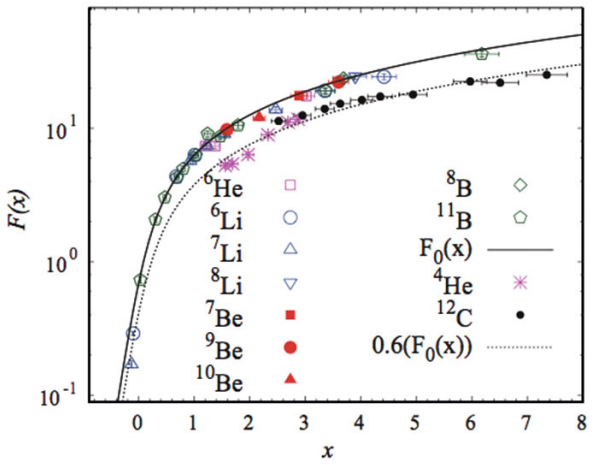

Fig. 19. Reduced total reaction cross sections for several light projectiles on ^{12}C. Figure reprinted with permission from ref. [110]. © 2011, The American Physical Society.

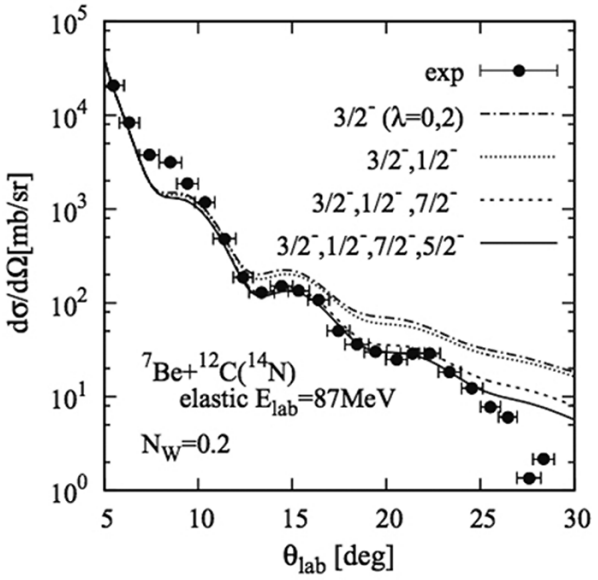

Fig. 20. Elastic-scattering angular distribution for ^{7}Be on melamine ($C_3N_6H_6$) at 87.7 MeV [112] and respective coupled-channel calculations. Figure reprinted with permission from ref. [113]. © 2010, The American Physical Society.

7.1.1 ^{7}Be + ^{9}Be

Quasi elastic scattering angular distributions for this system were reported in refs. [105,106] for energies E_{lab} of 17, 19 and 21 MeV in the angular range $24° \leq \theta_{c.m.} \leq 57°$. These, along with similar data for ^{7}Li + ^{9}Be taken from the literature, were analyzed within the CRC scheme in ref. [107]. Inelastic excitations, reorientation of projectile and target nuclei as well as the most relevant transfer channels were included in the CRC calculations. The data for both systems could be well described with very similar energy-dependent OM potentials. The authors concluded that potential scattering and reorientation of projectile and target are the most important mechanisms in both cases, with the former (latter) mechanism dominating at forward (backward) angles.

A quasielastic angular distribution for the same system at $E_{lab} = 23.7$ MeV was reported in ref. [108], covering the angular range between 12.3 and 38.8 degrees in the laboratory frame of reference. An absolute normalization was not obtained from the experiment, so the data were normalized to optical-model predictions. Coupled-channel calculations with and without couplings to the continuum gave very similar results.

7.1.2 ^{7}Be + ^{12}C

Angular distributions for the elastic scattering of ^{7}Be+^{12}C at $E_{lab} = 18.8$ MeV were measured at Notre Dame [109] and São Paulo [110]. The two data sets, corresponding to different angles that complement each other, gave consistent results and were well described by optical-model calculations using Woods-Saxon potentials. By analyzing both data sets together, a total reaction cross section of 1198 mb was deduced in ref. [110]. In order to investigate possible effects of bu couplings, CDCC calculations were performed [110] where the ^{7}Be nucleus was considered as formed by ^{3,4}He clusters. The effects of the couplings were found to be small. Using the "fusion function" type of data reduction described earlier (sect. 2.2.2), but applied now to total reaction cross sections, data for projectiles of ^{4,6}He, ^{6,7,8}Li, ^{7,9,10}Be, ^{8,11}B and ^{12}C on ^{12}C targets were plotted together (fig. 19). All reaction cross section data fell on a trajectory described by the Universal Fusion Function ($F_0(x)$), except those corresponding to the ^{4}He and ^{12}C projectiles which were suppressed by a factor of 0.6. The high proton and neutron separation energies of the latter projectiles could be the reason for the observed suppression. An angular distribution for quasielastic scattering of ^{7}Be + ^{12}C at $E_{lab} = 34$ MeV was reported in ref. [111]. These data were used to obtain the OM potential needed for a DWBA calculation of the ^{12}C(^{7}Be, ^{3}He) reaction, which was the reaction of primary interest in this work. No further analysis of the elastic-scattering data was done.

In ref. [112], data for elastic scattering at 87.7 MeV were reported for ^{7}Be on a melamine target (which has a ratio of 0.5 to 1 for ^{12}C to ^{14}N). These data were later theoretically analyzed in ref. [113], where a ^{4}He+^{3}He cluster structure was assumed for ^{7}Be and a coupled-channel calculation was performed including its ground and first bound states ($\frac{3}{2}^-$, $\frac{1}{2}^-$) as well as the first two resonant states ($\frac{7}{2}^-$, $\frac{5}{2}^-$). As shown in fig. 20, the inelastic couplings have an important effect at backward angles, with the excitation of the $\frac{7}{2}^-$ resonant state making the most significant contribution.

7.1.3 ^{7}Be + ^{14}N

The available data for this system refer to the melamine target mentioned in the previous section (reported in ref. [112]) and have been reviewed in ref. [1].

7.1.4 ^{7}Be + ^{27}Al

In addition to the data of ref. [114], which were reviewed in ref. [1], elastic-scattering angular distributions for this system have been reported in ref. [115] for $E_{lab} =$ 10.0, 13.8, 15.2, and 15.4 MeV. Optical-model fits to the data yielded total reaction cross sections of 171 ± 92, 737 ± 81, 951 ± 70, and 998 ± 74 mb, respectively. Although inelastic yields corresponding to excitation of the lowest-lying states of projectile and target would in principle also contribute to the data, coupled-channel calculations indicated that such contribution can be neglected. The above cross sections were obtained by using potentials with real and imaginary parts proportional to the São Paulo potential: $V = N_R V_{SPP}$, $W = N_I V_{SPP}$. A good description of the data was achieved, but normalization factors different from the most usual values ($N_R = 1$, $N_I = 0.78$) were generally needed to fit the data. Using two different data reduction procedures, a comparison of reaction cross sections was performed between systems having the same ^{27}Al target and projectiles of ^{6}He, ^{6,7}Li, ^{7,9}Be and ^{16}O, but no definitive conclusion could be drawn. This is actually consistent with part of the conclusions of a recent revision of the most frequently used methods of data reduction [116], where it was warned that these methods in general do not perform well when applied to reaction cross sections and should only be used with some caution.

7.1.5 ^{7}Be + ^{51}V

An elastic-scattering angular distribution for the ^{7}Be+^{51}V system at 26 MeV was reported in ref. [117]. An OM fit using the São Paulo potential gave a good description of the data, yielding a total reaction cross section of 1210 mb.

7.1.6 ^{7}Be + ^{58}Ni

As reviewed in ref. [1], experimental angular distributions for quasielastic scattering of this system (including inelastic excitation of the 0.43 MeV state in ^{7}Be) were reported in ref. [118], for E_{lab} energies of 15.1, 17.1, 18.5, 19.9, and 21.4 MeV. New measurements were recently reported at $E_{lab} =$ 21.5 Mev in ref. [119] where, in addition to the quasielastic-scattering data, angular and energy distributions of the ^{3,4}He residues produced in the reaction also were detected (these will be further discussed in sect. 7.2). The quasielastic data included in principle inelastic yields corresponding to population of the 0.43 (1.45) MeV excited state of the projectile (target), but the estimated contributions were small (negligible), respectively. A comparison with the data of ref. [118] at 21.4 MeV shows a remarkably good agreement, as seen in fig. 21. Optical-model and CDCC calculations, both with no free parameters, gave satisfactory descriptions of the data. A ^{3}He+^{4}He cluster structure was assumed for ^{7}Be in the latter calculations and the involved interaction potentials were obtained from independent experimental data. The optical-model calculations, represented with the solid curve in fig. 21,

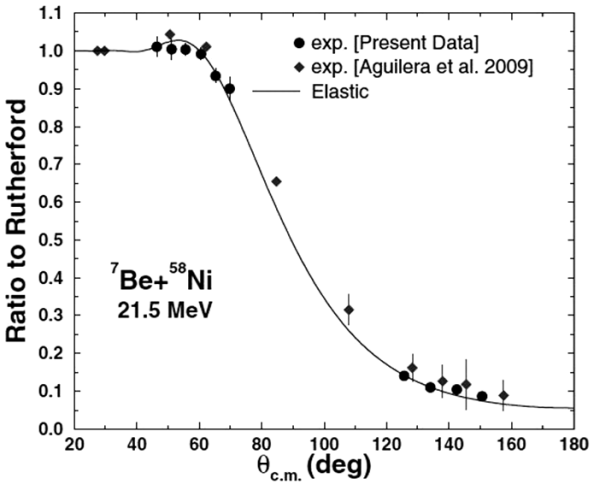

Fig. 21. Quasielastic-scattering angular distribution for ^{7}Be + ^{58}Ni at 21.5 MeV. Circles are from ref. [119] while diamonds are from [118]. The solid line corresponds to an optical-model calculation using a global potential parametrization for ^{7}Li. Figure reprinted with permission from ref. [119]. © 2015, The American Physical Society.

yielded a total reaction cross section of 585 mb, consistent with the 506 ± 97 mb value obtained in ref. [118].

On the basis of the elastic-scattering data of ref. [118], calculations on the energy dependence of the optical polarization potential were performed in ref. [120]. The experimental uncertainties did not allow to make a definitive conclusion about the presence (or not) of the breakup threshold anomaly (BTA) in the ^{7}Be + ^{58}Ni system. However, when the respective fusion data (sect. 7.3) could be also included in the analysis, it was concluded that this system actually shows the more normal threshold anomaly (TA) instead of the BTA [121].

7.2 Breakup of ^{7}Be

An unambiguous measurement of non-capture breakup of ^{7}Be into ^{3}He + ^{4}He would require coincidence detection of the respective He residues. In the ^{7}Be + ^{58}Ni experiment mentioned in sect. 7.1.6, ref. [119], no such coincidences were observed within the limits of the respective geometrical efficiency, thus providing an indication of a low bu cross section. Upper limits for the experimental bu angular distribution were obtained and, through respective CDCC calculations consistent with such limits, an estimated $\sigma_{bu} = 10.8$ mb was obtained for this cross section at $E_{lab} = 21.5$ Mev. According to the calculations, bu would make a contribution of 31% (24%) to the ^{3}He (^{4}He) experimental yields corresponding to direct processes, *i.e.*, after subtraction of the evaporation α yield from fusion. The latter yield was obtained by fitting with the statistical code PACE2 the ^{4}He angular distribution measured in the angular range $\theta_{lab} \geq 115°$, where fusion is likely to be the dominant mechanism. Other direct processes considered in ref. [119] were ^{4}He stripping, which would contribute

to $\sim$ 69% of the observed ^{3}He yield, and 1n-pickup (1n-stripping) with a 27% (22%) contribution to the measured ^{4}He yield. A remaining $\sim$ 26% ^{4}He yield, which happened to concentrate in the angular region between 50° and 70°, was ascribed to the ^{3}He stripping process.

In ref. [122] (reviewed in ref. [1]), reactions of ^{7}Be with ^{238}U at $E_{c.m.}$ energies of 54.4, 50.5, 48.4, 42.7, and 38.8 MeV were measured, stressing fusion-fission events. Light charged-particle yields were observed in coincidence with fission events, but this would exclude most breakup events because the fission signature requires a large energy transfer to the target. However, similar to the conclusions mentioned with respect to ^{7}Be + ^{58}Ni in the preceeding paragraph, these yields could be best explained as the products of ^{3}He and ^{4}He cluster transfers.

^{7}Be breakup events also were searched for in the ^{7}Be + ^{12}C experiment of ref. [111] by generating coincidence spectra for ^{3}He, ^{4}He, and $Z = 1$ ions. Very few ^{3,4}He coincidences were observed, but no upper limits for the respective bu cross section were estimated. A strong selectivity was observed in the ^{12}C(^{7}Be, ^{3}He) reaction, populating α cluster states in ^{16}O, and the measured angular distributions for ^{3}He were forward peaking. These two features are indicative of a direct α transfer as the main mechanism contributing to the observed ^{3}He yield, consistent with the conclusions of the ^{7}Be + ^{58}Ni experiment mentioned above [119].

7.3 Fusion of ^{7}Be

Fusion measurements with ^{7}Be projectiles have been reported for the rather light target ^{27}Al [114], the medium-mass target ^{58}Ni [123], and the much heavier target ^{238}U [122]. The ^{27}Al data were obtained by subtracting the measured one-proton-stripping cross sections from the total reaction data deduced from respective quasielastic-scattering measurements [114]. It should thus be correct to associate the reported values to the total fusion (TF) cross section or, at worst, to an upper bound for it. Fusion cross sections of 635 ± 76, 858 ± 94 and 922 ± 92 mb were obtained for $E_{lab} = 17, 19$ and 21 MeV, respectively. A comparison with fusion data for the mirror nucleus ^{7}Li on the same target yielded similar results.

For the ^{58}Ni target, evaporation proton yields were measured and total fusion cross sections were deduced by using calculated proton multiplicities [123]. Measurements performed at energies $E_{c.m.} = 13.9, 15.0, 16.6, 17.4, 17.9,$ and 19.0 MeV gave cross sections of $\sigma_{TF} = 26 \pm 3$, 61 ± 7, 165 ± 32, 246 ± 78, 292 ± 46, and 395 ± 116 mb, respectively. An enhancement with respect to BPM predictions corresponding to a realistic bare potential was observed, even in the region above the barrier.

In the case of the ^{238}U target, fusion-fission was measured [122]. Charged particles were detected with 40 Silicon detectors completely surrounding the target and a fission signature was established through coincidence of products flying in nearly opposite directions. Light charged particles in coincidence with fission also were detected in some events, which discards the possibility of complete fusion (CF) for these events. A complete fusion cross section (σ_{CF}) was thus deduced by subtracting the latter events from the total fission events.

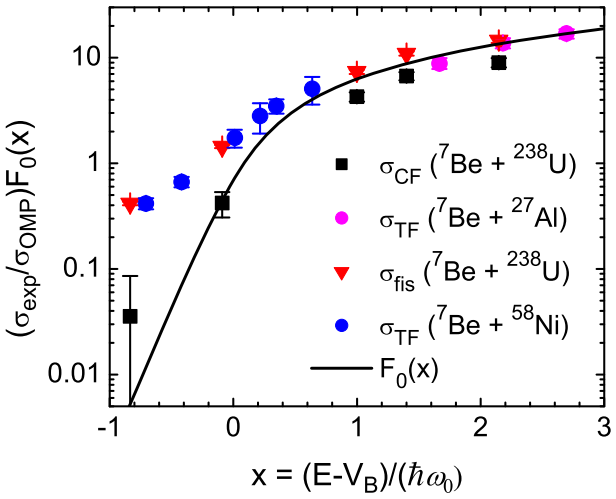

Fig. 22. Reduced total fusion cross sections for ^{7}Be + (^{27}Al, ^{58}Ni, ^{238}U), from data published in refs. [114,123,122], respectively. In the case of the ^{238}U target, respective CF data are also shown. The solid curve is the UFF. Adapted with permission from a figure published in ref. [123]. © 2014, The American Physical Society.

Taking the total fission data for the latter system, both CF and ICF would be included in the cross sections for all three systems, as well as possible ^{3,4}He direct transfer to highly excited states. This kind of transfer would produce fission (evaporation protons) in the case of the U (Ni) target, respectively. The three data sets are plotted together in reduced units in fig. 22, which in addition includes the CF data for ^{238}U, for comparison. A good consistency is seen in this figure between the σ_{TF} data (σ_{fis} for ^{238}U) corresponding to the three systems, which could indicate that the dominant mechanism responsible for the observed sub-barrier enhancement is mainly associated with the ^{7}Be projectile, independent of the target. The enhancement factor is still fairly large at the barrier ($\sim$ 2.5) and there is also evidence of enhancement for energies slightly above the barrier. For $x = 0.35$, for instance, the respective factor is $\sim$ 1.5. This corresponds to 1.1 (1.8) MeV above the barrier for the ^{7}Be + ^{58}Ni (^{7}Be + ^{238}U) system, respectively. It was shown in ref. [123] that inelastic excitations of target and projectile can account for part of the observed enhancement, but an additional mechanism would be needed to properly describe the data, especially for energies close to and below the barrier.

8 Reactions with ^{10}Be

The ^{10}Be nucleus is tightly-bound, with a neutron separation energy $S_n = 6.81$ MeV and a half-life of 1.51×10^{6} years. It can therefore be produced as either a primary or secondary beam. Fusion and elastic-scattering experiments with a ^{10}Be beam have been performed for intrinsic

interest and also for comparison with data for other isotopes such as the proton-rich ^{7}Be and neutron-rich ^{11}Be projectiles. These works are reviewed below.

8.1 Elastic scattering of ^{10}Be

8.1.1 ^{10}Be + ^{12}C

The elastic scattering of a low-energy ^{10}Be beam on a ^{12}C target was reported in ref. [110]. The 26 MeV secondary ^{10}Be beam was produced by the double solenoid RIBRAS facility at the Universidade de São Paulo, Brazil [124]. The ^{9}Be(^{11}B, ^{10}Be) reaction was used to produce a beam with an intensity of about 5×10^{3} pps. The elastic-scattered particles were identified by three ΔE-E silicon detector telescopes. An analysis with an optical-model potential was performed, considering both volume Woods-Saxon (WS) and double-folding São Paulo (SP) type potentials, achieving good agreement with the data.

Coupled-channel calculations have also been performed considering the two bound excited states in ^{10}Be (2^{+}_{1} and 0^{+}_{1}). These two excited states correspond to the most probable quadrupole transitions in ^{10}Be. The vibrational model for two-phonon states was adopted. The reduced transition probabilities $B(E2)(2^{+}_{1} \rightarrow 0^{+}_{gs}) =$ 8.0 W.u. and $B(E2)(0^{+}_{1} \rightarrow 2^{+}_{1}) = 2.5$ W.u. were taken from ref. [125]. These calculations also gave a good description of the angular distribution. It was determined that the coupling to the first excited state (2^{+}_{1}) was the most important one in describing the data. A comparison of the reduced total reaction cross section for the ^{7,9,10}Be + ^{12}C systems, also obtained from the double-folding potential analysis, is shown in fig. 19 (sect. 7.1.2), together with the results for some other light projectiles from the literature. The reduction of the reaction cross section is as given in sect. 2.2.2 above.

As pointed out in ref. [110], this behavior differs from that for weakly-bound projectiles on heavy targets where enhancement of the total reaction cross sections at near-barrier energies was observed. This can be an indication that dynamic effects have only a small influence on the reactions of these projectiles on the light ^{12}C target.

8.1.2 ^{10}Be + ^{64}Zn

The elastic scattering of ^{10}Be on ^{64}Zn was reported in ref. [126]. A full description of the experiment, as well as a more detailed analysis, was reported later in ref. [127]. Beams of ^{10}Be and ^{11}Be, produced by spallation of 1.4 GeV protons on a Ta target at REX-ISOLDE at CERN [128], were post-accelerated in the REX-Linac to 28.4 MeV and 28.7 MeV, respectively. The data on ^{11}Be will be discussed in sect. 9 below.

The motivation to perform elastic-scattering measurements with these projectiles was to investigate the influence of their nuclear structure on this process. The measurement with strongly-bound ^{10}Be serves as a base for comparison with the more exotic ^{11}Be isotope. The

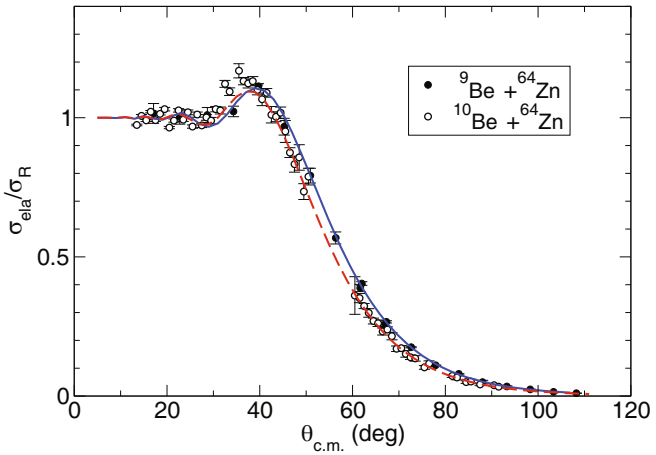

Fig. 23. Elastic-scattering angular distribution for ^{9}Be + ^{64}Zn (filled symbols) and ^{10}Be + ^{64}Zn (open symbols). The curves represent the results of an OM analysis. Figure reprinted with permission from ref. [127]. © 2012, The American Physical Society.

elastic-scattering angular distribution of strongly-bound light projectiles can show a Coulomb rainbow, when there is little or no absorption, or Fraunhofer/Fresnel diffraction when there is absorption.

An angular distribution for ^{10}Be + ^{64}Zn reported in refs. [126,127] was measured at $E_{c.m.} = 24.5$ MeV. It is shown in fig. 23, together with that measured for the weakly-bound ^{9}Be isotope at 29 MeV. The detection setup used in this experiment consisted of an array of 50×50 mm^{2} double sided Si-detector (DSSD) telescopes covering the angular range of 10° to 150°.

An OM analysis was performed with Woods-Saxon–type potentials. Angular distributions for the elastic scattering of both ^{9}Be and ^{10}Be show a Fresnel peak as expected. The most important conclusion from this OM analysis was the observation of a large ambiguity in the depth of the real potential. By continuously varying the radius parameter, equivalent fits could be obtained with different real potential depths, without changing the imaginary potential. Also, all potentials gave equivalent fits for distances larger than about $R = 10$ fm, indicating that the tail for all these potentials is identical. A double-folding potential analysis has also been performed for these systems by Hemalatha [129].

8.1.3 ^{10}Be + ^{194}Pt

A Coulomb excitation study of the 2^{+}_{1} state at 3.368 MeV in ^{10}Be has been performed via an inelastic-scattering measurement on a ^{194}Pt target [130]. The experiment was performed with a 41 MeV secondary ^{10}Be beam, produced at the TRIUMF/ISAC-II radioactive ion beam facility with an intensity of 1×10^{7} ions/s. The beam impinged on a 3.0 mg/cm^{2} ^{194}Pt target at the center of the TIGRESS γ-ray spectrometer [131]. The 41 MeV incident energy is well below the Coulomb barrier for this system. The use of reactions with negligible nuclear contributions is fundamen-

tal in such experiments, to avoid Coulomb-nuclear interference. Gamma rays emitted following the de-excitation of states in both beam and target nuclei were detected by eight segmented, highly efficient, Compton-suppressed TIGRESS clover detectors. The γ rays were used to clean the energy spectrum of the scattered ^{10}Be ions.

The quadrupole moment values and γ-ray yields from the de-excitation of the 3.368 MeV state were used to obtain the diagonal matrix element of the electric-quadrupole tensor in ^{10}Be, which was compared with predictions from several calculations. The experiment showed the feasibility of Coulomb excitation studies of high-lying 2_1^+ states in light nuclei, which is important to improve the understanding of the contributions of 2-nucleon and 3-nucleon potentials to the nuclear spin-orbit interaction, and especially how these contributions affect electric-quadrupole matrix elements.

8.2 Fusion of ^{10}Be

8.2.1 ^{10}Be + ^{209}Bi

Fusion reactions induced by ^{10,11}Be at energies close to the barrier (E_{lab} = 40 to 50 MeV) have been measured at RIKEN, Japan. This experiment was reviewed in [2]. The data were obtained in two different runs and were reported in two papers [132,133]. In the second paper, a new analysis of the first run was presented. The investigation of the fusion dynamics for these nuclei is related to the influence of their cluster structure on the complete and incomplete fusion process.

The data analysis for the ^{10}Be+^{209}Bi system has been revised by Hinde and Dasgupta [134]. Their motivation to carry out a new analysis was the fact that the results and conclusions from the previous two papers in refs. [132, 133] were different. The cause of difference was the detection efficiency within the time windows considered in these papers, which used the time of flight of the beams to determine the incident energy on an event by event basis. Depending on the time windows considered, different contributions were obtained from ^{215,216}Fr following 4n and 3n evaporation in the case of ^{10}Be projectile. Using the empirical systematics from the cross section for the ^{9}Be + ^{209}Bi system [132,135,136], the efficiency could be accounted for. The relative yields for the xn channels from complete fusion, the correct absolute normalization, and the fission contribution to the complete fusion cross section could then be deduced. The results of these corrections, and the newly-obtained cross sections as a function of the incident energy can be seen in fig. 24. The discussion and comparison of the results for the ^{9,10,11}Be + ^{209}Bi systems are presented in sect. 9.3 below.

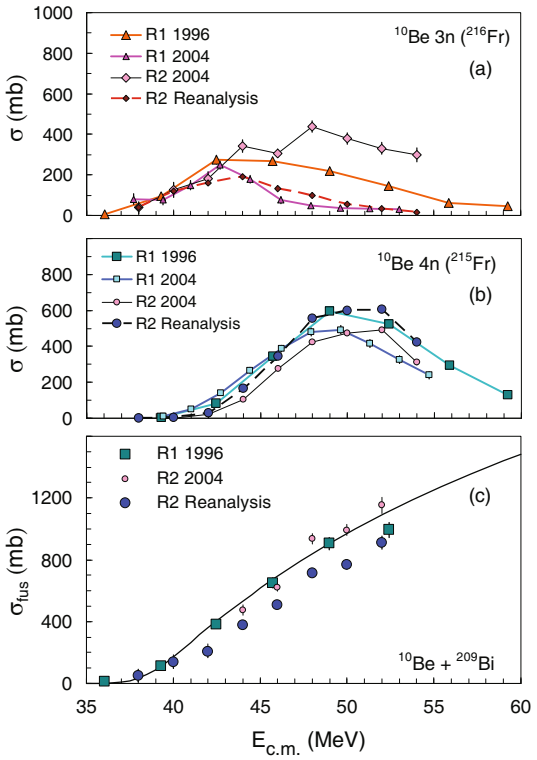

Fig. 24. Individual 3n- and 4n-evaporation channels and total fusion cross sections for the ^{10}Be + ^{209}Bi system. The several analyses are indicated. R1 1996 refers to the data and analysis from ref. [132], R1 2004 are the data from ref. [132] with analysis from ref. [133], R2 2004 are the data and analysis from ref. [133] and R2 Reanalysis are the data from ref. [132] and analysis from ref. [134]. Figure reprinted with permission from ref. [134]. © 2010, The American Physical Society.

9 Reactions with ^{11}Be

The ^{11}Be nucleus has a $J^\pi = 1/2^+$ ground state with a neutron binding energy of S_n = 0.501 MeV. It is one of the rare cases of a halo nucleus with a bound excited state. The low binding energy combined with the primarily S-wave relative orbital of the loosely bound neutron produce a one-neutron halo structure for this nucleus, with a compact ^{10}Be(0^+) core (not inert). Actually, ^{11}Be is the only presently-known halo nucleus with a strongly deformed core [137]. It has one of the largest known reduced dipole transition probabilities between the first excited state at E_x = 0.32 MeV and the ground state ($B(E1) = 0.116(12)\ e^2\,\mathrm{fm}^2$ [138]). This observation is corroborated by the recent high precision measurement of the electromagnetic dipole strengths performed at the TRIUMF Isotope Separator and Accelerator (ISAC II) [139]. The unusual features of this halo nucleus strongly affect the interaction with both light and heavy targets at low bombarding energies. Some experiments have recently been performed with a ^{11}Be beam to further investigate the effect of the distinctive features of this nucleus, such as the extended neutron density distribution, on fusion and elastic scattering.

9.1 Elastic scattering of ^{11}Be

The elastic-scattering angular distributions for neutron-halo nuclei such as ^{11}Be from heavy targets at near-barrier

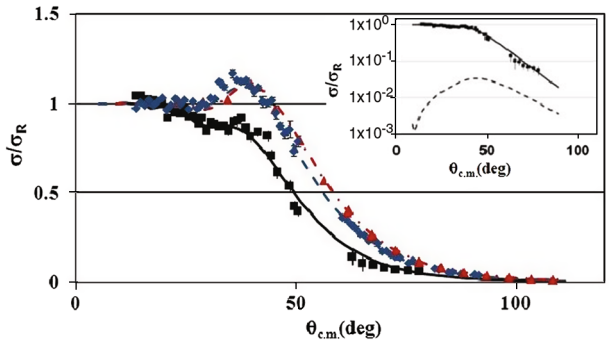

Fig. 25. Elastic-scattering angular distributions for ^{9}Be (triangles), ^{10}Be (diamonds), and ^{11}Be (squares) + ^{64}Zn. The data for ^{11}Be is practically elastic (not quasielastic) since the contribution of the inelastic channel ($E_x = 0.320\,\mathrm{MeV}$), shown in the inset, is very small. Figure reprinted with permission from ref. [126]. © 2010, The American Physical Society.

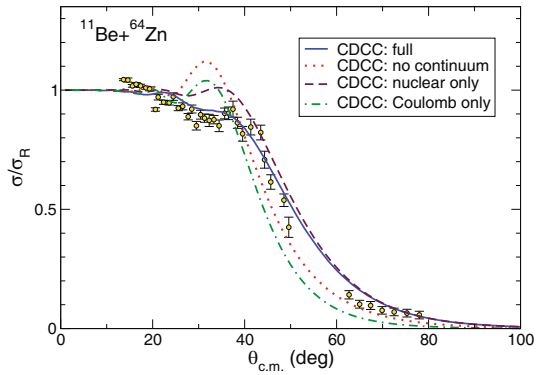

Fig. 26. Elastic-scattering angular distribution for the ^{11}Be + ^{64}Zn system at $E_{c.m.} = 24.5\,\mathrm{MeV}$. The curves correspond to CDCC calculations as indicated. Figure reprinted with permission from ref. [127]. © 2012, The American Physical Society.

energies are strongly affected by dipole polarizability. The combination of the nuclear interaction and the strong electric field make the charged core and the halo neutrons move in opposite directions, which in turn produces strong coupling to dipole modes of the system at relatively low excitation energy. These effects were investigated in the elastic scattering of ^{11}Be.

9.1.1 ^{11}Be + ^{64}Zn

The elastic scattering of a low-energy ^{11}Be beam on a ^{64}Zn target was measured in the same experiment as for the ^{10}Be beam discussed in sect. 8.1.2 above. The angular distribution measured at $E_{c.m.} = 24.5\,\mathrm{MeV}$ was first reported in ref. [126] and is shown in fig. 25.

Because of the small excitation energy of the first excited state ($E_x = 0.320\,\mathrm{MeV}$), the elastic cross section data may contain some contribution from inelastic scattering. As can be seen in the figure, the ^{11}Be scattering shows a very different pattern as compared to those for the ^{9}Be and ^{10}Be projectiles. The cross sections at forward angles are strongly reduced in a similar way to what is observed in collisions involving very deformed nuclei, where the damping is due to strong Coulomb excitation of the target [140]. Similar damping of the cross sections at forward angles observed in ^{11}Li and ^{6}He elastic-scattering angular distributions was attributed to a large Coulomb dipole excitation due to the presence of the strong continuum low-lying $E1$ strength, which is associated with the halo structure of these nuclei. The data shown in fig. 25 were analyzed in terms of the optical model (OM) using Woods-Saxon–type potentials. To describe the unusual pattern of the ^{11}Be angular distribution due to the presence of long-range couplings, a phenomenological surface potential (DPP) having the shape of a WS derivative was added to the imaginary volume potential. The best χ^2 fit was obtained with a large diffuseness, $a_{si} = 3.5\,\mathrm{fm}$ for this DPP. The authors concluded that the suppression of the cross section at forward angles originated from large-partial-wave absorption due to the diffuse halo structure of ^{11}Be. A more detailed analysis of this angular distribution in terms of continuum-discretized coupled-channel (CDCC) calculations was later reported in refs. [127,141], where a full description of the experiment was also given. A comparison of the CDCC results with the experimental data is shown in fig. 26. It's important to mention that the contribution of ^{10}Be core excitation was not taken into account in these calculations.

The full CDCC calculation, represented by the solid line in the figure, reproduces the data very well. The importance of the couplings to both nuclear and Coulomb breakup is also clear. As pointed out by Keeley in ref. [142], the largest effect in the damping of the Fresnel peak is due to nuclear breakup coupling. This could be interpreted as an unexpected result and should be further elucidated by more detailed model calculations where ^{10}Be would no longer be treated as an inert core.

A detailed study of the convergence in CDCC calculations for light exotic nuclei, where the importance of spins, binding energy, and number of partial waves were analyzed, was performed by Druet and Descouvemont [143]. They used the ^{11}Be + ^{64}Zn elastic-scattering data to show that an accuracy of 10% can be achieved in the CDCC calculations, but for higher accuracy convergence issues must be carefully taken into account.

Another analysis of this set of data was performed in terms of the OM with a bare potential plus a long-range dipole polarization potential (DPP) by Hemalatha [129]. The bare potential was a double-folding potential taking into account a parametrized extended density for ^{11}Be folded with the M3Y effective nucleon-nucleon interaction. The DPP was determined by using the dipole strength distribution from the cluster model and also from experimental data. The results for the calculated differential cross sections show a suppression in the Coulomb-nuclear interference region and reproduce the data quite well.

A more recent analysis of this set of data was performed by So *et al.* and reported in ref. [144]. Their OM analysis consisted of a short-range potential with a Woods-Saxon shape and parameters from the ^{10}Be + ^{64}Zn analysis, plus a long-range dynamic polarization (LRDP)

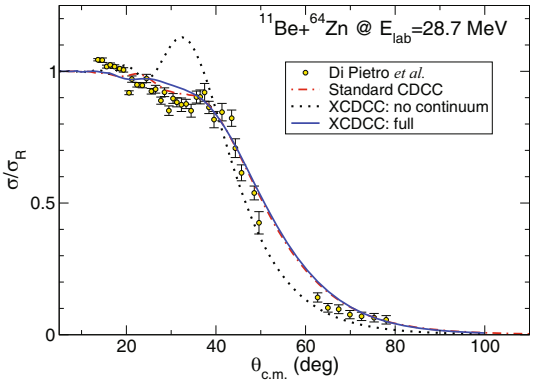

Fig. 27. Elastic-scattering angular distribution for the ^{11}Be + ^{64}Zn system at $E_{c.m.} = 24.5$ MeV. The curves correspond to CDCC calculations as indicated. Figure reprinted with permission from ref. [145]. © 2014, The American Physical Society.

potential consisting of a Coulomb dipole excitation (CDE) potential and a long-range nuclear (LRN) potential. Their conclusion is that both the CDE and LRN potentials are essential to describe the experimental angular distribution. The real parts of both potentials were responsible for the strong absorption by lowering the barrier, and the imaginary parts removed flux from the elastic channel.

The CDCC calculations described above ignored the possible admixtures of different core states in the wave functions of the ^{11}Be, as well as ^{10}Be core excitation. These admixtures are known to be important, particularly in the case of the well deformed ^{10}Be core. An extended CDCC calculation with core excitation has been performed by de Diego *et al.* and reported in ref. [145]. The authors improved the XCDCC calculation developed in ref. [146] by using the so-called pseudo-state method, in which the projectile states are approximated by the eigenstates of the Hamiltonian in a truncated basis of square-integrable functions. The results of this calculation for ^{11}Be + ^{64}Zn can be seen in fig. 27. To account for core excitation, the potential was deformed with the same deformation length used in the structure model, *i.e.*, $\delta 2 = 1.664$ fm. As can be seen in the figure, the XCDCC calculation is similar to the CDCC result but slightly overpredicts the data near 30°.

9.1.2 ^{11}Be + ^{120}Sn

Data on angular distribution for elastic scattering of ^{11}Be + ^{120}Sn were obtained at the REX-ISOLDE facility [147]. The experimental setup was similar to that used to measure elastic scattering and breakup for ^{11}Be + ^{64}Zn [126,127]. To compensate for the low beam intensity ($< 10^5$ pps), a thick (3.5 mg/cm^2) ^{120}Sn target was used. This limited the energy resolution of their detection system to 350 keV. It was therefore not possible to resolve the first excited state in ^{11}Be and the data are actually quasielastic. For angles between 15° and 38°, however, it was possible to identify the ^{10}Be fragments produced by the breakup of ^{11}Be into ^{10}Be+n. The measured angular distribution of quasielastic scattering was analyzed in terms of coupled channel (CC) calculations to study the relevant aspects of the dynamics of the reaction process. The qualitative CC calculation included several excited states in ^{11}Be up to 3.41 MeV, taking a vibrational model for the projectile and treating the target as inert. As a result, the couplings were found to be important but insufficient to completely describe the angular distribution.

A CDCC analysis of these data has also been performed [148]. Deformation of the ^{10}Be core was, however, not taken into account. It was found that Coulomb-nuclear interference is very important even at more backward angles where experimental data are unavailable. The effects of neutron transfer were also ignored. The authors suggested that it would be useful to obtain data beyond 40° to help disentangle the contributions of breakup and neutron transfer.

9.1.3 ^{11}Be + ^{197}Au

Preliminary data on inelastic scattering of ^{11}Be + ^{197}Au at 31.9 MeV from the TRIUMF/ISAC-II facility was reported in ref. [149]. The ^{11}Be beam had an intensity of 10^5 pps. The experimental inelastic-scattering probability was compared with semiclassical and coupled-channels calculations. The CDCC calculation overestimated the inelastic-scattering cross section. This can be explained by the fact that pure single-particle configurations of the valence neutron relative to an inert ^{10}Be(0^+) core was assumed, where the ground and first excited states correspond to pure $2s_{1/2}$ and $1p_{1/2}$ configurations, respectively. These states could in reality contain significant admixtures of excited states of the ^{10}Be core.

9.1.4 ^{11}Be + ^{209}Bi

Data on elastic scattering of ^{11}Be on a ^{209}Bi target were reported in ref. [150]. The experiment was carried out at the RIKEN laboratory in Japan. The ^{11}Be beam was produced in-flight by the fragmentation of ^{13}C ions on a Be target, and selected using the RIKEN Projectile-Fragment Separator (RIPS) [151]. The energy of the ^{11}Be beam (48 MeV/u) was strongly degraded to a final energy in the range of $E_{lab} = 40$–50 MeV. Angular distributions of the quasielastic process were obtained at five beam energies between 40 and 48 MeV. Since the experimental energy resolution did not allow the separation of inelastic scattering to the first excited state of ^{11}Be (0.320 MeV), the differential cross sections are actually quasielastic. The angular distributions were analyzed in terms of the OM with Woods-Saxon potentials. The inelastic contribution (up to 30% of the total yield) was estimated with DWBA and CC calculations. The total reaction cross section for each energy was obtained and scaled by R^2, where R is the sum of the projectile and target radii. The energy was scaled by the Coulomb barrier ($E_{c.m.}/V_C$) and the scaled values were compared with those for ^{9}Be + ^{209}Bi. At lower energies the reaction cross sections were larger for ^{11}Be, suggesting that direct processes due to the halo structure are more important at energies closer to the barrier.

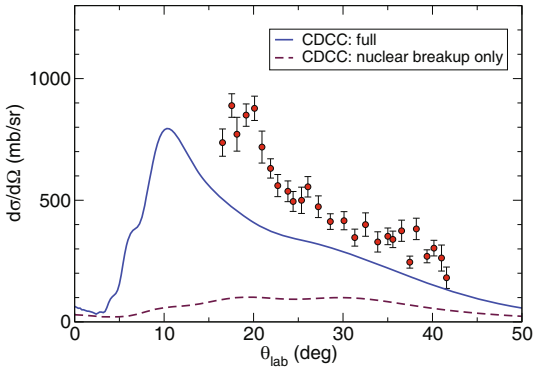

Fig. 28. Angular distribution for breakup and/or transfer in the ^{11}Be + ^{64}Zn system at $E_{c.m.}$ 24.5 MeV. The curves correspond to CDCC calculations as indicated. Figure reprinted with permission from ref. [127]. © 2012, The American Physical Society.

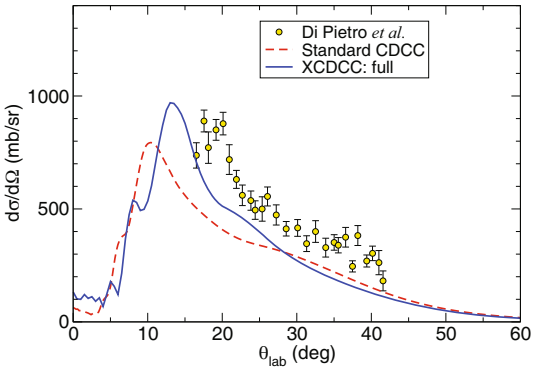

Fig. 29. Angular distribution for breakup and/or transfer in the ^{11}Be + ^{64}Zn system at $E_{c.m.}$ 24.5 MeV. The curves correspond to standard CDCC (dashed line) and XCDCC (solid line) calculations as indicated. Figure reprinted with permission from ref. [145]. © 2014, The American Physical Society.

9.2 Breakup of ^{11}Be

9.2.1 Breakup in the ^{11}Be + ^{64}Zn system

Large numbers of ^{10}Be events from breakup and/or transfer were identified in the elastic scattering of ^{11}Be + ^{64}Zn at $E_{c.m.} = 24.5$ MeV [126].

An angular distribution for these events was obtained, and a total integrated cross section from 0° to 60° of 1100 ± 150 mb was measured. A CDCC calculation was compared with the experimental angular distribution in ref. [127]. The results of this comparison are illustrated in fig. 28, where the solid line represents the full Coulomb + nuclear breakup and the dashed line is the result of nuclear breakup only. This calculation underestimated the data by 30%. This is perhaps to be expected since it corresponds to *elastic breakup* only. The contribution from the transfer of the undetected valence neutron to the target, as well as the excitation of the target and/or the ^{10}Be core, were not taken into account.

The previously mentioned XCDCC calculations, where admixtures of different core states into the wave functions of ^{11}Be as well as ^{10}Be core excitation were included, is reported in ref. [145]. This method was also used to compute the breakup cross section for the ^{11}Be + ^{64}Zn system. The calculation is considered to be only an approximation due to the fact that the XCDCC framework would require an appropriate kinematic transformation that is not yet available. Instead, the ^{10}Be scattering angle was approximated by the ^{11}Be scattering angle. The results of this calculation are shown in fig. 29. As can be seen in the figure, the XCDCC calculation is larger than the CDCC result and improves the agreement with the data. The remaining discrepancy was attributed by the authors to limitations of the ^{11}Be model used in the XCDCC calculations, but also to the contribution of non-elastic breakup events in the data.

9.2.2 Breakup in the ^{11}Be + ^{120}Sn system

Data on the breakup angular distribution for the ^{11}Be + ^{120}Sn system were obtained during the elastic-scattering experiment reported in ref. [147]. However, the results for the experimental breakup cross sections and a CDCC analysis were reported in ref. [148]. The contributions of Coulomb (C) and nuclear (N) breakup were investigated. The calculated breakup cross section with pure nuclear interactions was found to be negligible in comparison with the cross section calculated including Coulomb effects. Coulomb-nuclear interference played an important role in explaining the experimental data, although the calculation could not reproduce the absolute values.

9.2.3 Breakup in the ^{11}Be + ^{197}Au system

Preliminary data on inclusive breakup and/or transfer was obtained in the 31.9 MeV inelastic-scattering experiment discussed in sect. 9.1.3 above. An angular distribution measured in the angular range from 13° to 46° was reported in ref. [149]. A large yield of ^{10}Be was observed in this angular range, and the breakup probability was obtained. The data were compared with semiclassical and coupled-channels calculations. The semiclassical calculations, based on the first-order Coulomb theory of Alder and Winther [98] (which gives a breakup probability for a pure dipole excitation) underestimated the data. On the other hand, the CDCC calculation reproduced the experimental breakup cross sections quite well. As already mentioned, the CDCC calculation did not reproduce the inelastic-scattering data, indicating the need for a more sophisticated model to reproduce all the observables. The authors claimed that this was a preliminary analysis, and an extended CDCC calculation incorporating core-excitation effects in the structure of ^{11}Be, as well as in the core-target interaction, was in progress.

9.3 Fusion of ^{11}Be

As already mentioned in sect. 8.2 above, fusion induced by ^{10,11}Be at energies close to the barrier has been investigated at RIKEN, and these data were reviewed in

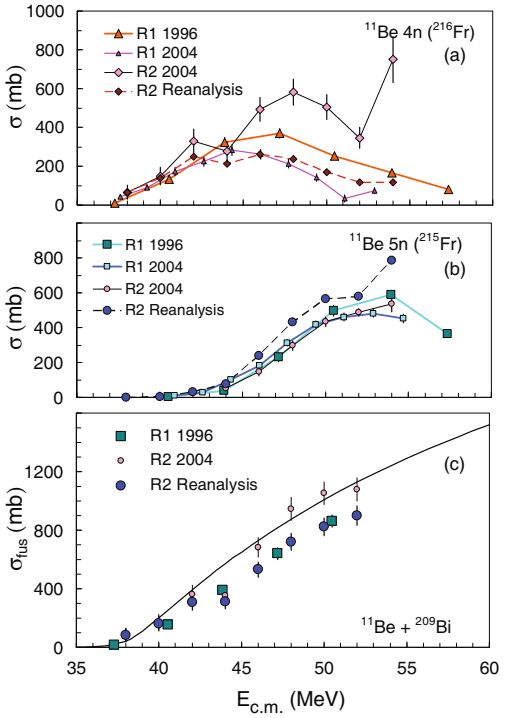

Fig. 30. Individual 4n- and 5n-channel evaporation and total fusion cross sections for the ^{11}Be + ^{209}Bi system. R1 1996 are the data and analysis from ref. [132], R1 2004 are the data from ref. [132] with analysis from ref. [133], R2 2004 are the data and analysis from ref. [133] and R2 Reanalysis are the data from ref. [132] but analysis from ref. [134]. Figure reprinted with permission from ref. [134]. © 2010, The American Physical Society.

ref. [2]. An activation method was used, detecting α particles emitted by the residual nucleus after 4n and 5n evaporation to infer information concerning complete and incomplete fusion. The investigation of the fusion dynamics for these nuclei is related to the influence of their cluster structure on the complete and incomplete fusion processes. In the case of ^{11}Be, a halo nucleus with a large radius, a reduced Coulomb barrier and a larger fusion cross section might be expected. On the other hand, the weak binding energy should increase the breakup probability and consequently may reduce the fusion yield. The data were obtained in two different runs and were reported in two papers [132,133]. In the second paper, a new analysis of the first run was presented. The data obtained with ^{11}Be projectile were also revised by Hinde and Dasgupta [134], who corrected for the time windows considered in the analysis of the 4n and 5n evaporation using the empirical systematics from the cross section for the ^{9}Be + ^{209}Bi system [132,135,136]. Using this set of data, they could correct for the time-window efficiency, calculate the relative yields for xn channels in complete fusion, correct the absolute normalization, and estimate the fission contribution. The results of these corrections, and the newly-obtained cross sections for the ^{11}Be + ^{209}Bi system, can be seen in fig. 30.

The final, corrected complete (CF) and total (TF) fusion cross sections for the ^{10,11}Be + ^{209}Bi systems were compared with those for the ^{9}Be + ^{209}Bi in ref. [134]. The total fusion cross section included the contribution of incomplete fusion. From the ratio of CF to TF, the fraction of incomplete fusion (ICF) was estimated, with surprising results. The fraction of ICF was 32% for ^{9}Be, 15% for ^{11}Be and 25% for ^{10}Be, although it was claimed that these values could be just a lower limit, depending on the identification and separation of Fr and At α decays. It would be worthwhile to repeat this measurement to obtain a better understanding of the role of the neutron-halo and α-cluster structure of ^{9,10,11}Be in the fusion process.

10 Reactions with ^{8}B

Several pieces of evidence support the presence of proton-halo structure in the ground state of the proton dripline nucleus ^{8}B, and it is now generally agreed that this is the case. The low proton separation energy associated (0.138 MeV) should in principle make the respective breakup process an important reaction channel in reactions with ^{8}B. Data with this projectile are still scarce because of the extreme difficulties to get reasonably intense beams, but some low-energy measurements have been performed in the last few years. Including both, experimental and theoretical works involving reactions with ^{8}B, over 40 articles have appeared during this period.

10.1 Elastic scattering of ^{8}B

Within the energy range of interest in the present review, elastic scattering of ^{8}B has been measured on targets of ^{12}C and ^{58}Ni. Higher energy data for ^{12}C and ^{208}Pb targets also will be mentioned because they are considered as providing interesting complementary information.

10.1.1 ^{8}B + ^{12}C

An elastic-scattering angular distribution for ^{8}B + ^{12}C has been measured in ref. [109] at an incident energy of 25.8 MeV, which is nearly three times the corresponding Coulomb barrier (V_B = 5.14 MeV). The data could be well described by an optical-model calculation using the São Paulo potential (SPP) with conventional normalization, indicating a weak effect of the breakup process on the elastic scattering. This was confirmed by performing CDCC calculations and comparing the full-coupling with the no-coupling results, as shown in fig. 31. Further CDCC studies of this system for near-barrier energies [152] indicated a negligible effect of breakup on the elastic channel at these energies as well. Comparing with previous calculations for a ^{58}Ni target (see sect. 10.1.2), it was concluded that such effect decreases with the charge of the target.

Analyzing data from an experiment performed at the higher energy E_{lab} = 95 MeV (ref. [112], reviewed in [1]), it was found in ref. [113] that core excitation has a significant effect on the ^{8}B + ^{12}C elastic-scattering channel. In

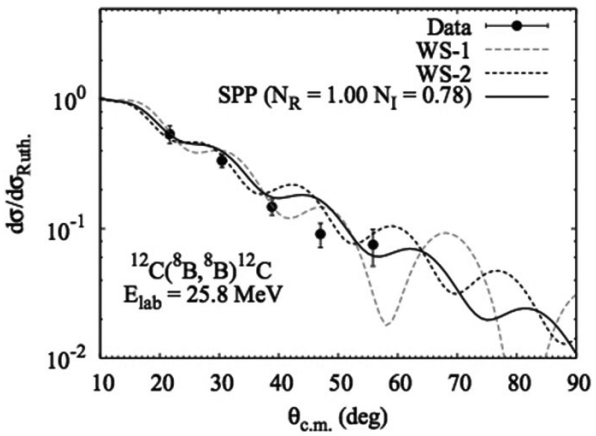

Fig. 31. Elastic scattering of ^{8}B on ^{12}C at 25.8 MeV. Figure reprinted with permission from ref. [109]. © 2011, The American Physical Society.

the latter reference, the ^{7}Be core was assumed to have a ^{4}He+^{3}He cluster structure and, in addition to the ground state, its three lowest excited states were included in a coupled-channel calculation. The valence proton in ^{8}B, on the other hand, was treated in an adiabatic approximation and, similar to the results of ref. [152], it was shown to have a negligible contribution. However, excitation of the $(7/2)^-$ resonant state of ^{7}Be was found to decrease significantly the elastic-scattering angular distribution for $\theta_{lab} \geq 13°$, thus bringing the predictions into agreement with the respective experimental results (see fig. 20 for the respective effect on ^{7}Be scattering).

It was also shown in ref. [152] that the continuum-continuum couplings play an important role on the predicted breakup cross section, a well-known effect in the case of the ^{58}Ni target [153–155].

10.1.2 ^{8}B + ^{58}Ni

The available elastic-scattering data on this system [118] are reviewed in ref. [1]. It was emphasized that, under a reasonable data reduction, the total reaction cross sections deduced for this system are consistent with those for systems having ^{6}He as projectile. This interesting result was further confirmed in ref. [156], where data for additional systems were also reduced and compared. A figure showing this will be presented later (fig. 41 in sect. 17.1.2). On the theoretical side, the data were analyzed in ref. [154], where the ^{8}B nucleus was described as an inert ^{7}Be core plus one proton and the CDCC method was used to investigate the effects of breakup couplings on the elastic-scattering cross sections. The calculations were in excellent agreement with the experimental data for all five energies measured. Inelastic excitations of the target also were considered and shown to have no important influence. Compared with the no-coupling calculation, the overal effect of bu couplings on the elastic-scattering angular distributions was only modest, but a striking effect of continuum-continuum couplings was noticed.

A comparison with the behavior of ^{6}Li projectiles, which show smaller bu cross sections but quite important bu coupling effects on the respective elastic scattering, has lead Keeley *et al.* [142,157] to point out that reactions with ^{8}B offer extreme examples where large bu cross sections not necessarily imply a large bu coupling effect. This point has been further discussed in refs. [1,158–160].

In ref. [120], a detailed study of the energy dependence of the optical potential for this system was made. The respective behaviour was found to be more compatible with the Breakup Threshold Anomaly (BTA) than with the more normal Threshold Anomaly. A similar study but including also the respective fusion data (see sect. 10.3) confirmed the BTA behaviour for this system [161].

10.1.3 ^{8}B + ^{208}Pb

An elastic-scattering angular distribution for ^{8}B + ^{208}Pb at 170.3 MeV was measured in ref. [158]. Even though this energy (nearly three times the Coulomb barrier) is considerably higher than the limit set for the present review, it is mentioned here because the conclusions reached are quite similar as those in the previous lower-enery ^{8}B studies for ^{12}C and ^{58}Ni targets. Arguments were given showing that inelastic scattering makes a negligible contribution to the data and corresponding CDCC calculations suggested a small effect of bu coupling channels on the elastic scattering for this heavier system as well.

10.2 Breakup of ^{8}B

The process of ^{8}B breakup in the field of heavy nuclei is of special interest as it can provide information about the ^{7}Be radiative proton capture at low energies, a reaction that plays an important role to understand the solar neutrino emission. Within the energy range covered in the present work, ^{8}B breakup has been measured only with a ^{58}Ni target.

In the first measurement, performed in 2000 [38], a complete angular distribution of the ^{7}Be bu-fragments was measured at 25.8 MeV (this has been reviewed in ref. [1]). Later, single angle measurements at $\theta = 45°$ were reported in ref. [162] for the three energies 25.0, 26.9, and 28.4 MeV. These measurements yielded results consistent with those at 25.8 MeV and showed a slight growth of the bu cross section with energy. CDCC calculations were performed in the same reference, which gave a good description of both, the ^{7}Be angular distribution at 25.8 MeV and the single angle bu excitation function. These calculations were later extended to lower energies in ref. [163], where the elastic-scattering data for (^{8}B, ^{7}Be) + ^{58}Ni reported in ref. [118] were fitted to determine energy-independent OM potentials and, in addition, DWBA calculations were used to estimate the influence of proton transfer to low-lying states in ^{59}Cu. As a final product, the astrophysical $S_{17}(0)$ factor [64] was found to be 20.8 ± 1.1 eV b.

In refs. [155,164,165] the CDCC formalism was used to study the effect of couplings among continuum breakup

states on the elastic-scattering and breakup cross sections for the ^{8}B+^{58}Ni system. By calculating the respective polarization potential, the authors predicted that the elastic scattering is enhanced by the couplings while non-capture breakup and fusion processes should be hindered. The later prediction, however, was not confirmed by the fusion measurements that will be described below (sect. 10.3).

The fact that reaction cross sections for different systems can in principle be scaled to each other if the respective charges and masses are not too different, has been used to provide experimental evidence that, in interactions with halo nuclei, the respective cores and haloes decouple from each other. In the case of the ^{8}B+^{58}Ni system, for instance, the interactions of the core (σ_{core}) are scaled from corresponding measurements for ^{7}Be + ^{58}Ni, while the interactions of the halo (σ_{halo}) are accounted for by the bu cross sections for the former system. The fact that for all measured energies the sum $\sigma_{core}+\sigma_{halo}$ coincides with the experimental values obtained for the respective total reaction cross sections verifies the decoupling phenomenon for this proton-halo system [118,166]. Neutron-halo nuclei do also show this phenomenon, as shown in refs. [166, 167] from corresponding data for the ^{6}He + (^{209}Bi, ^{64}Zn) systems.

10.3 Fusion of ^{8}B

The methods that have been used to obtain fusion cross sections (σ_{fus}) for ^{8}B consist of measuring a single type of charged evaporated particles and using the results of statistical-model calculations to deduce the respective values of σ_{fus}.

Data were first obtained for the ^{8}B+^{58}Ni system [168], for which σ_{fus} values were reported at ten energies lying in the near- and sub-barrier region. Later, similar data were published for ^{8}B + ^{28}Si [169] at four energies above the respective Coulomb barrier. In ref. [168], evaporation protons were measured while in ref. [169], evaporation alphas rather than protons were measured.

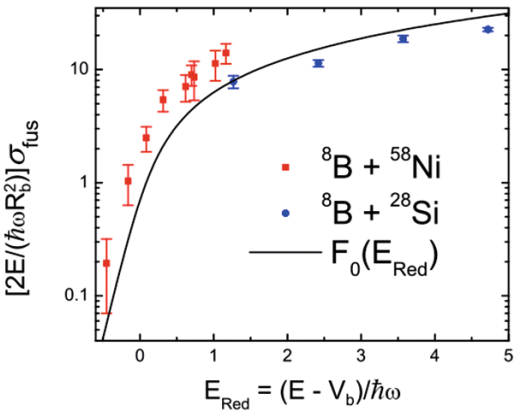

Fig. 32. Reduced fusion data for ^{8}B on ^{58}Ni [168] and ^{28}Si [170]. The barrier parameters are $V_B = 11.3$ MeV, $R_B = 8.2$ fm, $\hbar\omega = 3.38$ MeV for ^{28}Si and $V_B = 20.8$ MeV, $R_B = 8.9$ fm, $\hbar\omega = 4.09$ MeV for ^{58}Ni.

The two data sets, plotted in reduced units, are compared to each other in fig. 32. The data for the ^{8}B + ^{58}Ni system show a big fusion enhancement at all energies, even above the Coulomb barrier. This contrasts with what has been observed for neutron-halo systems, whose total fusion cross sections seem to be suppressed for energies above the barrier. On the other hand, the ^{8}B + ^{28}Si system presents a fusion suppression above the barrier, which would indicate a similar behavior with respect to neutron-halo systems, but an apparent inconsistency with the trend observed for the heavier proton-halo system.

It has been suggested [171] that protons coming from breakup (bu) of ^{8}B into ^{7}Be + p may have an important contribution to the data of ref. [168], which could possibly explain the above results. However, it can be shown [172] that this contribution is small, so that the corrected fusion cross sections remain practically unchanged in the region near and above the barrier. This confirms the presence of a fusion enhancement at energies above but not much higher than the barrier for the ^{8}B + ^{58}Ni system. If one considers possible model dependences in the mapping $\sigma_x \rightarrow \sigma_{fus}$, where x stands for either protons [168] or α particles [169], the two data sets are actually consistent with each other [172].

A novel method of data reduction for the purpose of comparing fusion cross sections for different systems was proposed in ref. [173]. Adducing a key role for phase space availability in the compound system, an energy scaling $E_r = (E_{c.m.} + Q)/(V_B + Q)$ is introduced, which depends on the Q value for compound nucleus formation and on the Coulomb barrier height. By applying this scaling to several systems in a $\sigma_{fus}/(A_p^{1/3} + A_t^{1/3})^2$ *vs.* E_r plot, a similar behavior was found for (^{3}He, ^{16}O) + ^{58}Ni and ^{7}Li + ^{59}Co, with only a slight enhancement around the barrier for the case of ^{8}B + ^{58}Ni.

In ref. [174], a simple one-dimensional model was used to analyze the difference between fusion and total reaction cross sections measured for ^{8}B + ^{58}Ni and for other weakly-bound systems, including systems with the neutron-halo projectile ^{6}He. In this model, all partial waves up to a maximum angular momentum L_f were assumed to fuse, while higher values of L correspond to direct reactions. A simple linear energy dependence was found for L_f in the case of all halo systems analyzed (^{8}B+^{58}Ni, ^{6}He+[^{209}Bi, ^{64}Zn]), as well as for some weakly bound systems (^{6,7}Li + ^{59}Co). These results are consistent with a semiclassical interpretation where the critical distance of approach for fusion to occur grows with decreasing energy.

Within a phenomenological optical-model approach, where both the fusion and the elastic-scattering data were fitted simultaneously, dynamic polarization potentials were derived which describe well the fusion enhancement for the ^{8}B+^{58}Ni system [175]. When these polarization potentials were added to the static Coulomb barrier, the barrier parameters were pushed to larger distances and lower heights than expected for non-halo systems.

In ref. [176], CDCC calculations were carried out including breakup, fusion, and elastic scattering of ^{8}B on

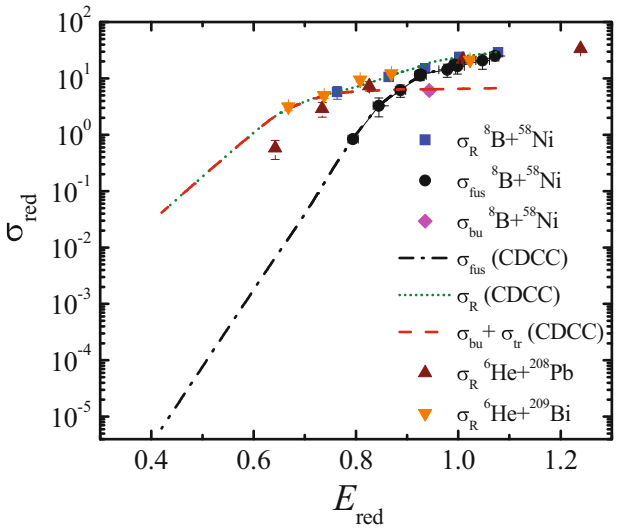

Fig. 33. Reduced fusion data for $^{8}\mathrm{B} + {}^{58}\mathrm{Ni}$ [38,118,168] and respective predictions from ref. [176]. For comparison, total reaction data for $^{6}\mathrm{He} + {}^{208}\mathrm{Pb}$ [17] and $^{6}\mathrm{He} + {}^{209}\mathrm{Bi}$ [177] are also included. Figure adapted with permission from ref. [176].

^{58}Ni. Inelastic excitations in the ^{7}Be-proton system from the ground state to excited states with orbital angular momenta $L = 0$–5 and energies up to 8 MeV in the continuum were considered. Direct proton transfer (tr) was calculated in the coupled-reaction-channels (CRC) approach and fusion was estimated by assuming $\sigma_{fus} = \sigma_R - \sigma_{bu+tr}$. The results are presented in reduced form in fig. 33, where a comparison with total reaction data for $^{6}\mathrm{He} + {}^{208}\mathrm{Pb}$ [17] and $^{6}\mathrm{He} + {}^{209}\mathrm{Bi}$ [177] also is made. The fusion, total reaction, and bu data for $^{8}\mathrm{B} + {}^{58}\mathrm{Ni}$ are from refs. [168,118, 38], respectively.

The calculations reproduce well the experimental fusion, breakup, and total reaction cross sections and predict the respective behavior at low incident energies. The predicted cross section for proton stripping accounts for $\sim 5\%$ of the total ^{7}Be emission cross section at $E_{c.m.} = 22.5$ MeV and rapidly decreases for energies below the Coulomb barrier. In this region, breakup is a predominant process and actually saturates the total reaction cross section at the lowest energy measured (20.7 MeV), showing a flat behavior down to this energy. Fusion becomes more important above the Coulomb barrier.

Coupled-channel calculations including inelastic excitations of the target were performed in ref. [171] for the $^{8}\mathrm{B} + {}^{58}\mathrm{Ni}$ system. To describe fusion, an ingoing wave boundary condition was assumed by using an imaginary Woods-Saxon potential internal to the Coulomb barrier (with depth $W_0 = 50$ MeV, radius $r_W = 1.06$ fm, and diffuseness $a_W = 0.2$ fm). The first 2^+ one-phonon state and the triplet of two-phonon states (2^+, 4^+, 0^+) in ^{58}Ni were included. As a conclusion, coupling to inelastic excitations of the target can not account for the observed fusion enhancement.

Semiclassical arguments indicate that Coulomb polarization might play an important role to produce the enhancement [178]. A time-dependent quantum mechanical

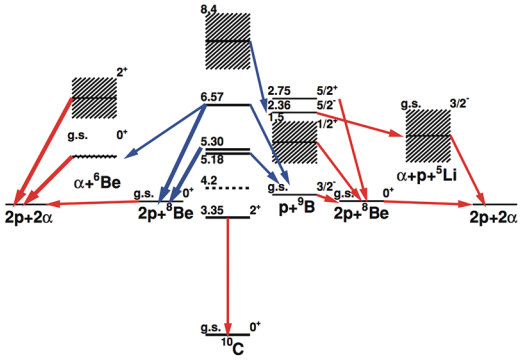

Fig. 34. Level scheme and decay paths for ^{10}C. Figure reprinted with permission from ref. [185]. © 2008, The American Physical Society.

treatment that includes both complete and incomplete fusion [179,180] has shown that the fusion probability should be enhanced (suppressed) by the presence of the halo for proton-halo (neutron-halo) nuclei. A gradual process of Coulomb polarization, eventually leading to breakup, was proposed as the mechanism explaining the fusion enhancement. After the breakup, the relevant Coulomb barrier is that between the core and the target, which is lower than the original projectile-target barrier, so the core can more easily penetrate it. A similar conclusion has been reached recently in ref. [181]. However, more theoretical work is needed to achieve a good description of the observed fusion enhancement above the barrier for the proton-halo system $^{8}\mathrm{B} + {}^{58}\mathrm{Ni}$.

11 Reactions with ^{10}C

The proton-rich carbon isotope ^{10}C has a half-life of $t_{1/2} = 19.3$ s. Once excited, it can decay by three possible channels: $2\mathrm{p} + {}^{8}\mathrm{Be}$, $^{9}\mathrm{B} + \mathrm{p}$ and $^{6}\mathrm{Be} + \alpha$, with threshold energies of 3.820 MeV, 4.006 MeV and 5.101 MeV, respectively (fig. 34). This nucleus is supposed to have a Brunnian (super-borromean) configuration, which would correspond to four interconnected rings (instead of three for a borromean system) associated with the four-body $2\alpha + 2\mathrm{p}$ configuration [182,183]. This unusual proposed structure has been investigated by resonance-decay spectroscopy [184–186]. The experiment utilized a 107 MeV ^{10}C beam produced by the p(^{10}B, ^{10}C)n reaction and separated from other reaction products by the MARS spectrometer at the Texas A&M University K500 cyclotron facility [187]. The beam was 99.5% pure and had an intensity of 2×10^5 pps. The ^{10}C nucleus was excited above 8 MeV via interactions with ^{9}Be and ^{12}C targets and all the decay products were detected by an array of four Si-strip ΔE-E telescopes. All the decay channels shown in fig. 34 were observed in coincidence measurements. Proton-proton angular correlations, resonance widths, energy distributions of di-proton and sequential two-proton decays, as well as $2\mathrm{p} + 2\alpha$, $\mathrm{p} + 3\alpha$ and other decay modes from excited resonant states, were studied.

Low-energy radioactive ^{10}C beams have also been used to investigate the unusual inversion of orbitals in the proton-rich nucleus ^{11}N. In general, a one-neutron halo nucleus mainly consists of a valence nucleon in an $s_{1/2}$ orbital coupled to a core. This is indeed the case for ^{11}Be, where the ground state has $J^\pi = 1/2^+$ in contradiction with the shell-model prediction that the odd neutron should be in a $p_{1/2}$ state leading to $J^\pi = 1/2^-$. This same inversion was then observed in ^{11}N, which is unbound to proton decay, and could be investigated by resonant elastic scattering with a ^{10}C beam [188,189].

11.1 Elastic scattering of ^{10}C

In the last decade only one experiment has been reported on the elastic scattering of a ^{10}C beam on medium- to heavy-mass targets. Although at a little above the energy of the proposed scope of this review, this interesting experiment corresponds to the measurement of angular distributions for quasielastic scattering of $^{10}\mathrm{C} + {}^{nat}\mathrm{Pb}$ at 226 and 256 MeV (3 times the Coulomb barrier) [190]. The motivation was to search for a Coulomb-rainbow diffraction pattern, which is strongly suppressed in the case of elastic scattering with the neutron-rich nuclei ^{11}Be [126], ^{11}Li [81] and ^{6}He [18], but not for the proton-rich-nuclei ^{8}B [158] and ^{17}F [191]. The experiment was performed with a ^{10}C beam of intensity $\approx 3 \times 10^4$ pps, produced at the Heavy Ion Research Facility in Lanzhou, China [192] The setup consisted of two PPACs and time-of-flight (TOF) to identify and reconstruct the incident angles, and two E-ΔE Si-detector telescopes to detect the scattered particles. After a careful OM analysis with Woods-Saxon and double-folding SP potentials, a clear Coulomb-rainbow pattern was observed in both angular distributions. They also determined the total reaction cross sections and compared with other existing data on ^{6}Li, ^{7}Be, ^{8}B, ^{10}C, ^{10}B and ^{11}C. Using the reduction method proposed in ref. [67] they found that, except for ^{8}B, there were no distinct differences among the weakly-bound and stable projectiles at above barrier energies, indicating that the influence of the additional open channels for these projectiles is small.

11.2 Fusion of ^{10}C

A fusion cross section measurement for $^{10}\mathrm{C} + {}^{12}\mathrm{C}$ at near-Coulomb-barrier energies was reported in ref. [193]. The motivations for this experiment were i) to investigate the importance of transfer reactions and intrinsic excitations of the target and projectile in the enhancement of fusion cross sections, ii) to compare fusion cross sections of carbon isotopes with theory in preparation for later efforts to investigate the importance of pycnonuclear fusion reactions [194] in the crust of accreting neutron stars, iii) to develop the technique of using a multi-sampling ionization chamber (MUSIC) [195] as an active target for fusion cross section measurements. These experiments were performed at the ATLAS (Argonne Tandem Linac Accelerator System) facility in Argonne National Laboratory,

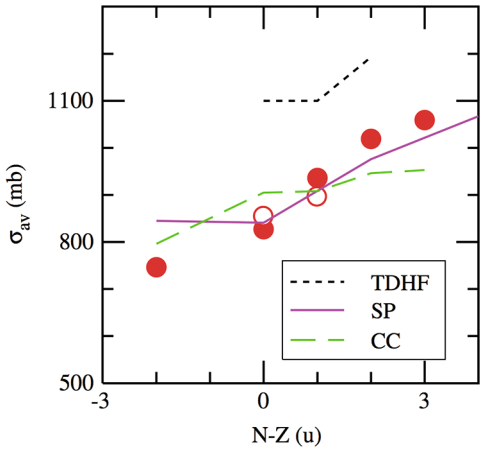

Fig. 35. Averaged fusion cross sections for the carbon isotopes $^{10,12-15}$C on a ^{12}C target. Experimental data (circles) are compared with OM predictions using the São Paulo (SP) potential (solid line), a coupled-channel calculation (dashed line), and a time-dependent Hartree-Fock (TDHF) prediction (dotted line). The open circles are data taken from ref. [196]. Figure reprinted with permission from ref. [193]. © 2014, The American Physical Society.

and also included fusion cross section measurements of ^{12,13,14,15}C. The latter two will be discussed in following sections of this review. The ^{10}C beam was produced with an intensity of about 5×10^2 pps, which was sufficient to be used in association with the active-target technique. The MUSIC detector was filled with CH_4 gas, and fusion cross sections for $^{10}\mathrm{C} + {}^{12}\mathrm{C}$ were obtained in the range from $E_{c.m.} = 9.5$–18.5 MeV. The averaged cross sections measured between 14 and 17 MeV for the carbon isotopes, $^{10,12-15}$C, are shown in fig. 35, where the results of several calculations are also plotted for comparison. As can be observed in the figure, there is an increase in the fusion cross section for higher $N - Z$ that is stronger than the usual R^2 dependence. Also, a coupled-channels calculation with one- and two-phonon excitation and mutual quadrupole and octupole excitations in the projectile and target gives a better prediction as compared with OM (São Paulo Potential with no free parameters) and TDHF calculations. The OM predictions fail rather badly in this case, possibly indicating some influence of the unusual structure of the ^{10}C nucleus.

12 Reactions with ^{11}C

12.1 Elastic scattering of ^{11}C

In the past decade, the only experiment performed with a ^{11}C beam was elastic scattering of ^{11}C on ^{nat}Pb, at the Heavy Ion Research Facility in Lanzhou, China [190]. This measurement was reported together with the one for the $^{10}\mathrm{C} + {}^{nat}\mathrm{Pb}$ system discussed above, and the motivation was the same: to search for a Coulomb-rainbow diffraction pattern in the elastic scattering angular distribution. The ^{11}C beam was 226 and 256 MeV with an intensity similar

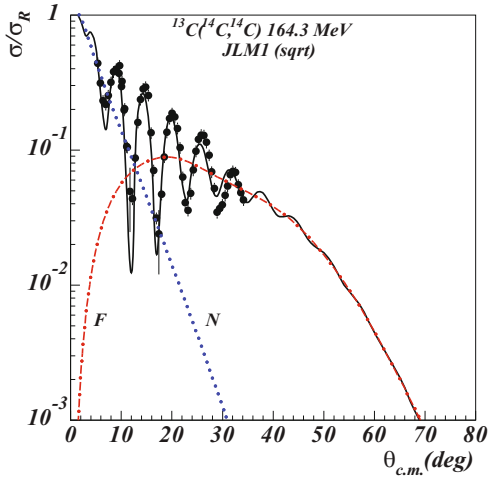

Fig. 36. Angular distribution for the elastic-scattering cross section ratio to Rutherford for ^{14}C on ^{13}C. The symbols are the data and the curves are the results of an OM calculation decomposed into nearside (dotted line) and farside (dot-dashed line) contributions, as well as their coherent sum (solid black). Figure reprinted with permission from ref. [201]. © 2014, The American Physical Society.

to that for ^{10}C, *i.e.*, 3×10^4 pps. The observed angular distributions do not show any suppression of the Coulomb-rainbow diffraction pattern.

13 Reactions with ^{14}C

Although radioactive, the lifetime of ^{14}C is quite long (5730 y). Thus, ^{14}C beams can be produced with similar quality and intensity as stable ^{12}C. Because of this, several experiments for elastic, inelastic, and transfer reactions using ^{14}C beams have been performed, and these were reviewed in ref. [1]. Most of these experiments were performed to investigate the role of one- and two-neutron stripping. Also, some reactions induced by low-energy ^{14}C beam have been used to populate highly-excited levels in some specific neutron-rich nuclei, such as ^{139}Ce populated by the ^{130}Te(^{14}C, 5n) [197] reaction, ^{21}F populated by the ^{9}Be(^{14}C, np) reaction [198], ^{22}F populated by the ^{9}Be(^{14}C, p) reaction [199] and ^{58}Fe populated by the ^{48}Ca (^{14}C, 4n) reaction [200]. The final nuclei were studied using γ-ray techniques. The current review is limited to studies of elastic scattering, transfer, breakup and fusion in order to investigate nuclear reaction mechanisms, so these works related to nuclear-structure investigation will not be further discussed.

13.1 Elastic scattering of ^{14}C

Elastic scattering of ^{14}C on a ^{13}C target was measured at the Texas A&M Cyclotron Institute (TAMU-CI) [201]. A 164 MeV ^{14}C beam obtained from the K500 superconducting cyclotron impinged onto a 104 μg/cm^2 ^{13}C target.

The main purpose of this measurement was to obtain the optical-model parameters for a later DWBA analysis of a transfer reaction measured in the same experiment. The data and the results of the OM analysis with a double-folding potential are illustrated in fig. 36, where the good quality of the fit can be seen.

13.2 Transfer reactions with ^{14}C

Transfer reactions have proven to be a powerful tool in the investigation of nuclear spectroscopy that is important for astrophysical reactions. The indirect method of using transfer reactions to obtain spectroscopic factors (SF) and/or asymptotic normalization coefficients (ANC) was recently applied with ^{14}C beams and these experiments are reviewed below.

13.2.1 ^{14}C + ^{6,7}Li

Two α-particle transfer reactions induced by a ^{14}C beam (^{6}Li(^{14}C, d) and ^{7}Li(^{14}C, t)) were measured at the John D. Fox Superconducting Accelerator Laboratory at Florida State University [202]. Beams of 8.8 MeV and 11.5 MeV ^{14}C impinged onto ^{6}Li and ^{7}Li targets, respectively. Five silicon ΔE-E telescopes were used to detect the light recoils (deuterons/tritons) produced by the α-transfer reactions. At these sub-Coulomb energies the reaction is assumed to be peripheral. In this case the dependence of the DWBA cross section on the parameters of the optical-model potentials is minimized and the ANCs of the 1^- (6.198 MeV) and 3^- (6.404 MeV) excited states in ^{18}O could be extracted. These ANCs were then used to infer information concerning the ^{14}C$(\alpha,\gamma)^{18}$O capture reaction. The combined final value of the ANC^2 for the state at 6.198 MeV in ^{18}O, from both (^{6}Li, d) and (^{7}Li, t) measurements, was 2.8 ± 0.7 (fm^{-1}). The 3^- state is unbound by 177 keV but it was treated as a bound state with small binding energy in the analysis. A width $\Gamma_\alpha = (7.8 \pm 2.7) \times 10^{-14}$ eV was determined from the ^{7}Li(^{14}C, t) reaction. Both of the above parameters were later used to determine the ^{14}C$(\alpha,\gamma)^{18}$O reaction rate, improving the uncertainty by five orders of magnitude in the range of interest for core helium flashes in low-mass stars.

13.2.2 ^{14}C + ^{10}Be

The ^{10}Be(^{14}C, ^{10}Be*)^{14}C and ^{10}Be(^{14}C, ^{12}Be*)^{12}C transfer reactions were used to populate ^{10}Be and ^{12}Be to energies above the α + ^{6}He, α + ^{8}He, and ^{6}He + ^{6}He thresholds [203]. The motivation of this experiment was to investigate the ^{6}He + ^{6}He and ^{4}He + ^{8}He decays of the molecular rotational band in ^{12}Be. An 88.5 MeV ^{14}C beam was produced by the superconducting LINAC facility at Florida State University. The He-like decay fragments were detected in coincidence in an array of two (50 mm × 50 mm) silicon double-sided strip detector (DSSD) telescopes. The excitation energy spectrum

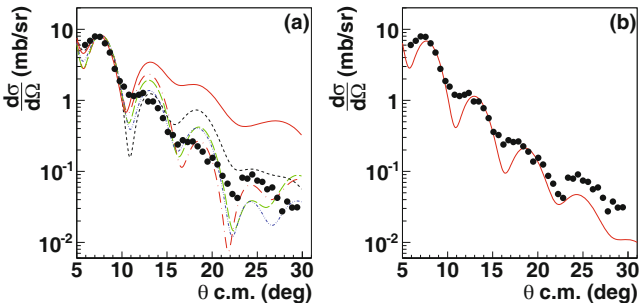

Fig. 37. Angular distribution for the ^{13}C(^{14}C, $^{15}C_{gs}$)^{12}C neutron-transfer reaction to the ground state. The curves are the results of calculations using (a) different WS potentials and (b) a double-folding potential. See ref. [201] for more details. Figure reprinted with permission from ref. [201]. © 2014, The American Physical Society.

for ^{10}Be was reconstructed from the α and ^{6}He relative energy in the ^{10}Be(^{14}C, α-^{6}He)^{14}C reaction. Many peaks were observed corresponding to excited states in ^{10}Be. As for the ^{10}Be(^{14}C, ^{6}He-^{6}He)^{12}C and ^{10}Be(^{14}C, α-^{8}He)^{12}C reactions, no evidence for fragments from the breakup of ^{12}Be* was observed. However, upper limits for the integrated cross sections of 50 and 300 nb were assigned, for these transfer reactions, respectively. These values are dependent on the angular distributions used in Monte Carlo simulations of the detection efficiency.

13.2.3 ^{14}C + ^{13}C

The ^{13}C(^{14}C, ^{15}C) transfer reaction was used to obtain spectroscopic factors (SF) for the $\langle ^{15}C_{gs}|^{14}C_{gs} + n\rangle$ and $\langle ^{15}C^{*}(0.740)|^{14}C_{gs} + n\rangle$ bound systems [201]. These SFs were then used to infer information concerning the direct, non-resonant ^{14}C(n, γ)$^{15}C_{gs}$ and ^{14}C(n, γ)^{15}C*(0.740) capture reactions with the phenomenological potential method [76] and the code RADCAP [204]. This measurement was performed using a 12 MeV/nucleon ^{14}C beam from the K500 superconducting cyclotron at TAMU-CI. The measured angular distribution for the ^{13}C(^{14}C, $^{15}C_{gs}$) transfer reaction can be seen in fig. 37, together with the results of DWBA calculations using different potentials.

The SFs for both the ground and first excited states were obtained by normalizing the calculated differential cross section to the corresponding experimental cross sections at the main stripping peak of the angular distributions. As one can see in this figure, all potentials give good results for the ground state in the region of the main peak (5° to 11°). The beam energy for this experiment was chosen to ensure that the neutron transfer reaction was peripheral. The ANC can thus be extracted and used to normalize the corresponding low-energy capture reaction, which is also a peripheral process governed by the asymptotic tail of the radial overlap function, even for a neutron-capture reaction. In this work, the ANCs for the ground state and first excited state in ^{15}C were evaluated from the SFs obtained from the transfer reaction using a method proposed in ref. [205], according to which the ANCs of the overlap functions are included in the transfer analysis. The obtained values were $ANC^2_{2s1/2} = 2.09 \pm 0.29$ (fm^{-1}) and $ANC^2_{1d5/2} = 4.48 \pm 0.58$ (fm^{-1}) from ^{13}C(^{14}C, ^{15}C). They also obtained $ANC^2_{2s1/2} = 1.77 \pm 0.21$ (fm^{-1}) and $ANC^2_{1d5/2} = 4.08 \pm 0.49$ (fm^{-1}) using the d(^{14}C, p)^{15}C reaction. As a final conclusion, the authors claimed that the applied method gave a higher SF value for the first excited state of ^{15}C ($E_x = 0.740$ MeV) which is not consistent with the expected value (less than 1) for a strong single-particle state, and from a mirror-symmetry comparison with the SF for ^{15}F.

13.3 Fusion of ^{14}C

Since ^{14}C is the core of the neutron-halo nucleus ^{15}C, fusion measurements induced by this nucleus have also been reported in connection with ^{15}C experiments. These are reviewed in the ^{15}C section below.

13.3.1 ^{14}C + ^{12}C

Fusion cross sections for ^{14}C + ^{12}C at near-Coulomb-barrier energies were reported in ref. [193]. See the section on ^{10}C fusion above.

13.3.2 ^{14}C + ^{208}Pb

An excitation function for fusion of ^{14}C + ^{208}Pb was obtained in the 1980s [206] at energies close to the Coulomb barrier. This dataset was recently re-analyzed by Sagaidak *et al.* [207]. In this new analysis, nuclear potentials which could describe both sub-barrier fusion and heavy-cluster (^{14}C) decay were investigated. A series of nuclear potentials which could be used in barrier-penetration models to obtain the ^{14}C decay probabilities were found.

13.3.3 ^{14}C + ^{232}Th

Fusion cross section measurements at energies in the vicinity of the Coulomb barrier are reported for the ^{14}C+^{232}Th system in ref. [208]. ^{14}C is a spherical system and fusion induced by this nucleus was used as a reference for any unusual characteristics of ^{15}C-induced fusion. ^{14}C was delivered as a primary beam by the ATLAS accelerator at Argonne National Laboratory. The fusion-fission fragments were detected using four 5×5 cm^2 Si surface barrier detectors, each divided into four quadrants. The experimental fusion-fission cross sections were compared with a coupled-channel calculation. Only the inelastic channels were considered, using deformed Woods-Saxon potentials to describe the static quadrupole and octupole of the ^{232}Th target. Good agreement was obtained. The transfer channel was later considered, in the analysis of Sargsyan *et al.* [209], without changing the previous conclusions.

14 Reactions with ^{15}C

The ^{15}C nucleus is a good candidate for a one-neutron halo system. This nucleus can be described as an $s_{1/2}$ valence neutron coupled to a ^{14}C core with a low separation energy of $S_n = 1.218$ MeV. The narrow measured momentum distribution for the one-neutron removal reaction [210] and the observed large interaction radius as compared to ^{14,16}C isotopes [211], corroborate this conclusion. The low binding energy of the valence neutron in ^{15}C makes it a good candidate to investigate possible effects of the nucleon-transfer mechanism on elastic scattering and fusion.

14.1 Elastic scattering of ^{15}C

14.1.1 ^{15}C + ^{208}Pb

Although it is potentially very interesting, there are no data related to elastic scattering of ^{15}C on medium to heavy nuclei at energies around the Coulomb barrier. However, coupled-channels calculations for elastic scattering of ^{15}C + ^{208}Pb system at 54 MeV have been performed by Keeley and Alamanos [212]. They showed that the extended wave function of the valence neutron in ^{15}C leads to a large transfer probability at large radii, larger than for more conventional nuclei. The inelastic channels and (^{15}C, ^{14}C) transfer ($Q = +2.70$ MeV) were included, but not (^{15}C, ^{16}C) ($Q = -3.10$ MeV) transfer. It was also suggested that breakup couplings might be as important as single-neutron transfer. Data on ^{15}C elastic scattering would be very welcome to check these possibilities.

14.2 Fusion of ^{15}C

14.2.1 ^{15}C + ^{12}C

Fusion cross sections for ^{15}C + ^{12}C at near-Coulomb-barrier energies were reported in ref. [193]. See the section on ^{10}C fusion above.

14.2.2 ^{15}C + ^{208}Pb and ^{15}C + ^{232}Th

The question of whether fusion with a weakly-bound projectile is enhanced or suppressed has been addressed by Keeley and Alamanos [212], who extended the previously mentioned coupled-channel calculations for elastic scattering to the near-barrier fusion regime for ^{15}C+^{208}Pb. They found a significant hindrance of the total fusion cross section for energies above the barrier due to single-neutron stripping couplings linked to the dominant $2s_{1/2}$ structure of the ^{15}C ground state.

Fusion data for the ^{15}C + ^{232}Th system were reported in ref. [208]. Fission fragments from the decay of the compound nucleus ^{247}Cm were detected in coincidence using four Si surface barrier detectors surrounding a ^{232}Th target. The ^{15}C beam was produced by the in-flight technique with the d(^{14}C, ^{15}C)p reaction. A fusion excitation function from 54 to 70 MeV was obtained. The data are shown in fig. 38, together with those for the ^{13,14}C+^{232}Th systems and the ^{12}C + ^{232}Th system from ref. [213]. The

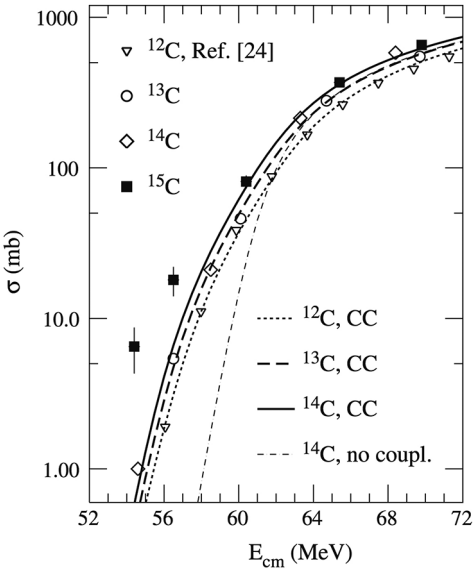

Fig. 38. Excitation function of the fusion-fission reactions for ^{12,13,14,15}C+^{232}Th. The symbols correspond to the data for the isotope indicated. The curves are the result of coupled-channels calculations as indicated. Figure reprinted with permission from ref. [208]. © 2011, The American Physical Society.

fusion-fission cross section for ^{15}C+^{232}Th is enhanced by a factor 5 in comparison with those for the other carbon isotopes at the lowest energies. The results of some coupled-channel calculations using a deformed Woods-Saxon potential with static quadrupole and hexadecapole deformations are also shown. The solid line in this figure corresponds to a coupled-channels calculation for ^{14}C. To describe the data for ^{15}C, the authors assumed a spectator model for the valence neutron, whereby ^{15}C was assumed to have the same excitation-energy spectrum and ion-ion potential as ^{14}C. The result for ^{15}C, therefore, overlaps with that for ^{14}C and is not shown in the figure. The calculation does not reproduce the data at sub-barrier energies, indicating that additional effects are responsible for the strong enhancement. This problem in the calculation was addressed by Sargsyan *et al.* [209], who investigated the possible influence of neutron transfer in sub-barrier fusion. Their calculation is based in the quantum diffusion approach, which takes into account the fluctuation and dissipation effects in collisions of heavy ions. Low-lying collective modes are included through deformation of the potentials. Transfer reactions were also taken into account by changing the deformations of the interacting nuclei. The agreement between theory and experiment was improved for the ^{12,13,14}C + ^{232}Th system but the data for ^{15}C + ^{232}Th were still underestimated at sub-barrier energies. The authors argued that the role of the breakup channel, which was not included in these calculations, might be much more important than that of transfer. Thus, the ^{15}C + ^{232}Th system deserves further investigation.

15 Reactions with ^{12}N

^{12}N decays to ^{12}C by β^+ emission with a half-life of 11 ms. It has a low proton separation energy (0.6 MeV) and some

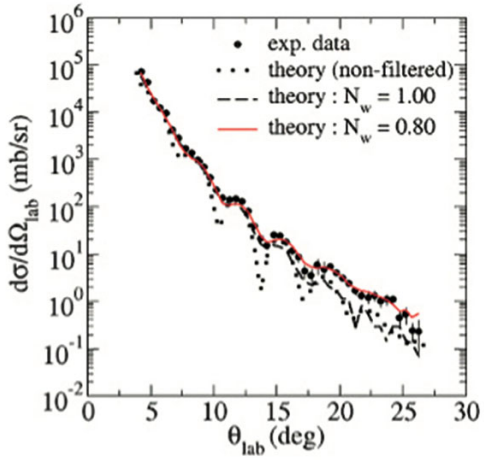

Fig. 39. Elastic-scattering angular distribution for ^{12}N on ^{14}N and ^{12}C from a $C_3H_6N_6$ target, at $E_{lab} = 137.6$ MeV. Figure reprinted with permission from ref. [216]. © 2009, The American Physical Society.

evidence exists showing that it may have a one-proton halo structure [214,215]. There is no reported experiment with ^{12}N projectiles at energies lower than 10 MeV/A, but a measurement taken at an energy slightly above this value is described below.

An elastic-scattering angular distribution of ^{12}N on a melamine target, $C_3H_6N_6$, was measured in ref. [216]. The projectile energy at the center of the target was 137.6 MeV and the scatterings from ^{12}C and ^{14}N could not be distinguished from each other. The inclusive angular distribution is shown in fig. 39, where the contribution of each target is related to the stoichiometry of carbon and nitrogen in melamine (1:2), as well as to the respective cross sections. The dashed curve corresponds to a calculation using double-folding potentials that had been proved to work well for elastic scattering of radioactive nuclei such as ^{7}Be, ^{8}B, ^{11}C, ^{13}N, and ^{17}F. The discrepancy with experiment at large angles indicates that a less absorptive potential is needed to describe the ^{12}N data. Changing the renormalization coefficient for the imaginary part of the potential from 1.0 to 0.8 was sufficient to obtain a good description of the data, as shown with the solid line.

A separate experiment for elastic scattering of ^{12}N from a ^{12}C target was also reported in ref. [216], but the much thicker target prevented observation of the Fraunhofer oscillations in the respective angular distribution. An angular distribution for the one-proton transfer reaction ^{14}N(^{12}N, ^{13}O)^{13}C also was reported in ref. [216]. Carrying out appropriate DWBA calculations and using the ANC (Asymptotic Normalization Coefficient) method, the authors were able to deduce the astrophysical S-factor for the ^{12}N(p, γ)^{13}O proton capture reaction.

16 Reactions with ^{13}N

The ^{13}N nucleus is unstable, decaying by β^+ emission with a half-life of 9.97 m. It is also weakly bound, with a proton separation energy of 1.9 MeV. Reactions of this projectile with targets of ^{11}B, ^{12,13}C and ^{14}N were reviewed in ref. [1]. Additional measurements with a ^{9}Be target will be briefly described here.

Evaporation residues from the ^{13}N + ^{9}Be fusion reaction have been measured in ref. [217] at $E_{lab} = 45$ MeV. The residue distribution was well described by statistical-model calculations using the code CASCADE and the extracted fusion cross sections were similar to the ones for the ^{10}B + ^{12}C system at the same energy in the center-of-mass reference frame. Both systems correspond to the same compound nucleus ^{22}Na, so no apparent influence on fusion of the weakly bound nature of the reactants in the former system was found.

17 Reactions with ^{17}F

The proton drip line nucleus ^{17}F decays into ^{17}O + β^+ with a half-life of 64.49 s. It has a low breakup threshold (0.6 MeV) into ^{16}O + p and its first excited state is a proton-halo state [218] which is bound by only 105 keV. Some reactions of ^{17}F with targets of ^{12}C, ^{14}N and ^{208}Pb were reviewed in ref. [1]. Additional measurements as well as some theoretical analyses will be described below. It can be anticipated that, given the exotic nature of ^{17}F, a lower reactivity than expected is generally observed.

17.1 Elastic scattering of ^{17}F

17.1.1 ^{17}F + ^{12}C

An angular distribution for quasielastic scattering of ^{17}F+ ^{12}C at 60 MeV was reported in ref. [219]. The experiment was performed at the CRIB facility of the CNS, University of Tokyo, where a 101 MeV ^{16}O primary beam was used to produce about 4×10^5 ^{17}F/s, through the d(^{16}O, ^{17}F)n reaction. Six ΔE-E telescopes were used to detect the scattered particles, covering an angular range of 5°–80°. Energy resolution was not enough to separate inelastic particles populating the 495 keV state in ^{17}F, but corresponding CDCC calculations indicated that their contribution is negligible. Optical-model calculations using a potential extrapolated from those fitting ^{16}O + ^{12}C elastic data at several energies produced a reasonable global description of the angular distribution, although not all maxima and minima in the data could be quantitatively reproduced.

The effect of coupling to the first 2^+ state in ^{12}C also was investigated, but this gave similar quality fits to the data as the single channel calculation. The calculated total reaction cross sections with and without the inclusion of the first 2^+ state in ^{12}C were 1417.6 mb and 1388.5 mb, respectively. CDCC calculations where continuum states of ^{16}O + p with relative energies going up to 12 MeV were discretized indicated that bu effects on the elastic channel are small.

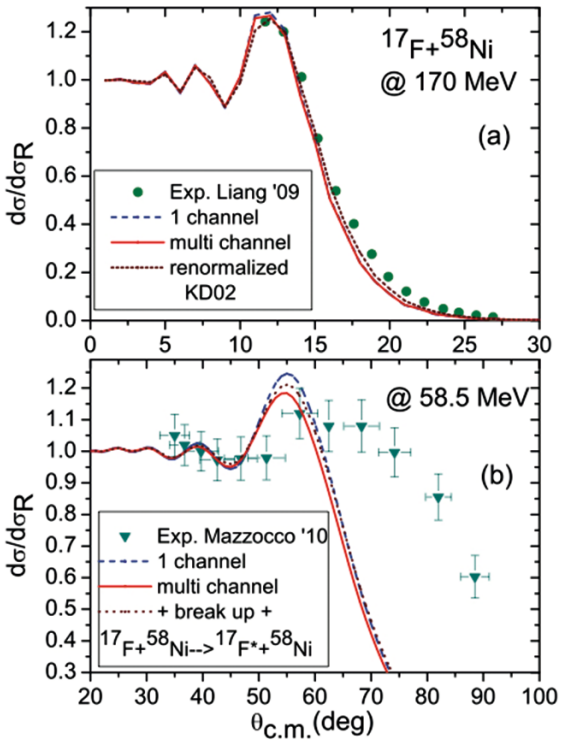

Fig. 40. Quasielastic-scattering angular distributions for ^{17}F+ ^{58}Ni at 170 MeV [220] and 58.5 MeV [222], and respective predictions from the MCDCC model [226]. Figure reprinted with permission from ref. [226]. © 2014, The American Physical Society.

17.1.2 ^{17}F + ^{58}Ni

An angular distribution for quasielastic scattering of ^{17}F+ ^{58}Ni at 10 MeV/A was reported in ref. [220]. A ^{17}F beam of $\sim 8 \times 10^6$ pps was produced by the ^{16}O(d, n) reaction at the HRIBF facility (Oak Ridge, TN, USA), bombarding a 1.0 mg/cm^2 ^{58}Ni target. Energy resolution prevented separation of several quasielastic processes, including inelastic scattering populating the first excited state of projectile and target and neutron pickup. A silicon surface barrier detector at 10° served to monitor the beam and a three stage telescope using 5×5 cm^2 silicon strip detectors (64 μm, 278 μm, 295 μm) was used to detect the reaction products in the angular range 8°–22°.

The cross sections were first normalized to the 10° monitor assuming Rutherford scattering, but comparison with optical-model predictions using two different potentials (one of them the São Paulo potential [33]) lead the authors to notice a deficiency in this normalization and introduce a renormalization factor of 1.2. The results are shown in fig. 40(a) with solid circles, along with theoretical predictions that will be described later at the end of the present section. Other reactions measured in ref. [220] will also be discussed later: quasielastic scattering of ^{17}F + ^{208}Pb (sect. 17.1.3), and breakup of ^{17}F on ^{58}Ni and ^{208}Pb (sect. 17.2).

CDCC calculations for this system, assuming a simple p + ^{16}O configuration for the projectile, were reported in ref. [221]. The maximum excitation energy and the number of discrete bins in the continuum were dictated by convergence of the calculated observables. By using three different combinations of core-target and p-target optical potentials, very good agreement with the data was found.

Quasielastic-scattering angular distributions for ^{17}F + ^{58}Ni at two near-barrier energies were reported in ref. [222]. A preliminary account of the same experiment was also given in ref. [223]. The facility EXOTIC at the Laboratori Nazionali di Legnaro, Italy, was used to produce ^{17}F secondary beams through the p(^{17}O, ^{17}F)n reaction, with energies of 54.1 ± 1.1 and 58.5 ± 1.0 MeV. The ^{17}F beams ($\sim 10^5$ pps), with respective purities of 93% and 96%, impinged onto a 1.0 mg/cm^2 ^{58}Ni target, yielding energies at the center of the target of 52.0 and 56.5 MeV, respectively. An array of eight ΔE-E silicon telescopes (EXODET), covering $\sim$ 70% of the full solid angle, was used to detect the resulting charged particles. Some inelastic-scattering events, as well as transfer processes and the ^{16}O + p breakup channel, could not be distinguished from the elastic channel. The measured angular distribution corresponding to the highest energy is displayed in fig. 40(b). The meaning of the curves in this figure will be described at the end of the present section.

An optical-model potential of Woods-Saxon shape with $V_0 = 2W_0 = 52.24$ MeV, $r_0 = r_i = 1.18$ fm, and $a_0 = a_i = 0.63$ fm, was used in ref. [222] as a starting point to fit the data. This potential follows a well-known standard parametrization. The real and imaginary depths were varied and the most relevant direct processes were included in a coupled-channel calculation. Reaction cross sections of 510.5 ± 55.3 (559.7 ± 64.3) mb were obtained for the lower (higher) energy, respectively. The estimated contributions from direct processes, which could not be experimentally separated from the elastic data, were: 67–74 mb from inelastic channels, 11–14 mb from breakup, and 7–15 mb from p-stripping. It was noted, however, that the later contribution should be considered as a lower estimate because only three final states in ^{59}Cu were considered for the stripped proton, and the actual contribution could in fact be on the order of 50–75 mb. A related uncertainty was added by the authors to the error bars reported for the reaction cross sections for the purpose of comparing with results for other systems.

A comparison with other systems was carried out in ref. [222] with a commonly-used prescription for data reduction. This comparison is extended in fig. 41 to include also all systems considered in ref. [156]. One can see that the reaction cross sections for ^{17}F do not follow the systematics found in ref. [156], whereby the most weakly bound systems (^{6}He, ^{8}B) show the largest reduced cross sections, followed first by less loosely-bound nuclei and finally by well-bound ones. In fig. 41, the reduced cross sections for ^{17}F, which is quite loosely bound (with a bu threshold even lower than those for ^{6}He, ^{6,7}Li and ^{7,9}Be), appear rather close to those of well-bound ^{16}O. One difference with ^{6}He and ^{8}B is that ^{17}F does not have a halo configuration in its ground state, but this would not explain the difference observed with respect to the Li and Be

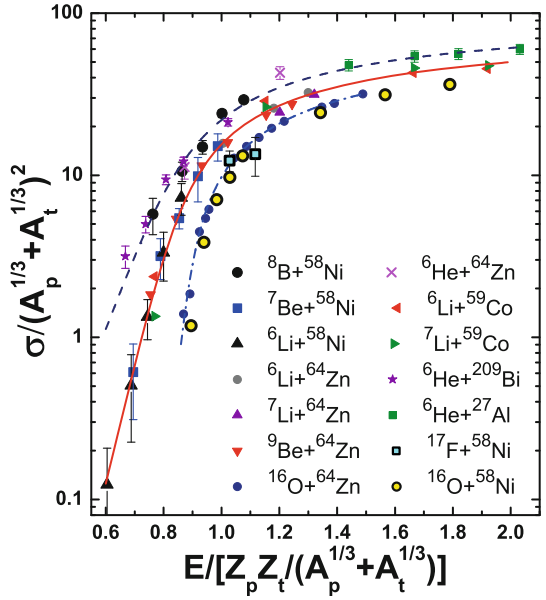

Fig. 41. Reduced reaction cross sections for several weakly bound projectiles, compared with the well bound ^{16}O projectile. For the original data sources see refs. [156,222].

isotopes. The apparently peculiar behaviour of ^{17}F could be at least partially related to an intrinsic limitation of the existing data reduction procedures when comparing total reaction cross sections [116]. This would possibly explain also the fact that different conclusions can be drawn from a comparison of some of the systems of fig. 41, but using an alternate data reduction procedure [224,225].

Theoretical calculations for the two datasets described above (from refs. [220,222]) were carried out in ref. [226] within a microscopic CDCC model (MCDCC) [227]. This model is based on a nucleon-target optical potential, which is folded with the projectile density to obtain the projectile-target interaction. The ^{17}F nucleus is assumed to have a ^{16}O + p configuration and an effective nucleon-nucleon (NN) interaction is used to build the respective internal many-body Hamiltonian, which is in turn used to obtain the projectile density. The target is structureless in this model. A total Hamiltonian for the projectile-target system was then given, which depends only on the assumed nucleon-target optical potential and the NN interaction, leading to a set of coupled-channel equations involving all projectile states. The CDCC method is then applied to solve these equations, by discretizing the projectile states in the continuum. According to ref. [227], the fact that the nucleon-target optical-model potentials are generally well known should confer a good predictive power on the model. In order to pick a proper nucleon-target optical-model potential, the performance of three different common potentials was carefully analyzed by comparing the results of single-channel calculations with elastic-scattering data for ^{17}F + ^{208}Pb at 170 and 90.4 MeV, as well as with data for p and n scattering from the same target at energies near and below 10 MeV. The Koning-Delaroche potential [228] was chosen.

The curves in fig. 40 show the MCDCC predictions for the ^{17}F + ^{58}Ni system at the two measured energies. In both cases, the influence of the couplings is small. At 170 MeV, the predicted cross sections are in good agreement with the data but at 58.5 MeV the description is not satisfactory. Inclusion of inelastic as well as breakup contributions in the calculation does not produce any substantial improvement. The authors of ref. [226] point out that the reasons for the observed discrepancy are not clear. One might notice that there was a rather large energy loss in the target in this particular case ($\sim$ 4.3 MeV [222]), which could partially explain the discrepancy since apparently the calculations were done assuming a projectile at 58.5 MeV.

17.1.3 ^{17}F + ^{208}Pb

A quasielastic scattering angular distribution for ^{17}F + ^{208}Pb at 141 MeV was reported in ref. [229]. The experiment was performed with the Radioactive Ion Beam Line at Lanzhou, China, using a 70 MeV/A ^{20}Ne primary beam on a 3.5 mm ^{9}Be primary target. The secondary target was a 2 mg/cm^2 ^{208}Pb foil. Three PPAC's and five Si detectors were used both to locate the beam position and direction and to detect the particles scattered into the angular range 6°–20°. Inelastic scattering populating the first excited state in either ^{17}F or ^{208}Pb could not be separated from the elastic-scattering yield. The data were presented only as a $\ln(\mathrm{d}\sigma/\mathrm{d}\theta)$ *vs.* θ^2 plot and a semiclassical analysis was attempted. A comparison with data for other systems within the same semiclassical framework was also shown in ref. [230]. The authors claim that a nuclear rainbow is observed for most of the considered systems and they estimate the ratio of the nuclear rainbow angle to the grazing angle. For ^{6}He and ^{17}F projectiles, this ratio is about one half (or less) of that for ^{4}He, ^{6}Li and ^{16,17}O.

A 1.84 mg/cm^2 lead target was also used in the experiment of ref. [220] which was described at the beginning of sect. 17.1.2, so a quasielastic-scattering angular distribution for ^{17}F + ^{208}Pb at 170 MeV also was obtained. An angular range of 8°–50° was covered in this case and, in contrast to the case of the ^{58}Ni target, the 10° monitor provided a proper data normalization so no renormalization was necessary. The results are presented in fig. 42 (top panel) along with the predictions of the MCDCC model [226], described in the previous section. Calculations with the São Paulo potential [33], using default parameters, provided a good description of the data [220].

Figure 42 also includes older data for the same system, not only at 170 MeV (top panel) but also at 98 MeV (middle panel) and 90.4 MeV (bottom panel). References for these older data are given in the figure caption, and they were reviewed in ref. [1]. To get a better description of the 170 MeV data within the MCDCC model, a renormalization of the real part of the Koning-Delaroche potential [228] by a factor 0.65 was required [226]. In the case of the data at 98 and 90.4 MeV, good agreement was not achieved but the authors claim that similar results are obtained with conventional CDCC calculations. For the

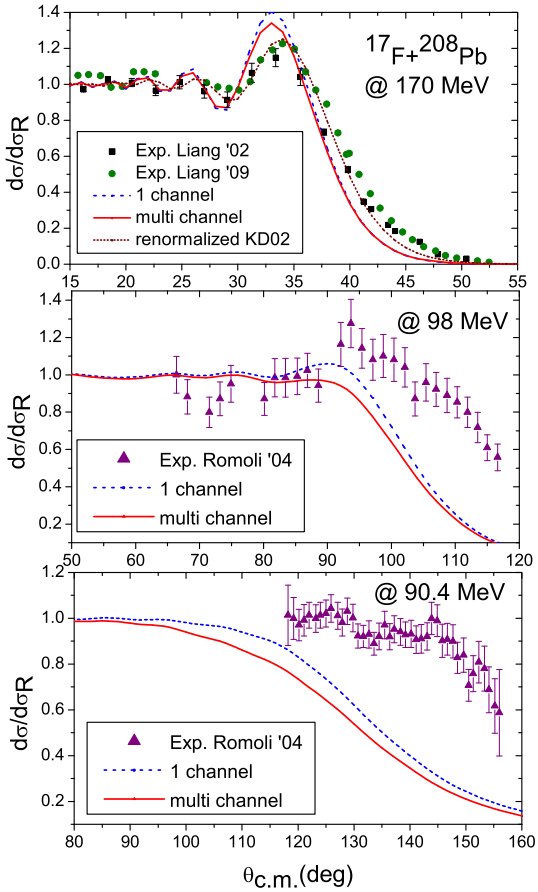

Fig. 42. Quasielastic-scattering angular distributions for ^{17}F+^{208}Pb at 170 MeV [220,231], 98 MeV [231] and 90.4 MeV [232], and respective predictions from the MCDCC model [226]. Figure reprinted with permission from ref. [226]. © 2014, The American Physical Society.

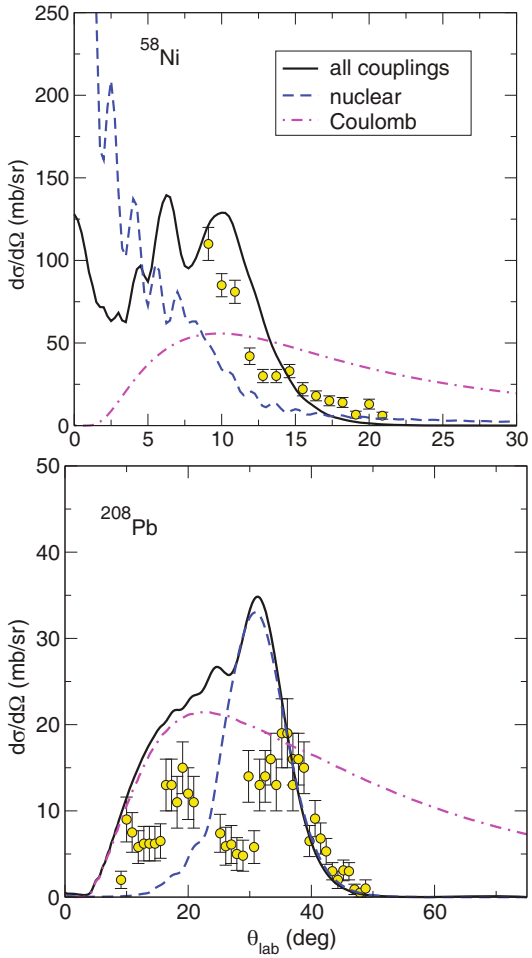

Fig. 43. Exclusive breakup angular distributions for ^{17}F + (^{58}Ni, ^{208}Pb) at 170 MeV [220], and respective CDCC calculations [221]. Figure reprinted with permission from ref. [221]. © 2012, The American Physical Society.

case of the 170 MeV data in fig. 42, the CDCC approach of ref. [221] that was briefly described in the third paragraph of sect. 17.1.2, was also applied to the ^{17}F + ^{208}Pb system, with very good agreement.

Quasielastic-scattering data for the ^{17}F+^{208}Pb system including the first excited state of ^{17}F (but not of ^{208}Pb) were reported in ref. [233] at $E_{lab} = 86 \pm 1$ MeV. The experiment was performed at the INFN-LNL, Italy, using the EXOTIC facility and the EXODET detection system that were mentioned earlier (sect. 17.1.2) in connection with ref. [222]. The data exhibited a nearly pure Rutherford behaviour so only an upper limit of 5 mb was determined for the respective reaction cross section. However, DWBA calculations indicated an inelastic cross section of 35 mb to the first excited state of ^{17}F, consistent with a total reaction cross section of 40 mb. Breakup data were also reported in this experiment, which will be mentioned in next section.

17.2 Breakup of ^{17}F

It was already mentioned in sect. 17.1.1 that the effects of bu couplings on the elastic scattering of ^{17}F + ^{12}C at 60 MeV are estimated to be small. The CDCC calculations of ref. [219] yielded 37.5 mb for the respective total bu cross section.

As mentioned in sect. 17.1.2, ^{16}O resulting from ^{17}F breakup when bombarding the ^{58}Ni target at 54.1 and 58.5 MeV (52.0 and 56.5 MeV at the target center, respectively) [222], could not be separated from pure elastic scattering. The CDCC calculations performed in ref. [222], which gave good fits to the quasielastic-scattering data, yielded respective estimations of 11.1 ± 0.7 mb and 14.2 ± 0.9 mb for the breakup cross sections at the two energies.

Exclusive breakup angular distributions for ^{17}F + (^{58}Ni, ^{208}Pb) at 170 MeV were measured at Oak Ridge [220] simultaneously to the respective quasielastic-scattering measurements described above (sects. 17.1.2, 17.1.3). The same experimental arrangement was used. Protons and oxygen ions were detected in coincidence, with efficiencies (estimated from Monte Carlo simulations) of 14%–19% for ^{58}Ni and 18%–40% for ^{208}Pb. The experimental results are shown by the circles in fig. 43. Corresponding bu calculations were

performed by assuming an $^{16}O + p$ configuration for ^{17}F and following the time evolution of the respective wave function along Coulomb trajectories [220]. The agreement with the experiment was good for the ^{58}Ni target but overestimated the forward angle data for $^{17}F + ^{208}Pb$ by a factor of two. The authors mention core excitation, which was not considered in the calculation, as a possible reason for this discrepancy. The predictions of these dynamic calculations look qualitatively similar to the solid curves in fig. 43, which will be described below.

The CDCC calculations of ref. [221], which were briefly described in the third paragraph of sect. 17.1.2, were also used to study the above breakup data for $^{17}F + (^{58}Ni, ^{208}Pb)$. The respective full calculations, including both nuclear and Coulomb couplings, are presented as solid curves in fig. 43, while the only-Coulomb (only-nuclear) calculations are displayed with dash-dot (dashed) curves, respectively. For ^{58}Ni, nuclear bu is small beyond the grazing angle ($\theta \sim 12°$) and the interference between both couplings is destructive at small angles and constructive around the maximum. The overall description of the data for this target is reasonably good (see the upper part of fig. 43). For ^{208}Pb, the nuclear contribution presents a maximum around the respective grazing angle ($\theta \sim 35°$), and Coulomb bu dominates at small angles but it is strongly suppressed beyond the grazing angle. Additional CDCC calculations in ref. [221] showed that the fact that the proton is charged produces a hindrance of the breakup cross section, consistent with a dynamic polarization effect resulting from a displacement of the proton behind the core, thus screening it from the full Coulomb interaction with the target. The angular distributions of bu protons and oxygen ions were also discussed. While the calculated ^{16}O distribution is fully inside the experimental angular range, a large fraction of the protons would be out of the region covered by the detectors. This could introduce additional uncertainties into the data which, combined with the fact that core excitations were not included in the calculations, may partially explain the discrepancy observed with the bu data for the ^{208}Pb target (see the lower part of fig. 43).

The experiment on $^{17}F + ^{208}Pb$ that was briefly described at the end of sect. 17.1.3 [233] also reported an exclusive breakup measurement at 86 MeV for this system, with a respective cross section of 0.6 ± 0.4 mb. Previous data from the same group [232] were also reanalyzed, yielding a breakup (total) reaction cros section of 33 ± 16 mb (74 mb) for the same system at 90.4 MeV. The strong energy dependence of the breakup cross section could not be explained in terms of a simple Coulomb dissociation estimation. A comparison with reaction cross sections induced by other nuclei on heavy targets showed a relatively small reactivity for ^{17}F, indicating that the loosely bound nature of this projectile is not playing an important role in the reaction dynamics.

17.3 Fusion of ^{17}F

Only one fusion measurement involving ^{17}F projectiles has been reported, in 1998, corresponding to the $^{17}F + ^{208}Pb$ system at near-barrier energies [234]. Even though the respective year of publication falls well beyond the general scope of the present review, it is considered that these results provide an important complement to achieve a global view of ^{17}F reactions, so they will be briefly described here.

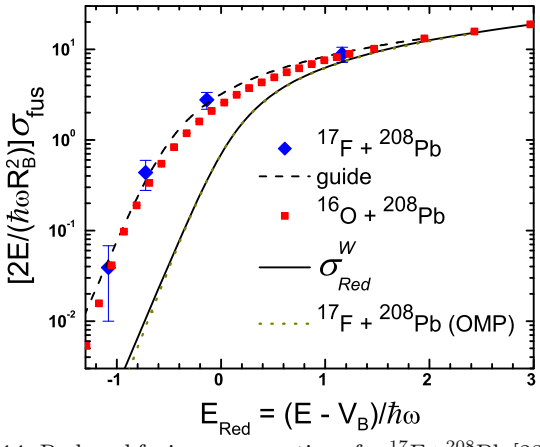

Fig. 44. Reduced fusion cross sections for $^{17}F + ^{208}Pb$ [234] and $^{16}O + ^{208}Pb$ [235]. The solid curve is the UFF (sect. 2.2.2) and the dotted curve corresponds to an optical-model calculation using a short range absorptive potential. The dashed curve is to guide the eye. The respective barrier parameters (V_B (MeV), R_B (fm), $\hbar\omega$ (MeV)) are (76, 11.7, 4.6) in the case of ^{16}O and (85.6, 11.6, 4.8) in the case of ^{17}F.

The experiment was performed at the Argonne National Laboratory (USA), where the $p(^{17}O, ^{17}F)n$ reaction was used to produce a ^{17}F beam of (1-2) $\times 10^5$ pps which bombarded a 500 μg/cm^2 ^{208}Pb target. Fission fragments corresponding to four bombarding energies between 87 and 99 MeV were measured in coincidence using four 5×5 cm^2 Si detectors, with a 7.8% total efficiency (determined from a Monte Carlo simulation). For comparison, the $^{19}F + ^{208}Pb$ fusion-fission reaction at similar energies was also measured. A plot of σ_{fus}/R^2 *vs.* E/V_C showed very similar results for the fusion with the two projectiles $^{17,19}F$, which was somehow unexpected because ^{19}F is well bound. For the lowest energy measured, the reduced cross section for ^{17}F was even lower than that of the heavier isotope. Figure 44 shows a comparison of fusion data for ^{17}F and ^{16}O projectiles with the same target ^{208}Pb, using the data reduction procedure of eq. (1). One can see that the results for both systems behave similarly, so the loosely bound nature of ^{17}F does not seem to produce any appreciable effect on the fusion process. An enhancement is observed with respect to the UFF, even for energies above the barrier. Canto *et al.* [31,32] analyzed both systems in this context and included the effects of coupling to low-energy inelastic excitations of the target. After renormalizing the experimental cross sections to take account of these effects (see eq. (3)), no enhancement was evident in the remaining values.

References

1. N. Keeley *et al.*, Prog. Part. Nucl. Phys. **63**, 396 (2009).
2. N. Keeley *et al.*, Prog. Part. Nucl. Phys. **59**, 579 (2007).
3. L.F. Canto *et al.*, Phys. Rep. **596**, 1 (2015).
4. M. Majer *et al.*, Eur. Phys. J. A **43**, 153 (2010).
5. E. Muskat *et al.*, Nucl. Phys. A **581**, 42 (1995).
6. J. Cook, K.W. Kemper, Phys. Rev. C **31**, 1745 (1985).
7. K.C.C. Pires *et al.*, Phys. Rev. C **83**, 064603 (2011).
8. K.C.C. Pires *et al.*, EPJ Web of Conferences **66**, 03071 (2014).
9. R. Lichtenthäler *et al.*, AIP Conf. Proc. **1139**, 76 (2009).
10. V. Morcelle *et al.*, Phys. Lett. B **732**, 228 (2014).
11. R. Lichtenthäler *et al.*, AIP Conf. Proc. **1224**, 461 (2010).
12. M. Rodríguez-Gallardo *et al.*, Phys. Rev. C **77**, 064609 (2008).
13. Ł. Standyło *et al.*, Phys. Rev. C **87**, 064603 (2013).
14. K. Rusek, Eur. Phys. J. A **41**, 399 (2009).
15. M. Rodríguez-Gallardo *et al.*, Phys. Rev. C **80**, 051601R (2009).
16. V.V. Parkar *et al.*, Acta Phys. Pol. **42**, 761 (2011).
17. A.M. Sánchez-Benítez *et al.*, Nucl. Phys. A **803**, 30 (2008).
18. L. Acosta *et al.*, Phys. Rev. C **84**, 044604 (2011).
19. E.F. Aguilera *et al.*, Phys. Rev. Lett. **84**, 5058 (2000).
20. J.P. Bychowski *et al.*, Phys. Lett. B **596**, 26 (2004).
21. P. DeYoung *et al.*, Phys. Rev. C **71**, 051601 (2005).
22. J.J. Kolata *et al.*, Phys. Rev. C **75**, 031302 (2007).
23. P.N. de Faria *et al.*, Phys. Rev. C **82**, 034602 (2010).
24. D. Escrig *et al.*, Nucl. Phys. A **792**, 2 (2007).
25. J.P. Fernández-García *et al.*, Phys. Lett. B **693**, 310 (2010).
26. V.V. Sargsyan *et al.*, Phys. Rev. C **86**, 054610 (2012).
27. V.V. Sargsyan *et al.*, Eur. Phys. J. A **45**, 45 (2010).
28. P.R.S. Gomes *et al.*, Phys. Rev. C **84**, 014615 (2011).
29. Y. Kucuk, Nucl. Phys. A **927**, 195 (2009).
30. M.S. Hussein *et al.*, Phys. Rev. C **73**, 044610 (2006).
31. L.F. Canto *et al.*, J. Phys. G: Nucl. Part. Phys. **36**, 015109 (2009).
32. L.F. Canto *et al.*, Nucl. Phys. A **821**, 51 (2009).
33. L.C. Chamon *et al.*, Phys. Rev. C **66**, 014610 (2002).
34. C.Y. Wong, Phys. Rev. Lett. **31**, 766 (1973).
35. P.R.S. Gomes *et al.*, Nucl. Phys. A **834**, 151 (2010).
36. A. Di Pietro *et al.*, Phys. Rev. C **69**, 044613 (2004).
37. A.M. Moro *et al.*, Nucl. Phys. A **787**, 463 (2007).
38. V. Guimarães *et al.*, Phys. Rev. Lett. **84**, 1862 (2000).
39. K. Ogata *et al.*, Nucl. Phys. A **805**, 447 (2008).
40. T. Matsumoto *et al.*, Phys. Rev. C **73**, 051602(R) (2006).
41. V. Scuderi *et al.*, Phys. Rev. C **84**, 064604 (2011).
42. A.S. Fomichev *et al.*, Phys. Part. Nucl. Lett. **9**, 496 (2012).
43. M. Herman *et al.*, Nucl. Data Sheeets **108**, 2655 (2007).
44. N.K. Skobelev *et al.*, Phys. Part. Nucl. Lett. **10**, 248 (2013).
45. A.A. Kulko *et al.*, J. Phys. G: Nucl. Part. Phys. **34**, 2297 (2007).
46. R. Wolski *et al.*, Eur. Phys. J. A **47**, 111 (2011).
47. S.M. Lukyanov *et al.*, Phys. Lett. B **670**, 321 (2009).
48. Yu.E. Penionzhkevich *et al.*, Phys. Rev. Lett. **96**, 162701 (2006).
49. V.I. Zagrebaev, Phys. Rev. C **67**, 061601 (2003).
50. A.A. Kulko *et al.*, Phys. At. Nucl. **70**, 613 (2007).
51. G. Marquínez-Durán *et al.*, Acta Phys. Pol. B **43**, 239 (2012).
52. G. Marquínez-Durán *et al.*, EPJ Web of Conferences **66**, 03058 (2014).
53. A. Lemasson *et al.*, Phys. Lett. B **697**, 454 (2011).
54. V.V. Parkar *et al.*, EPJ Web of Conferences **17**, 16009 (2011).
55. A. Lemasson *et al.*, Phys. Rev. Lett. **103**, 232701 (2009).
56. A. Lemasson *et al.*, Phys. Rev. C **82**, 044617 (2010).
57. Yu.E. Penionzhkevich *et al.*, Eur. Phys. J. A **31**, 185 (2007).
58. M.S. Basunia *et al.*, Phys. Rev. C **75**, 015802 (2007).
59. A. Navin *et al.*, Phys. Rev. C **70**, 044601 (2004).
60. A. Chatterjee *et al.*, Phys. Rev. Lett. **101**, 032701 (2008).
61. X. Gu *et al.*, Phys. Lett. B **343**, 31 (1995).
62. D. Howell *et al.*, Phys. Rev. C **88**, 025804 (2013).
63. H.M. Xu *et al.*, Phys. Rev. Lett. **73**, 2027 (1994).
64. I.J. Thompson, F.M. Nunes, *Nuclear Reactions for Astrophysics: Principles, Calculations and Applications of Low-Energy Reactions* (Cambridge University Press, 2009) p. 5, ISBN 978-0-521-85635-5.
65. S. Mukherjee *et al.*, Eur. Phys. J. A **45**, 23 (2010).
66. O. Camargo *et al.*, Phys. Rev. C. **78**, 034605 (2008).
67. P.R.S. Gomes *et al.*, Phys. Rev. C **71**, 017601 (2005).
68. J.M.B. Shorto *et al.*, Phys. Lett. B **678**, 77 (2009).
69. A. Barioni *et al.*, Phys. Rev. C **80**, 034617 (2009).
70. A. Pakou *et al.*, Eur. Phys. J. A **51**, 55 (2015).
71. A. Pakou *et al.*, Eur. Phys. J. A **51**, 90 (2015).
72. N. Keeley, Phys. Rev. C **80**, 064614 (2009).
73. I.J. Thompson, Comput. Phys. Rep. **7**, 167 (1988).
74. I.J. Thompson, `www.fresco.org.uk`.
75. V. Guimarães *et al.*, Phys. Rev. C **75**, 054602 (2007).
76. C.A. Bertulani, V. Guimarães, AIP Conf. Proc. **1304**, 183 (2010).
77. F.D. Becchetti *et al.*, Phys. Rev. C **71**, 054610 (2005).
78. E.F. Aguilera *et al.*, Phys. Rev. C **80**, 044605 (2009).
79. A. Gavron, Phys. Rev. C **21**, 230 (1980).
80. G.C. Ball *et al.*, J. Phys. G **38**, 024003 (2011).
81. M. Cubero *et al.*, Phys. Rev. Lett. **109**, 262701 (2012).
82. W. Loveland *et al.*, Phys. Rev. C **74**, 064609 (2006).
83. A.M. Vinodkumar *et al.*, Phys. Rev. C **80**, 054609 (2009).
84. V.I. Zagrebaev, V.V. Samarin, W. Greiner, Phys. Rev. C **75**, 035809 (2007).
85. A.B. Balantekin, G. Kocak, AIP Conf. Proc. **1072**, 289 (2008).
86. K. Hagino, N. Rowley, A.T. Kruppa, Comput. Phys. Commun. **123**, 143 (1999).
87. T. Nakamura *et al.*, Phys. Rev. Lett. **96**, 252502 (2006).
88. J.P. Fernàndez-García *et al.*, Phys. Rev. Lett. **110**, 142701 (2013).
89. A.M. Vinodkumar *et al.*, Phys. Rev. C **87**, 044603 (2013).
90. M.V. Andrés, J. Gómez-Camacho, Phys. Rev. Lett. **82**, 1387 (1999).
91. M. Rodríguez-Gallardo *et al.*, Phys. Rev. C **80**, 051601(R) (2009).
92. N. Keeley, K.W. Kemper, K. Rusek, Phys. Rev. C **88**, 017602 (2013).
93. W.Y. So *et al.*, Phys. Rev. C **89**, 057601 (2014).
94. W.Y. So *et al.*, Phys. Rev. C **90**, 054615 (2014).
95. J.P. Fernández-García *et al.*, Phys. Rev. C **92**, 014604 (2015).
96. A.V. Dobrovolsky *et al.*, Nucl. Phys. A **766**, 1 (2006).

97. E.C. Pinilla, P. Descouvement, D. Baye, Phys. Rev. C **85**, 054610 (2012).
98. K. Alder, A. Winther, *Electromagnetic excitations: Theory of Coulomb Excitation with Heavy Ions* (North-Holland, Amsterdam, 1975).
99. I. Tanihata *et al.*, Phys. Rev. Lett. **55**, 2676 (1985).
100. L.F. Canto *et al.*, Phys. Rev. C **52**, R2848 (1995).
101. N. Takigawa, M. Kuratani, H. Sagawa, Phys. Rev. C **47**, R2470 (1993).
102. M.S. Hussein *et al.*, Phys. Rev. C **46**, 377 (1992).
103. M.S. Hussein *et al.*, Phys. Rev. C **47**, 2398 (1993).
104. C.H. Dasso, A. Vitturi, Phys. Rev. C **50**, R12 (1994).
105. S. Verma *et al.*, Eur. Phys. J. ST **150**, 75 (2007).
106. S. Verma *et al.*, Eur. Phys. J. A **44**, 385 (2010).
107. A.T. Rudchik *et al.*, Eur. Phys. J. A **41**, 31 (2009).
108. K.C.C. Pires *et al.*, *Proceedings of the 12th International Conference on Nuclear Reaction Mechanisms, Varenna, Italy, 2009*, edited by F. Cerutti, A. Ferrari, Vol. **2** (CERN, 2010) p. 337, `http://cdsweb.cern.ch/record/1233497`.
109. A. Barioni *et al.*, Phys. Rev. C **84**, 014603 (2011).
110. J.C. Zamora *et al.*, Phys. Rev. C **84**, 034611 (2011).
111. H. Amro *et al.*, Eur. Phys. J. ST **150**, 1 (2007).
112. G. Tabacaru *et al.*, Phys. Rev. C **73**, 025808 (2006).
113. K. Horii *et al.*, Phys. Rev. C **81**, 061602(R) (2010).
114. K. Kalita *et al.*, Phys. Rev. C **73**, 024609 (2006).
115. V. Morcelle *et al.*, Phys. Rev. C **89**, 044611 (2014).
116. L.F. Canto *et al.*, Phys. Rev. C **92**, 014626 (2015).
117. R. Lichtenthäler *et al.*, Eur. Phys. J. ST **150**, 27 (2007).
118. E.F. Aguilera *et al.*, Phys. Rev. C **79**, 021601(R) (2009).
119. M. Mazzocco *et al.*, Phys. Rev. C **92**, 024615 (2015).
120. A. Gómez Camacho *et al.*, Nucl. Phys. A **833**, 156 (2010).
121. A. Gómez Camacho, E.F. Aguilera, Phys. Rev. C **90**, 064607 (2014).
122. R. Raabe *et al.*, Phys. Rev. C **74**, 044606 (2006).
123. E. Martinez-Quiroz *et al.*, Phys. Rev. C **90**, 014616 (2014).
124. A. Lepine-Szily, R. Lichtenthaler, V. Guimarães, Eur. Phys. J. A **50**, 128 (2014).
125. D. Tilley *et al.*, Nucl. Phys. A **745**, 155 (2004).
126. A. Di Pietro *et al.*, Phys. Rev. Lett. **105**, 022701 (2010).
127. A. Di Pietro *et al.*, Phys. Rev. C **85**, 054607 (2012).
128. D. Voulot *et al.*, Nucl. Instrum. Methods B **266**, 4103 (2008).
129. M. Hemalatha, Eur. Phys. J. Web of Conf. **66**, 03036 (2014).
130. J.N. Orce *et al.*, Phys. Rev. C **86**, 041303 (2012).
131. C.E. Svensson *et al.*, J. Phys. G **31**, S1663 (2005).
132. A. Yoshida *et al.*, Phys. Lett. B **389**, 457 (1996).
133. C. Signorini *et al.*, Nucl. Phys. A **735**, 329 (2004).
134. D.J. Hinde, M. Dasgupta, Phys. Rev. C **81**, 064611 (2010).
135. C. Signorini *et al.*, Eur. Phys. J. A **2**, 227 (1998).
136. M. Dasgupta *et al.*, Phys. Rev. C **81**, 024608 (2010).
137. H.G. Bohlen *et al.*, Phys. Rev. C **75**, 054604 (2007).
138. D.J. Millener *et al.*, Phys. Rev. C **28**, 497 (1983).
139. E. Kwan *et al.*, Phys. Lett. B **732**, 210 (2014).
140. C.E. Thorn *et al.*, Phys. Rev. Lett. **38**, 384 (1977).
141. V. Scuderi *et al.*, Acta Phys. Pol. B **44**, 463 (2013).
142. N. Keeley, J. Phys.: Conf. Ser. **381**, 012087 (2012).
143. T. Druet, P. Descouvemont, Eur. Phys. J. A **48**, 147 (2012).
144. W.Y. So *et al.*, Phys. Rev. C **92**, 014627 (2015).
145. R. de Diego *et al.*, Phys. Rev. C **89**, 064609 (2014).
146. N.C. Summers, F.M. Nunes, I.J. Thompson, Phys. Rev. C **74**, 014606 (2006).
147. L. Acosta *et al.*, Eur. Phys. J. A **52**, 461 (2009).
148. K. Rusek *et al.*, Acta Phys. Pol. B **43**, 233 (2012).
149. V. Pesudo *et al.*, Acta Phys. Pol. **45**, 375 (2014).
150. M. Mazzocco *et al.*, Eur. Phys. J. ST **150**, 3740 (2007).
151. T. Kubo *et al.*, Nucl. Instrum. Methods B **70**, 309 (1992).
152. B. Paes *et al.*, Nucl. Phys. A **890-891**, 1 (2012).
153. F.M. Nunes, I.J. Thomson, Phys. Rev. C **59**, 2652 (1999).
154. J. Lubian *et al.*, Phys. Rev. C **79**, 064605 (2009).
155. L.F. Canto *et al.*, Phys. Rev. C **80**, 047601 (2009).
156. J.J. Kolata, E.F. Aguilera, Phys. Rev. C **79**, 027603 (2009).
157. N. Keeley *et al.*, Nucl. Phys. A **834**, 792 (2010).
158. Y.Y. Yang *et al.*, Phys. Rev. C **87**, 044613 (2013).
159. R.S. Mackintosh, D.Y. Pang, Phys. Rev. C **88**, 014608 (2013).
160. R.S. Mackintosh, Phys. Rev. C **88**, 054603 (2013).
161. A. Gómez Camacho *et al.*, Phys. Rev. C **84**, 034615 (2011).
162. E.F. Aguilera *et al.*, Phys. At. Nucl. **71**, 1163 (2008).
163. T.L. Belyaeva *et al.*, Phys. Rev. C **80**, 064617 (2009).
164. J. Lubian *et al.*, Phys. Rev. C **78**, 064615 (2008).
165. L. Lubian *et al.*, Nucl. Phys. A **834**, 802 (2010).
166. E.F. Aguilera *et al.*, Phys. Rev. C **81**, 011604(R) (2010).
167. E.F. Aguilera *et al.*, Phys. Rev. C **83**, 021601(R) (2011).
168. E.F. Aguilera *et al.*, Phys. Rev. Lett. **107**, 092701 (2011).
169. A. Pakou *et al.*, Phys. Rev. C **87**, 014619 (2013).
170. A. Pakou *et al.*, Phys. Rev. C **87**, 049901(E) (2013).
171. J. Rangel *et al.*, Eur. Phys. J. A **49**, 57 (2013).
172. E.F. Aguilera *et al.*, Phys. Rev. C **93**, 034613 (2016).
173. R. Wolski, Phys. Rev. C **88**, 041603(R) (2013).
174. E.F. Aguilera, J.J. Kolata, Phys. Rev. C **85**, 014603 (2012).
175. A. Gómez Camacho *et al.*, J. Phys. G: Nucl. Part. Phys. **40**, 035103 (2013).
176. T.L. Belyaeva *et al.*, EPJ Web of Conferences **66**, 03008 (2014).
177. E.F. Aguilera *et al.*, Phys. Rev. C **63**, 061603(R) (2001).
178. E.F. Aguilera *et al.*, J. Phys.: Conf. Ser. **492**, 012002 (2014).
179. T. Nakatsukasa *et al.*, Prog. Theor. Phys. Suppl. **154**, 85 (2004).
180. M. Ito *et al.*, Nucl. Phys. A **787**, 267 (2007).
181. R. Kumar *et al.*, Phys. Rev. C **89**, 027601 (2014).
182. N. Curtis *et al.*, Phys. Rev. C **77**, 021301 (2008).
183. N. Curtis *et al.*, Phys. Rev. C **82**, 029907 (2010).
184. R.J. Charity *et al.*, Phys. Rev. C **80**, 024306 (2009).
185. K. Mercurio *et al.*, Phys. Rev. C **78**, 031602 (2008).
186. R.J. Charity *et al.*, Phys. Rev. C **75**, 051304 (2007).
187. R.E. Tribble, R.H. Burch, C.A. Gagliardi, Nucl. Instrum. Methods Phys. Res. A **285**, 441 (1989).
188. K. Markenroth *et al.*, Phys. Rev. C **62**, 034308 (2000).
189. E. Casarejos *et al.*, Phys. Rev. C **73**, 014319 (2006).
190. Y.Y. Yang *et al.*, Phys. Rev. C **90**, 014606 (2014).
191. J.F. Liang *et al.*, Phys. Rev. C **65**, 051603(R) (2002).
192. Z. Sun *et al.*, Nucl. Instrum. Methods Phys. Res. A **503**, 496 (2003).
193. P.F.F. Carnelli *et al.*, Phys. Rev. Lett. **112**, 192701 (2014).
194. S. Schramm, S.E. Koonin, Astrophys. J. **365**, 296 (1990).
195. P.F.F. Carnelli *et al.*, Nucl. Instrum. Methods Phys. Res. A **799**, 197 (2015).
196. D. Kovar *et al.*, Phys. Rev. C **20**, 1305 (1979).

197. S. Kaim *et al.*, Phys. Rev. C **91**, 024318 (2015).
198. J.M. Von Moss *et al.*, Phys. Rev. C **92**, 034301 (2015).
199. S. Lee *et al.*, Phys. Rev. C **76**, 034308 (2007).
200. D. Steppenbeck *et al.*, Phys. Rev. C **85**, 044316 (2012).
201. M. McCleskey *et al.*, Phys. Rev. C **89**, 044605 (2014).
202. E.D. Johnson *et al.*, Phys. Rev. C **80**, 045805 (2009).
203. N. Curtis *et al.*, Phys. Rev. C **73**, 057301 (2006).
204. C.A. Bertulani, Comput. Phys. Commun. **156**, 123 (2003).
205. A.M. Mukhamedzhanov, F.M. Nunes, Phys. Rev. C **72**, 017602 (2005).
206. A. Celler *et al.*, Nucl. Phys. A **432**, 421 (1985).
207. R.N. Sagaidak *et al.*, Phys. Rev. C **76**, 034605 (2007).
208. M. Alcorta *et al.*, Phys. Rev. Lett. **106**, 172701 (2011).
209. V.V. Sargsyan *et al.*, Phys. Rev. C **86**, 014602 (2012).
210. E. Sauvan *et al.*, Phys. Lett. B **491**, 1 (2000).
211. D.Q. Fang *et al.*, Phys. Rev. C **69**, 034613 (2004).
212. N. Keeley, N. Alamanos, Phys. Rev. C **75**, 054610 (2007).
213. J.C. Mein *et al.*, Phys. Rev. C **55**, R995 (1997).
214. J.-X. Li *et al.*, Chin. Phys. Lett. **27**, 032501 (2010).
215. J.-X. Li *et al.*, Chin. Phys. C **34**, 452 (2010).
216. A. Banu *et al.*, Phys. Rev. C **79**, 025805 (2009).
217. A. Di Pietro *et al.*, Phys. At. Nucl. **69**, 1366 (2006).
218. R. Morlock *et al.*, Phys. Rev. Lett. **79**, 3837 (1997).
219. G.L. Zhang *et al.*, Eur. Phys. J. A **49**, 57 (2013).
220. J.F. Liang *et al.*, Phys. Lett. B **681**, 22 (2009).
221. Y. Kucuk, A.M. Moro, Phys. Rev. C **86**, 034601 (2012).
222. M. Mazzocco *et al.*, Phys. Rev. C **82**, 054604 (2010).
223. M. Mazzocco *et al.*, Nucl. Phys. A **834**, 488 (2010).
224. M. Mazzocco *et al.*, J. Phys.: Conf. Ser. **312**, 082032 (2011).
225. M. Mazzocco *et al.*, EPJ Web of Conferences **17**, 13005 (2011).
226. J. Grineviciute, P. Descouvemont, Phys. Rev. C **90**, 034616 (2014).
227. P. Descouvemont, M.S. Hussein, Phys. Rev. Lett. **111**, 082701 (2013).
228. A.J. Koning, J.P. Delaroche, Nucl. Phys. A **713**, 231 (2003).
229. Q. Wang *et al.*, Chin. Phys. Lett. **23**, 1731 (2006).
230. Z. Bai *et al.*, Chin. Phys. Lett. **24**, 3384 (2007).
231. J.F. Liang *et al.*, Phys. Rev. C **65**, 051603 (2002).
232. M. Romoli *et al.*, Phys. Rev. C **69**, 064614 (2004).
233. C. Signorini *et al.*, Eur. Phys. J. A **44**, 63 (2010).
234. K.E. Rehm *et al.*, Phys. Rev. Lett. **81**, 3341 (1998).
235. C.R. Morton *et al.*, Phys. Rev. C **60**, 044608 (1999).